Organic ferroelectric diodes

Document status and date:
Published: 01/01/2015

Document Version:
Publisher's PDF, also known as Version of Record (includes final page, issue and volume numbers)

Please check the document version of this publication:

• A submitted manuscript is the version of the article upon submission and before peer-review. There can be important differences between the submitted version and the official published version of record. People interested in the research are advised to contact the author for the final version of the publication, or visit the DOI to the publisher's website.
• The final author version and the galley proof are versions of the publication after peer review.
• The final published version features the final layout of the paper including the volume, issue and page numbers.

Link to publication

Organic Ferroelectric Diodes

PROEFSCHRIFT

ter verkrijging van de graad van doctor aan de
Technische Universiteit Eindhoven, op gezag van de
rector magnificus prof.dr.ir. F.P.T. Baaijens, voor
een commissie aangewezen door het College voor
Promoties, in het openbaar te verdedigen
op woensdag 4 november 2015 om 16:00 uur

door

Vsevolod Khikhlovskyi

geboren te Zhovti Vody, Oekraine

Dit proefschrift is goedgekeurd door de promotoren en de samenstelling van de promotiecommissie is als volgt:

voorzitter:	prof.dr.ir. G.M.W. Kroesen
1^e promotor:	prof.dr.ir. M. Kemerink (Universiteit van Linköping)
2^e promotor:	prof.dr. G.H. Gelinck
copromotor(en):	prof.dr.ir. R.A.J. Janssen
leden:	prof.dr. B. Noheda (RUG)
	prof.dr. D.M. de Leeuw (MPIP Mainz)
	prof.dr. P.M. Koenraad

Het onderzoek of ontwerp dat in dit proefschrift/proefontwerp wordt beschreven is uitgevoerd in overeenstemming met de TU/e Gedragscode Wetenschapsbeoefening.

Contents

Chapter 1

Introduction

1.1 Introduction

Modern electronic devices are made of inorganic materials on rigid substrates such as glass and silicon using complicated manufacturing methods involving high-temperature process steps. Despite its tremendous success, there are functions that are not well addressed by conventional microelectronics technology. In particular, there is a need for low-cost, flexible electronics, to be integrated into everyday objects like paper, clothes and packaging material. This has given a boost to the development of new semiconductor materials that can be processed at low temperatures, preferably from solution, which in turn has allowed for the development of a variety of organic-based electronic devices on flexible plastic substrates, such as solar cells,[1] light-emitting diode displays,[2] field-effect transistors,[3] transponders,[4] sensors,[5,6] actuators,[7] and non-volatile memories.[8-12] The latter will be the topic of this thesis.

In order to store information electronically, a memory element should be able to be set to at least two distinctly different states ('bits'). Programming is preferably done by applying a short voltage pulse, while retrieving the information is preferably done by measuring a change in electrical resistance under conditions that do not alter the programmed state, so that the same state can be readout multiple times without re-programming. Ideally, the memory retains its state when no voltages are applied. These so-called non-volatile memories are ideal for wireless electronic labels, for instance.

In almost all foreseeable applications, multiple memory elements are needed to store multiple bits. The cross-bar memory array is the most promising structure in this regard (see Figure 1.1). A storage medium is sandwiched between two inter-crossing electrodes, forming the word- and bit-lines. This configuration allows for a high integration density due to a minimal footprint of $4 \times F^2$, with F the minimum feature size. Preferably, the information storage layer is not patterned. Eliminating patterning reduces manufacturing cost. The extreme parallel geometry of the cross-bar array, however, requires the implementation of a certain selection device to prevent read disturbance problems (see Figure 1.2). The cross-talk results in measuring a resistance that is equal to the resistance of the selected cell connected in parallel to the memory cells in all other word and bit lines. Hence reliable determination of the logic value therefore requires electrical isolation of the discrete cells. The problem can be solved by adding a rectifying diode to each cell.[14] Cho *et al.* demonstrated a 4×4 crossbar memory device constructed with hybrid-type devices consisting of an inorganic Schottky diode and organic unipolar memory components.[15] Yet, it is highly beneficial that the resistance switching device would inherently possess rectifying characteristics.

Non-volatile reprogrammable organic memories based on phase separated blends of polymer semiconductors and ferroelectrics were recently demonstrated by Asadi *et al.*[16] The concept behind this memory element is to combine two polymers that have distinct roles in its operation: a ferroelectric polymer provides the binary state and non-volatile data retention whereas a semiconducting polymer provides the means to probe that state via an

electrical signal. The diodes can be switched at biases larger than the coercive field. The resistance can be read-out non-destructively at low bias. Both symmetric and rectifying diodes have been reported with current modulation up to six orders of magnitude. In a theoretical study, Kemerink *et al.* calculated that the maximum bit density for this memory technology could be as high as 1 Gb/cm^2.[17] This new and exciting memory is the topic of further study in this thesis. Polymer ferroelectrics and its applicability in memory devices are discussed in detail in the following paragraph.
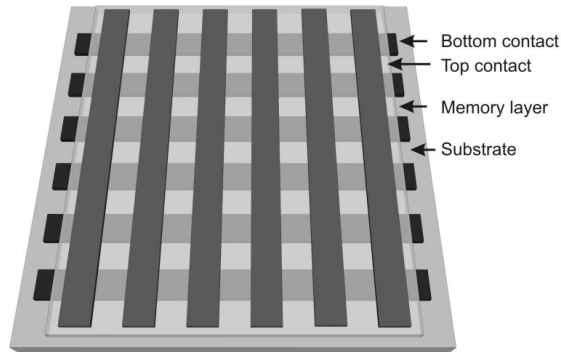
Figure 1.1: Schematic representation of a cross-bar memory array with the memory material sandwiched between the bottom contacts (word lines) and the top contacts (bit lines). Reproduced from Ref. 13.
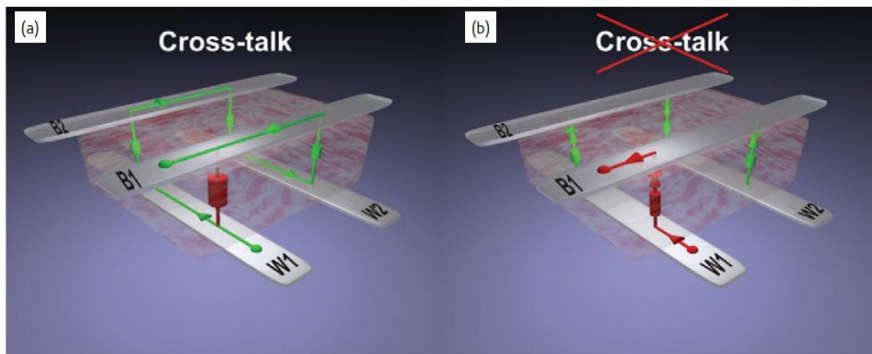
Figure 1.2: Schematic illustration of cross-talk. (a) A 4-bit array of bistable resistors. The high resistive OFF-state of the bit W1B1 (red) formed by word-line W1 and bit-line B1 is addressed. The three neighboring bits are in the low resistive ON-state (green). Addressing the high resistance W1B1 bit by applying a voltage difference between W1 and B1 is hampered by the low resistance parasitic path along the three neighboring bits. Consequently, the logic state of the W1B1 bit cannot be reliably read-out. (b) The cross-talk is circumvented by adding a rectifying diode in series with each discrete switch. The parasitic leakage path is then disabled by the reverse biased diode of the W2B2 bit. By applying a bias on appropriate rows and columns, the logic states, '0' or '1', of each individual bit can now unambiguously be addressed. Reproduced from Ref. 14.

1.2 Ferroelectric polymer memories

In general, ferroelectricity is described as a property of a material that possesses spontaneous electric polarization, the direction of which can be reversed by an external electric field. Experimentally, the reversal of the spontaneous polarization is observed as a single ferroelectric hysteresis loop shown in Figure 1.3. It contains important characteristics of the ferroelectric material: remnant polarization (P_r) – the ferroelectric polarization at zero electric field – and the coercive voltage (V_c) – the minimal electric voltage required to reverse the direction of the polarization.

One of the most promising, most studied and most commonly used organic ferroelectric materials is P(VDF-TrFE) – a random copolymer of vinylidene fluorine (VDF, -CH$_2$-CF$_2$-) and trifluoroethylene (TrFE, -CFH-CF$_2$-), schematically shown in Figure 1.4a. Its ferroelectric properties originate from the difference in electronegativity between fluorine, carbon and hydrogen yielding a large net dipole perpendicular to the polymer chain direction. P(VDF-TrFE) has several advantageous properties including a large remnant polarization, excellent polarization stability, low leakage for high resistivity and switching times as short as 1 microsecond. Furthermore, it is intrinsically bistable, *i.e.* it does not require a voltage to keep its polarization state. It can be processed from solution at low temperatures, opening the possibility of using a wide range of plastic substrates instead of glass – saving weight and making the final product thinner and virtually unbreakable. It is therefore ideally suited for next-generation organic electronics applications that require re-programmable, non-volatile memories. Owing to its piezoelectric and pyroelectric properties this material is used in other applications as well, such as transducers,[18] sensors,[19] and actuators.[20,21]
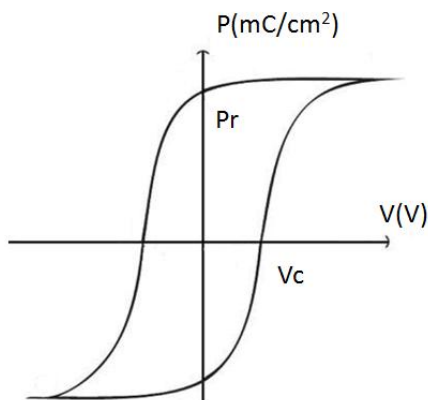
Figure 1.3: Schematic representation of a ferroelectric hysteresis loop. P_r and V_c indicate remnant polarization and coercive voltage, respectively.
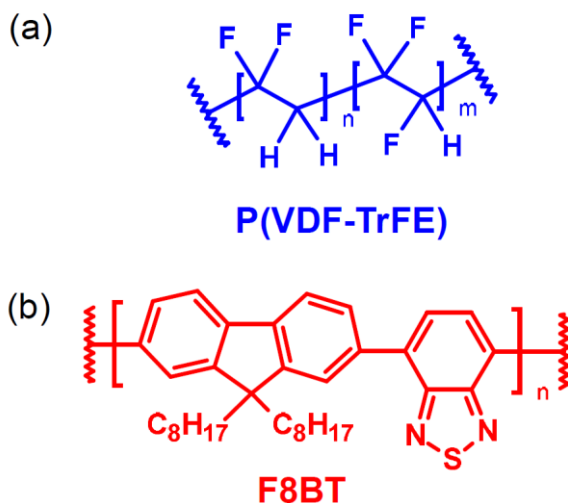
Figure 1.4: Schematic representation of the chemical structures of (a) ferroelectric polymer P(VDF-TrFE) and (b) semiconducting polymer F8BT.

Different types of P(VDF-TrFE)-based memories have been reported: capacitors,[22,23] thin-film transistors[12] and ferroelectric diodes.[16] The basic layout of each of these device types is shown in Figure 1.5.
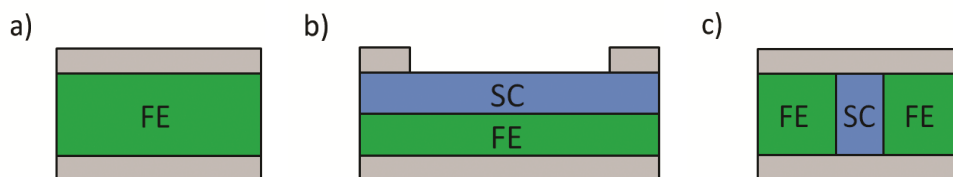
Figure 1.5: Schematic representation of (a) ferroelectric capacitor; (b) ferroelectric thin-film transistor; (c) ferroelectric diode. Ferroelectric and semiconductor are denoted as FE and SC respectively.

In the ferroelectric capacitor the ferroelectric film is sandwiched between two metal electrodes (see Figure 1.5a). The ferroelectric can be polarized by applying a sufficiently large electric field across the electrodes. Depending on the direction of the polarization, the memory is in its '1' state or in its '0' state. One important advantage of the ferroelectric capacitor is the possibility to integrate them in the form of cross-bar arrays, without the need for transistors or other electronic components. Another advantage is that the information is non-volatile, *i.e.* the ferroelectric polarization remains when the power is turned off. In a typical memory array, the capacitors are defined by patterning the top electrode into columns and the bottom electrodes into rows. The memory state from a

capacitor is changed by addressing the corresponding row and column and applying a bias that will provide the desired ferroelectric polarization. To program all memory elements, each row is sequentially addressed. To read out the polarization state of each memory element, again a sufficiently large voltage is applied and external electronics is used to detect switching charge. The expected switching charge is $2 \times Pr$, but only when the ferroelectric polarization is reversed. This gives two problems. Firstly, downscaling of the memory areas implies detecting less switching charge, and requires more sensitive (expensive) readout electronics outside the array. Second, as read-out of the state occurs via the detection of the switching current by applying a voltage that exceeds the coercive voltage, the original state may be changed. This is the problem of so-called destructive read-out. It is possible to set back the memory to its original state, but this requires an extra step.

In a ferroelectric thin-film transistor the ferroelectric is used as a gate dielectric in an otherwise conventional field effect transistor (see Figure 1.5b).[12] The polarization of the ferroelectric layer alters the threshold voltage of the field effect transistor thus producing distinctly different conductivity states at a given potential depending upon the polarization. Only a small source-drain potential is required to read out the state. The ferroelectric thin-film transistor thus allows the polarization state to be read without altering the polarization. This provides the advantage that the memory transistor is not subjected to the destructive read/rewrite cycle commonly employed in ferroelectric capacitors. A cost for this improvement is the increased complexity of the device and the associated increase in the number of layers.

The ferroelectric diode was first demonstrated by Asadi *et al.*[16,24-27] A spin-coated film that is sandwiched between two metal electrodes consists of pillars of a semiconducting polymer, continuous from top to bottom, embedded in a ferroelectric matrix. A schematic presentation of the cross-section of a diode based on the blend is given in Figure 1.5c. Because of the insulating ferroelectric matrix transport of the majority of charge carriers is possible only via the semiconducting phase. Work function(s) of the metal contact(s) are purposely chosen to yield substantial injection barrier(s) into the semiconductor. Without ferroelectric polarization, charge injection is therefore limited and the current in the device is low. When the ferroelectric is poled in the right direction the polarization field of the ferroelectric apparently lowers the injection barrier at the semiconductor-metal interface as a higher device current is observed.[16] When the ferroelectric is poled in the other direction, the current is low again. A bistable resistive switch is thus obtained. It has to be noted that the diodes can be switched at biases larger than the coercive field. Originally, the switching mechanism of the device was proposed to be related to a particular morphology in which ferroelectric polarization charges induce counter charges in the semiconductor, facilitating injection.[16] Later, it was proposed on basis of numerical calculations that the stray field of the ferroelectric might be the driving force for resistive switching of the ferroelectric diode.[17] However, at that moment no experimental evidence was presented to confirm this theoretical model.

Figure 1.6b shows the corresponding working principle of the device that is programmed in the ON-state in the case of two injection-limiting (non-Ohmic) contacts. In the scenario of Ref. 17, the stray field from the ferroelectric, shown with black dotted arrows, enhances injection of charge carriers into the semiconductor. If the stray field is sufficiently large, it can lower the injection barrier and locally make the contact Ohmic. The current then becomes space charge limited, *i.e.* bulk limited.[24] When the device is programmed in the OFF-state the stray field actually increases the injection barrier, further suppressing the current in the device (see Figure 1.6c). Figures 1.6a-c also provide the energy diagram of the device in the corresponding three distinct cases. Black, red and blue curves in Figure 1.6a-c correspond to the device with a ferroelectric which is non-poled, poled upwards and downwards respectively. It is clear that only the upwards direction of the polarization lowers the injection barrier, but does so for both types of charge carriers. Finally, *I-V* characteristics of P(VDF-TrFE):F8BT (poly[(9,9–di–*n*–octylfluorenyl-2,7–diyl)–*alt*–(benzo[2,1,3]thiadiazol-4,8-diyl)], see Figure 1.4b) active blend sandwiched between gold electrodes are shown in Figure 1.7. Starting from the OFF-state, *i.e.* with downward polarization (see Figure 1.6c), the device turns on once the coercive voltage of the ferroelectric is exceeded. On the downward sweep the device remains in the ON-state due to the upward polarization, resulting in a hysteretic loop.[14] Hence the resistance can be read-out non-destructively at low bias. Both symmetric and rectifying diodes have been reported with current modulation up to six orders of magnitude. By deliberately varying the HOMO energy of the semiconductor and the work-function of the metal electrode, it is demonstrated that injection barriers up to (nominally) 1.6 eV can be surmounted by the ferroelectric polarization.[24]

Such device promises the best characteristics of both types of the devices mentioned above – ferroelectric bistability, non-destructive resistive readout and current rectification. It is important to mention that the device satisfies the rectification requirement mentioned above. By sandwiching this polymer blend film between rows and columns of metal electrode lines, where each intersection makes up one memory cell, 1 kilobit cross-bar arrays with bit densities up to 10 kb/cm^2 have been demonstrated by van Breemen *et al*.[28]

So far most of the experimental reports focused on the macroscopic electrical characteristics of such devices[16,28,29] and the mechanism of device operation is not yet fully resolved. It has been shown that the operation of ferroelectric diodes strongly depends on the 3D-morphology of the phase-separated blend.[30,31] The combination of detailed investigation of microstructure and charge transport measurements will lead to understanding of the switching mechanism including estimations for the injection barriers that can be tolerated, and the current rectification that can be achieved.
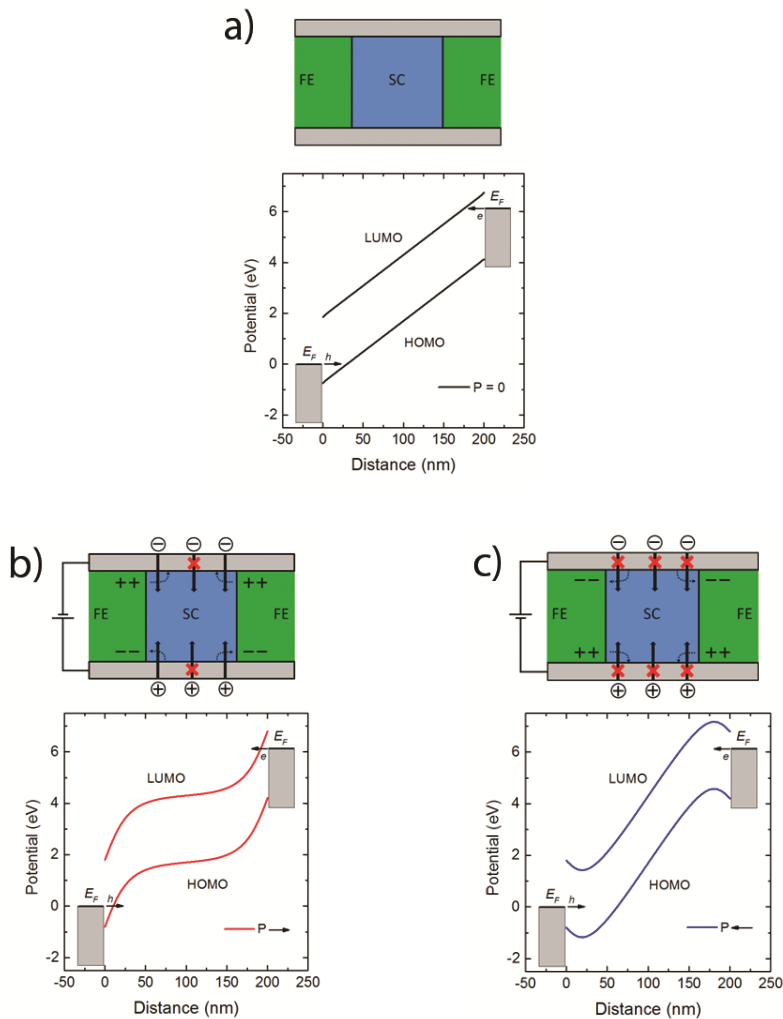
Figure 1.6: Schematic representation of the structure, the operation mechanism and the energy diagram of ferroelectric diode. (a) Simplified view of the cross-section and energy diagram of the ferroelectric diode. Green and blue regions correspond to the ferroelectric and semiconducting polymers, respectively. Top and bottom metal electrodes (possibly different materials) are indicated in grey. (b) Device in the ON-state. (c) Device in the OFF-state. The stray field increases the injection barrier, suppressing the current in the device. Minuses (−) and pluses (+) indicate polarization charges in the ferroelectric. Black dashed arrows indicate the stray field from the ferroelectric. The stray field lowers the injection barrier leading to nearly Ohmic contact(s) and space charge limited current (SCLC).
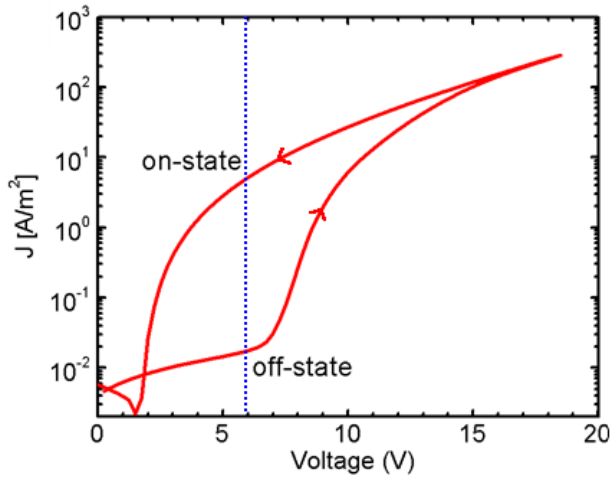
Figure 1.7: *I-V* characteristics of P(VDF-TrFE):F8BT active blend sandwiched between gold electrodes. The device is programmed in the ON- or OFF- state by applying a voltage exceeding, respectively, the positive or negative coercive voltage of the ferroelectric phase of the blend (blue dashed line). Arrows indicate the scan direction.

It has to be noted that the blend formation is driven by a spinodal decomposition process – a mechanism by which a solution of two or more components can separate into distinct phases (*e.g.* ferroelectric matrix and semiconductor domains) with distinctly different chemical compositions and physical properties. The phase separation due to spinodal decomposition occurs uniformly throughout the material – not just at discrete nucleation sites. Since the morphology is key to the operation and performance of the ferroelectric diodes getting control over the 3D-morphology formation is crucial for improving the device performance.

Another important parameter is data retention. Loss of polarization with time and/or upon readout can lead to data corruption and therefore loss of information.[32] This can be compensated by redundancy of memory bits, or via additional re-writing of the memory arrays. In all cases, this is not ideal and data retention is preferably very long. In ferroelectric capacitors and thin-film transistors depolarization effects are well studied. Although there are a number of publications in which data retention of ferroelectric diodes is studied,[33-35] the detailed mechanism of information loss, especially at the local scale, is unknown for our diodes.

1.3 Characterization of the ferroelectric polarization

Ferroelectric polarization in a ferroelectric capacitor is typically studied in a so-called Sawyer-Tower setup. The switching charge due to changes in ferroelectric polarization is detected and separated from other (leakage) currents by applying a so-called PUND (positive up negative down) scheme.[36,37] This technique can however not be applied in our ferroelectric diodes, due to their macroscopic conductivity that overwhelms the ferroelectric switching currents. Therefore, several new methods needed to be employed to unravel the operational mechanism of the ferroelectric diode. In particular, the double-wave method (DWM) and piezoresponce force microscopy (PFM) were used at respectively the macroscopic and microscopic levels. Scanning probe techniques were used to measure the voltage and current spatially resolved with the aim to experimentally investigate scaling of the current transport with the domain size.

1.3.1 Piezoresponce force microscopy

In 1992, Guthner and Dransfeld first reported piezoresponse force microscopy (PFM).[36] PFM is a tool for local imaging, spectroscopy and manipulation of piezoelectric and ferroelectric materials. PFM relies on the inverse piezoelectric effect, *i.e.* a local mechanical deformation in response on an electrical stimulation. The deformation of a material in the direction perpendicular to the film surface – ΔS is linked to the applied electric field – E via a so-called effective piezoelectric coefficient or piezoelectric modulus – d_{33} by $\Delta S = d_{33} \times E$.[38] It has to be noted that in case of P(VDF-TrFE) d_{33} is negative.[39] Typical PFM uses a standard scanning force microscope (SFM) that operates in contact mode. An oscillating voltage is applied to the conductive tip of the SFM. Because of the piezoelectric effect the voltage-induced deformation of the sample leads to periodic
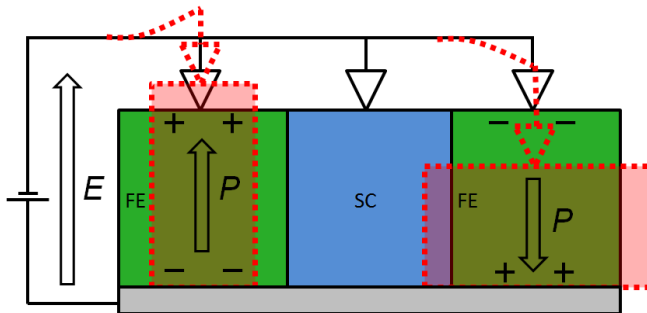
Figure 1.8: Schematic representation of vertical PFM on ferroelectric diode, sketched in the same color coding as Figure 1.6. The effective piezoelectric coefficient – $d_{33} > 0$.

vibrations of the sample surface which are transmitted to the tip. The resulting oscillations of the cantilever are detected as the first harmonic component of the tip deflection and can be read out with the help of a lock-in amplifier. Figure 1.8 shows a schematic representation of vertical PFM on ferroelectric diode. It is clear that the PFM signal comes only from the ferroelectric part of the blend. In Chapter 3, PFM, in combination with other scanning probe microscopy (SPM) techniques, is used to reveal the working mechanism of the ferroelectric diode at the local scale.

1.3.2 Double-wave method

Clearly there is a strong demand for accurate measurements of the key properties of the ferroelectric in actual devices – coercive voltage and remnant polarization. A proper and conceptually simple way of doing that is the double-wave method (DWM), which is a powerful tool for accurately measuring ferroelectric hysteresis loops.[40,41] The concept of the DWM is based on the idea that the polarization state of a ferroelectric can be probed by flipping its polarization and detecting the corresponding switching charges.

The DWM was realized by using the experimental setup shown in Figure 1.9. It consists of a signal generator (SG, typically a function generator connected to a voltage amplifier), a picoammeter (A), an oscilloscope (OSC) and the device. The signal generator, the picoammeter and the device are connected in series whereas an oscilloscope (OSC) is connected in parallel with the analog output of the picoammeter (V_{OUT}). Thus the signal generator is used for constructing an appropriate input signal applied to the device. At the same time the switching charges of the device and the applied voltage can be measured and visualized by the oscilloscope.
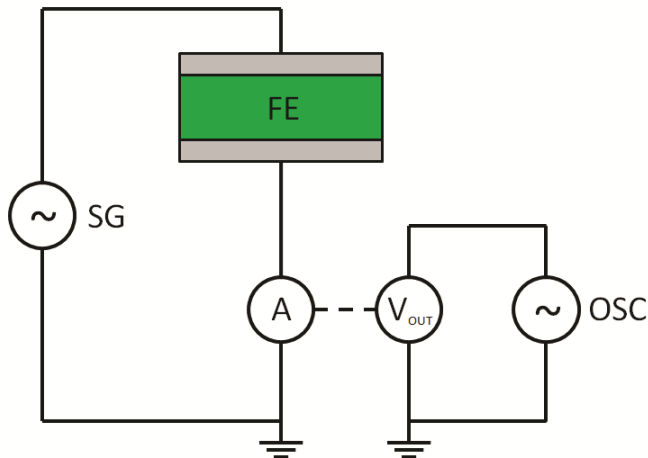
Figure 1.9: Schematic representation of the experimental setup used to study the ferroelectric properties of the devices. A signal generator (SG), a picoammeter (A), an oscilloscope (OSC) and the device are assembled together.

Figure 1.10 shows a typical input signal used in the DWM-based experiments for measuring inner and saturated ferroelectric hysteresis loops together with the corresponding schematic current responses. The preparation part of the signal is used for constructing the desired polarization state of the ferroelectric. The probing part is used for studying the prepared ferroelectric polarization. To probe the ferroelectric polarization a triangular pulse, labeled '1' in Figure 1.10, is applied and the corresponding switching current is read out. Contributions from displacement and the leakage currents can be determined with a second probing pulse – '2' in Figure 1.10. As this pulse is equal in size and slope to the first, no polarization switching occurs, whereas displacement and leakage currents are, in lowest order, the same. Red solid curves, labeled '1' and '2' in Figure 1.10, represent the corresponding schematic current responses. The shaded area corresponds to the current associated with the switching of the ferroelectric polarization. Dotted and dashed black lines represent current responses due to the leakage and the displacement contribution, respectively. Thus using the response to the second pulse all unwanted responses can be subtracted from the response to the first pulse, giving solely the voltage-dependent switching response of the ferroelectric. Moreover the displacement current can upfront be
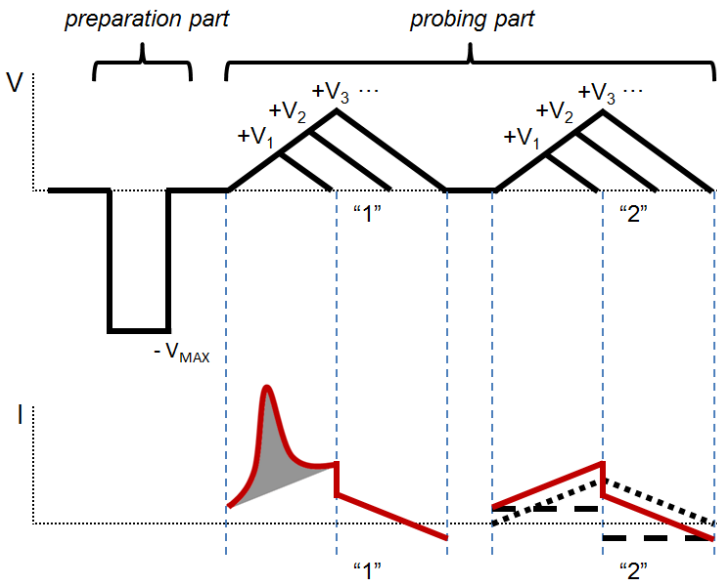
Figure 1.10: Schematic representation of the signals used in the DWM for measuring inner and saturated ferroelectric hysteresis loops and corresponding schematic current responses. The amplitude V_{max} of the preparation signal is chosen to be well above the coercive voltage of the ferroelectric capacitor. Different probing signals V_i have the same ramping speeds but different amplitudes for measuring inner ferroelectric hysteresis loops. Red solid curves represent schematic current responses measured with the probing signals '1' and '2'. The shaded area corresponds to the switching current associated with the reversal of the ferroelectric polarization. Dotted and dashed black lines represent currents due to leakage and displacement, respectively.

significantly suppressed by doing slow measurements – the so-called quasi-static regime of the DWM. In addition the preparation part of the signal can be changed as well as the probing one (V_i in Figure 1.10), giving the possibility to study different switching properties of a ferroelectric material. Hence the DWM provides a simple and a powerful tool for detailed study of ferroelectrics. In Chapter 2 and 7 the DWM was used to manipulate and measure the polarization state of the P(VDF-TrFE)-based capacitors and diodes.

It should be noted that the DWM originates from the so-called PUND (positive 'up' negative 'down') approach.[36,37] The basic idea behind both methods is similar and can be summarized as flipping the polarization state of the ferroelectric and detecting both the switching (*i.e.* associated with the ferroelectric polarization) and the nonswitching currents (*i.e.* displacement and leakage current). However, the PUND approach is usually associated with step-like voltage pulses. It often serves for transient-type measurements or for determining a total polarization of the ferroelectric material. At the same time the DWM uses continuous transients, for instance linearly increasing/decreasing voltages, giving rise to much lower displacement currents. Hence it is more suitable for the quasi-static regime in which we are interested here.

1.4 Outline of the thesis

The aim of the research described in this thesis is focused on the development, characterization and optimization of ferroelectric P(VDF-TrFE)-based memory devices.

In Chapter 2, a multi-bit organic ferroelectric-based non-volatile memory with binary readout from a simple capacitor structure is introduced. The working principle of the multi-bit device is quite general and only demands fulfillment of three requirements described in Chapter 2. We showed experimentally that the organic ferroelectric polymer – P(VDF-TrFE) - qualifies for being a multi-bit storage medium. Hence we demonstrated a 3-bit data P(VDF-TrFE)-based storage element. In addition, we measured the ferroelectric properties (V_c and P_r) of P(VDF-TrFE) that will be used in the rest of the thesis.

In Chapter 3, the operational mechanism of the ferroelectric diode based on the blend of P(VDF-TrFE):F8BT is studied at the nanoscale. Various scanning probe techniques were combined with numerical modeling. Resistive switching is shown to result from modulation of the charge injection barrier at the semiconductor–electrode interfaces. It has been proven experimentally that the modulation is driven by the stray field of the polarization charges in the ferroelectric phase and consequently is restricted to regions where semiconductor and ferroelectric phases exist in close vicinity.

In Chapter 4, we study the 3D nanoscale morphology of P(VDF-TrFE):F8BT by AFM and statistical analysis, by selectively dissolving the ferroelectric and semiconductor components in the blend. We found that the blend consists of a ferroelectric matrix with

three types of embedded semiconductor domains. In addition, the existence of a thin wetting layer at the bottom electrode was revealed. The criteria for the general applicability of the presented technique are discussed as well. Thus a simple approach for studying the morphology of the blend at the local scale was introduced.

In Chapter 5, the polymer phase separation of P(VDF-TrFE):F8BT blends is studied in detail. It was also demonstrated that it is possible to direct the semiconducting domains of a phase-separating mixture of P(VDF-TrFE) and F8BT in a thin film into a highly ordered 2D lattice by means of surface directed phase separation. By optimizing the ratio of the blend components, the number of electrically active semiconductor domains is maximized. Thus the electrical performance of the memories was improved.

In Chapter 6, the device structure and its impact on the device performance are studied by advanced scanning probe techniques. We found that a thin wetting layer drastically influences the device performance by hindering the ferroelectric polarization in one of the bias directions. An optimal and simple fabrication recipe to avoid the formation of this wetting layer is found. The new fabrication provides an improved blend structure that offers better device performance.

In Chapter 7, the data retention of the ferroelectric diodes is studied. It was found that the data retention is intimately linked to the morphology of the phase-separated polymer blend and, surprisingly, is due to polarization loss in a narrow region around the semiconducting domains. We argue that the depolarization is driven by an energy minimization process and inherently present in this type of phase-separated polymer blends.

In Chapter 8, a summary and an outlook are presented.

1.5 References

[1]   D. Gebeyehu, C.J. Brabec, F. Padinger, T. Fromherz, J.C. Hummelen, D. Badt, H. Schindler, N.S. Sariciftci, The interplay of efficiency and morphology in photovoltaic devices based on interpenetrating networks of conjugated polymers with fullerenes, *Synth. Met.* **2001**, *118*, 1.

[2]   L. Zhou, A. Wanga, S.-C. Wu, J. Sun, S. Park, T.N. Jackson, All-organic active matrix flexible display, *Appl. Phys. Lett.* **2006**, *88*, 083502.

[3]   G.H. Gelinck, H.E.A. Huitema, E. van Veenendaal, E. Cantatore, L. Schrijnemakers, J.B.P.H. van der Putten, T.C.T. Geuns, M. Beenhakkers, J.B. Giesbers, B.-H. Huisman, E.J. Meijer, E.M. Benito, F.J. Touwslager, A.W. Marsman, B.J.E. van Rens, D.M. de Leeuw, Flexible active-matrix displays and shift registers based on solution-processed organic transistors, *Nat. Mater.* **2004**, *3*, 106.

[4]   P.F. Baude, D.A. Ender, M.A. Haase, T.W. Kelley, D.V. Muyres, S.D. Theiss, Pentacene-based radio-frequency identification circuitry, *Appl. Phys. Lett.* **2003**, *82*, 3964.

[5]   T. Someya, Y. Kato, T. Sekitani, S. Iba, Y. Noguchi, Y. Murase, H. Kawaguchi, T. Sakurai, Conformable, flexible, large-area networks of pressure and thermal sensors with organic transistor active matrixes, *Proc. Natl. Acad. Sci. U.S.A.* **2005**, *102*, 12321.

[6]   T. Sekitani, T. Yokota, U. Zschieschang, H. Klauk, S. Bauer, K. Takeuchi, M. Takamiya, T. Sakurai, T. Someya, Organic nonvolatile memory transistors for flexible sensor arrays, *Science* **2009**, *326*, 1516.

[7]   T. Sekitani, M. Takamiya, Y. Noguchi, S. Nakano, Y. Kato, T. Sakurai, T. Someya, A large-area wireless power-transmission sheet using printed organic transistors and plastic MEMS switches, *Nat. Mater.* **2007**, *6*, 413.

[8]   C.A. Nguyen, S.G. Mhaisalkar, J. Ma, P.S. Lee, Enhanced organic ferroelectric field effect transistor characteristics with strained poly(vinylidene fluoride-trifluoroethylene) dielectric, *Org. Electron.* **2008**, *9*, 1087.

[9]   K.H. Lee, G. Lee, K. Lee, M.S. Oh, S. Im, Flexible low voltage nonvolatile memory transistors with pentacene channel and ferroelectric polymer, *Appl. Phys. Lett.* **2009**, *94*, 093304.

[10]   T. Sekitani, K. Zaitsu, Y. Noguchi, K. Ishibe, M. Takamiya, T. Sakurai, T. Someya, Printed nonvolatile memory for a sheet-type communication system, *IEEE Trans. Electron. Dev.* **2009**, *56*, 1027.

[11]   R. Schroeder, L.A. Majewski, M. Grell, All-organic single-transistor permanent memory device, *Adv. Mater.* **2004**, *16*, 633.

[12]   R.C.G. Naber, C. Tanase, P.W.M. Blom, G.H. Gelinck, A.W. Marsman, F.J. Touwslager, S. Setayesh, D.M. de Leeuw, High-performance solution-processed polymer ferroelectric field-effect transistors, *Nat. Mater.* **2005**, *4*, 243.

[13]   P. Heremans, G.H. Gelinck, R. Muller, K.-J. Baeg, D.-Y. Kim, Y.-Y. Noh, Polymer and organic nonvolatile memory devices, *Chem. Mater.* **2011**, *23*, 341.

[14]   K. Asadi, M. Li, P.W.M. Blom, M. Kemerink, D.M. de Leeuw, Organic ferroelectric opto-electronic memories, *Mater. Today* **2011**, *14*, 12, 592.

[15]   B. Cho, T.-W. Kim, S. Song, Y. Ji, M. Jo, H. Hwang, G.-Y. Jung, and T. Lee, Rewritable switching of one diode–one resistor nonvolatile organic memory devices, *Adv. Mater.* **2010**, *22*, 1228.

[16]   K. Asadi, D.M. de Leeuw, B. de Boer, P. Blom, Organic non-volatile memories from ferroelectric phase- separated blends. *Nat. Mater.* **2008**, *7*, 547.

[17]   M. Kemerink, K. Asadi, P.W.M. Blom, D.M. de Leeuw, The operational mechanism of ferroelectric-driven organic resistive switches, *Org. Electron.* **2012**, *13*, 147.

[18]   S. Takahashi, Properties and characteristics of P(VDF/TrFE) transducers manufactured by a solution casting method for use in the MHz-range ultrasound in air, *Ultrasonics* **2012**, *52*, 3, 422.

[19]   S.-S. Jel, T. Sharmal, Y. Leel, B. Gill, J.X. Zhani, A thin-film piezoelectric P(VDF-TrFE) based implantable pressure sensor using lithographic patterning, *MEMS* **2011**, 644.

[20]   Z.-Y. Cheng, V. Bharti, T.-B. Xu, H. Xu, T. Mai, Q.M. Zhang, Electrostrictive poly(vinylidene fluoride-trifluoroethylene) copolymers, *Sensor Actuator A* **2001**, *90*, 138-147.

[21]   S.-H. Bae, O. Kahya, B.K. Sharma, J. Kwon, H.J. Cho, B. Ozyilmaz, J.-H. Ahn, Graphene-P(VDF-TrFE) multilayer film for flexible applications, *ASC Nano* **2013**, *7*, 4, 3130–3138.

[22]   S. Usui, T. Nakajima, Y. Hashizume, S. Okamura, Polarization induced resistance switching effect in ferroelectric vinylidenefluoride/trifluoroethylene copolymer ultrathin films, *Appl. Phys. Lett.* **2014**, *105*, 162911.

[23] W.J. Hu, D.-M. Juo, L. You, J. Wang, Y.-C. Chen, Y.-H. Chu, T. Wu, Universal ferroelectric switching dynamics of vinylidene fluoride-trifluoroethylene copolymer films, *Sci. Rep.* **2014**, *4*, 4772.

[24] K. Asadi, T.G. de Boer, P.W.M. Blom, D.M. de Leeuw, Tunable injection barrier in organic resistive switches based on phase-separated ferroelectric–semiconductor blends, *Adv. Funct. Mater*. **2009**, *19*, 3173.

[25] K. Asadi, P.W.M. Blom, D.M. de Leeuw, The MEMOLED: Active addressing with passive driving, *Adv. Mater.* **2011**, *23*, 865.

[26] J. Hu, J. Zhang, Z. Fu, J. Weng, W. Chen, S. Ding, Y. Jiang, G. Zhu, Fabrication of electrically bistable organic semiconducting/ferroelectric blend films by temperature controlled spin coating, *ACS Appl. Mater. Interfaces* **2015**, *7*, 6325.

[27] S.H. Sung, B.W. Boudouris, Systematic control of the nanostructure of semiconducting-ferroelectric polymer composites in thin film memory devices, *ACS Macro Lett.* **2015**, *4*, 293.

[28] A.J.J.M. van Breemen, J.-L. van der Steen, G. van Heck, R. Wang, V. Khikhlovskyi, M. Kemerink, G.H. Gelinck, Crossbar arrays of nonvolatile, rewritable polymer ferroelectric diode memories on plastic substrates. *Appl. Phys. Express* **2014**, *7*, 031602.

[29] K. Asadi, P.W.M. Blom, D.M. de Leeuw, The MEMOLED: active addressing with passive driving, *Adv. Mater.* **2011**, *23*, 865.

[30] C.R. McNeill, K. Asadi, B. Watts, P.W.M. Blom, D.M. de Leeuw, Structure of Phase-Separated ferroelectric/semiconducting polymer blends for organic non-volatile memories, *Small* **2010**, *6*, 4, 508.

[31] K. Asadi, H.J. Wondergem, R.S. Moghaddam, C.R. McNeill, N. Stingelin, B. Noheda, P.W.M. Blom, D.M. de Leeuw, Spinodal decomposition of blends of semiconducting and ferroelectric polymers, *Adv. Funct. Mater*. **2011**, *21*, 1887.

[32] K. Asadi, J. Wildeman, P.W.M. Blom, D.M. de Leeuw, Retention time and depolarization in organic nonvolatile memories based on ferroelectric semiconductor Phase-Separated Blends, *IEEE Trans Electron Devices* **2010**, *57*.

[33] M.A. Khan, U.S. Bhansali, D. Cha, H. N. Alshareef, *Adv. Funct. Mater.* **2013**, *23*, 2145.

[34] J. Hu, J. Zhang, Z. Fu, J. Weng, W. Chen, S. Ding, Y. Jiang, G. Zhu, Fabrication of electrically bistable organic semiconducting/ferroelectric blend films by temperature controlled spin coating, *ACS Appl. Mater. Interfaces* **2015**, *7*, 6325.

[35] S.H. Sung, B.W. Boudouris, Systematic control of the nanostructure of Semiconducting-Ferroelectric polymer composites in thin film memory devices, *ACS Macro Lett.* **2015**, *4*, 293.

[36] J.F. Scott, L. Kammerdiner, M. Parris, S. Traynor, V. Ottenbacher, A. Shawabkeh, W.F.J. Oliver, Switching kinetics of lead zirconate titanate submicron thin film memories, *Appl. Phys.* **1988**, *64*, 787.

[37] S.D. Traynor, T.D. Hadnagy, L. Kammerdiner, Capacitor test simulation of retention and imprint characteristics for ferroelectric memory operation, *Integr. Ferroelectr.* **1997**, *16*, 1.

[38] P. Güthner, K. Dransfeld, Local poling of ferroelectric polymers by scanning force microscopy, *Appl. Phys. Lett.* **1992**, *61*, 1137.

[39]   A.V. Bune, C. Zhu, S. Ducharme, L.M. Blinov, V.M. Fridkin, S.P. Palto, N.G. Petukhova, S.G. Yudin, Piezoelectric and pyroelectric properties of ferroelectric Langmuir–Blodgett polymer films, *J. Appl. Phys.* **1999**, *85*, 7869.

[40]   M. Fukunaga, Y. Noda, Improvement of the double-wave method for ferroelectric hysteresis loops and its application to multiferroic $EuMn_2O_5$, *J. Korean Phys. Soc.* **2009**, *55*, 888.

[41]   M. Fukunaga, Y. Noda, New technique for measuring ferroelectric and antiferroelectric hysteresis loops, *J. Phys. Soc. Jpn.* **2008**, *77*, 064706.

Chapter 2

Multi-bit organic ferroelectric memory

Storage of multiple bits per element is a promising alternative to miniaturization for increasing the information data density in memories. In this chapter, we introduce a multi-bit organic ferroelectric-based non-volatile memory with binary readout from a simple capacitor structure. The functioning of our multi-bit concept is quite generally applicable and depends on the following properties for the data storage medium: (a) The data storage medium effectively consists of microscopic switching elements ('hysterons'). (b) The positive and negative coercive fields of each hysteron are equal in magnitude. (c) The distribution of hysteron coercive fields has substantial width. We show that the organic ferroelectric copolymer P(VDF-TrFE) meets these requirements. All basic properties of our device were measured and modeled in the framework of the dipole switching theory (DST). As a first example we show the possibility to independently program and subsequently read out the lower, middle and upper parts of the hysteron distribution function, yielding a 3-bit memory in a single capacitor structure. All measured devices show good state reproducibility, high endurance and potentially great scalability.

2.1 Introduction

There is a great ongoing search for novel non-volatile memory technologies. Systems investigated include phase changing materials,[1] filamentary conductivity switching oxides[2,3] and various 'ferroic' systems like ferromagnetic, ferroelectric and multi-ferroic materials[4-10] Of these the organic ferroelectric random access memory (FeRAM) is a promising element for printable, large area, low-cost electronic circuits. A major concern in FeRAM is the limited minimum feature size that can be reached in general and with low-cost, large-area technology in particular. Potentially this problem can be mitigated by using multiple discrete states in a single memory element. Recently a number of multi-bit memory elements were proposed[11,12] but either require undesired additional device structuring or suffer from non-binary readout signals.

In this chapter, we propose a non-volatile multi-bit organic ferroelectric-based memory with binary readout from a simple capacitor structure. The operational principle behind our multi-bit device is quite general, with the applicability of the dipole switching theory (DST) as only constraint.[13,14] The DST considers a ferroelectric material as a collection of micro dipoles (hysterons) described by a specific Preisach distribution function.[15] We show experimentally that the organic ferroelectric copolymer P(VDF-TrFE) meets all the requirements to be described by the DST. On this basis we demonstrate a non-volatile 3-bit data storage element. We show the possibility to independently program and subsequently read out the lower, middle and upper parts of the hysteron distribution function. This shows that a simple capacitor structure based on this organic ferroelectric material can be used as multi-bit low-cost memory element.

2.2 Results and discussion

2.2.1 Study of ferroelectric properties of P(VDF-TrFE)

The devices investigated here were simple metal-insulator-metal capacitors with Au electrodes and the organic ferroelectric P(VDF-TrFE) as insulator. The material is commercially available and known for its robustness and good retention.[16,17] Fabrication and measurement details can be found in the experimental section. First, the general ferroelectric properties of the P(VDF-TrFE) capacitor were characterized. Figure 2.1 shows a series of ferroelectric (displacement charge) hysteresis loops using sinusoidal input voltage with different amplitudes at a frequency of 50 Hz. The inner loops correspond to the partially switched polarization whereas the saturated loop is related to the completely switched ferroelectric. From the saturated loop the remnant polarization (P_r) and coercive voltage (V_c) are estimated to be 70 mC/m^2 and 13.5 V respectively. It has to be noticed that the P_r and the V_c cannot be accurately determined from such measurements due to the presence of displacement and leakage currents.
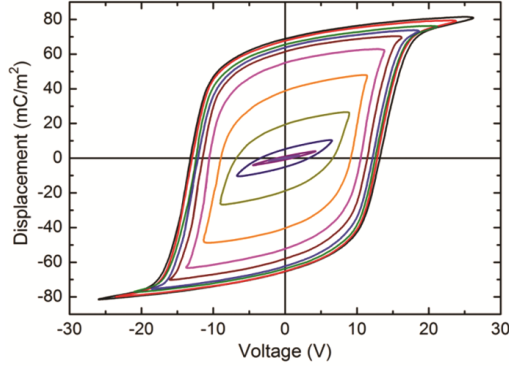
Figure 2.1: Displacement charge versus applied voltage hysteresis loop of a 200 nm thick Au/P(VDF-TrFE)/Au capacitor at a frequency of 50 Hz.

In order to obtain the pure ferroelectric polarization of the P(VDF-TrFE) capacitor the displacement contribution and the leakage current should be suppressed and excluded. A proper and simple way of doing this is by using the double-wave method (DWM), which is a powerful tool for accurately measuring ferroelectric hysteresis loops.[18,19] The concept of the DWM is described in detail in Chapter 1.

The solid curves in Figure 2.2a represent a series of ferroelectric hysteresis loops measured on the P(VDF-TrFE) capacitor using the quasi-static approach of the DWM. Since the displacement contribution and the leakage current were always negligible and completely excluded from the data, all measured values correspond to the pure ferroelectric polarization of the capacitor. This is in line with a fact that P(VDF-TrFE) is known to be an excellent insulator (resistivity $< 10^{10}$ Ohm·m). In addition no signs of moving ionic or parasitic electronic charges were observed. The remnant saturated polarization (P_r) and coercive voltage (V_c) are determined to be 60 mC/m^2 and 9.2 V ($E_c = 4.6 \times 10^7$ V/m) respectively. As in the previous case the inner loops describe the partially switched ferroelectric polarization. The difference between hysteresis loops and related parameters shown in Figure 2.1 and Figure 2.2a is due to the displacement and leakage contributions discussed above and due to the frequency dependence of the switching properties of the ferroelectric.[20] The frequency dependence of the P(VDF-TrFE) hysteresis curves of our devices is shown in Figure 2.3. A displacement charge $D(E)$ in Figure 2.3 is defined as following:

$$D(E) = P(E) + \varepsilon_r \varepsilon_0 E \tag{2.1}$$

Here E denotes an externally applied electric field, $P(E)$ – a polarization of the ferroelectric capacitor, ε_0 – the permittivity of vacuum and ε_r – the relative permittivity of the ferroelectric material – P(VDF-TrFE) which was found to be 10 based on the series of impedance spectroscopy measurements.
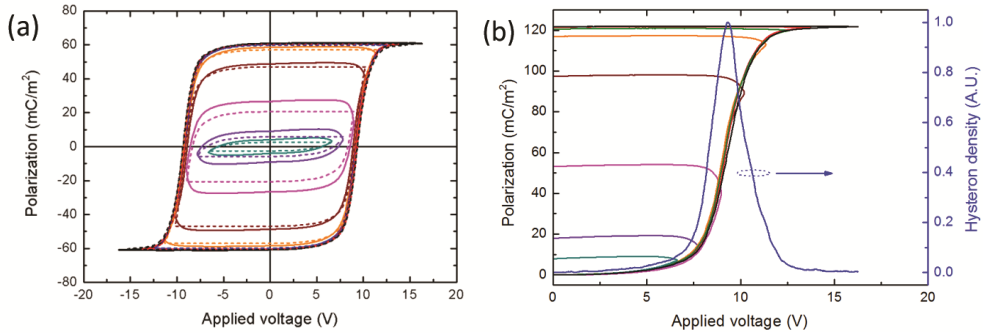
Figure 2.2: (a) Solid lines: ferroelectric polarization charge *P* versus applied voltage *V* hysteresis loops measurements of a 200 nm thick P(VDF-TrFE) ferroelectric capacitor. Dashed lines represent the corresponding calculated ferroelectric hysteresis loops on basis of the dipole switching theory. (b) Ascending ferroelectric hysteresis loops taken from Figure 2.2a and plotted from the same starting point (left axis). Hysteron distribution function used in the DTS simulations (right axis).
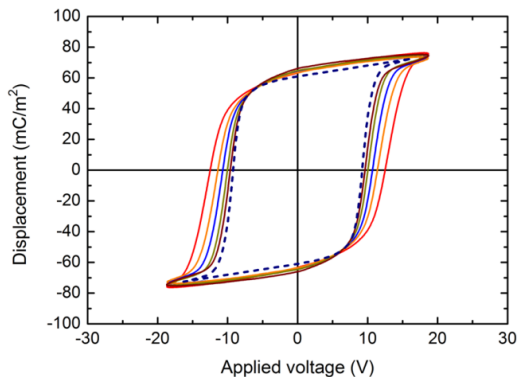
Figure 2.3: Displacement charge *D* versus applied voltage *V* hysteresis loops measured on a 200 nm thick Au/P(VDF-TrFE)/Au capacitor at different frequencies: 100 Hz, 50 Hz, 25 Hz, 10 Hz, 5 Hz. The dashed curve represents the DST-based calculated displacement charge (*D*) versus applied voltage (*V*) hysteresis loop at 1 Hz.

2.2.2 Dipole switching theory (DST)

The analysis of the measured ferroelectric hysteresis loops shown in Figure 2.2a was done according to the dipole switching theory (DST).[13,14] In contrast to behavioral models like Miller's concept,[21] the DST is a practical and accurate physical model based on the Preisach theory for extrinsically switching ferroelectrics.[15] It includes the possibility of consistently modeling inner and saturated loops and it is capable of taking into account history dependent effects. Similarly to the Preisach theory the DST considers a ferroelectric

material as a collection of micro dipoles (hysterons) where each hysteron has two normalized spontaneous polarization states and corresponding coercive fields U_0, V_0 (see Figure 2.4a). Each hysteron behaves as a perfect ferroelectric – its polarization can be flipped by application of a well-defined electric field, yielding rectangular 'microscopic' polarization loops. An aggregation of hysterons typically leads to a distribution of coercive fields. A 2D projection of this Preisach distribution function (V, U) is represented by the Preisach plane shown in Figure 2.4b. The shaded triangular area corresponds to all possible types of hysterons present in a ferroelectric material. However, in contrast to the general case considered in Preisach theory the DST hysterons possess symmetric coercive voltages
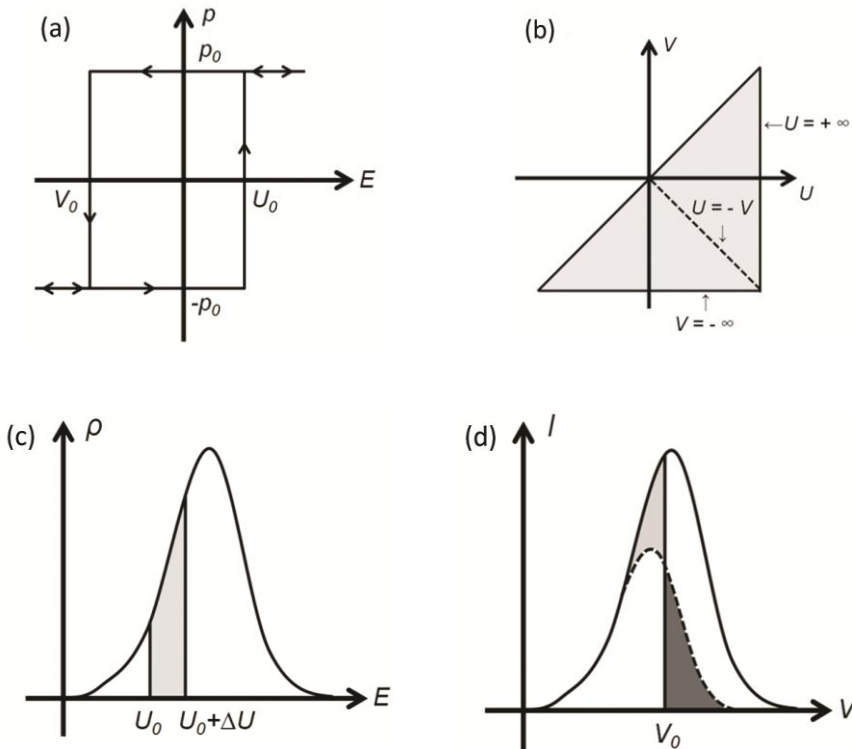
Figure 2.4: Basic concepts of the Preisach model and the dipole switching theory (DST). (a) Polarization hysteresis loop of a single Preisach hysteron. (b) Schematic representation of the Preisach plane. The dashed line corresponds to the DST case where $V_0 = -U_0$. (c) Schematic representation of the hysteron distribution along the dashed line in (b), *i.e.* in the DST case. The shaded area shows hysterons having coercive fields in the range [U_0, $U_0 + \Delta U$]. (d) Schematic representation of the broadening effect discussed in the text. The solid and dashed distributions represent the actually flipped hysterons upon full and partial switching the ferroelectric capacitor, respectively. The vertical solid line corresponds to the maximum applied voltage used for partial switching. The dark and light shaded areas respectively represent hysterons that, in comparison to the situation without broadening, are and are not switched.

$\pm U_0$. In this case the distribution function is confined to a limited part of the Preisach plane, namely the dashed line shown in Figure 2.4b. Alternatively the DST hysteron distribution function can be represented by a 2D plot as shown in Figure 2.4c. Each point on the curve represents the relative density ρ of hysterons having a coercive field U_0. E.g. the shaded area in Figure 2.4c corresponds to hysterons having coercive fields in the range of $\pm$ [U_0, $U_0+\Delta U$].

In terms of the Preisach model the inner loops in Figure 2.2a correspond to a partially filled hysteron distribution function. Figure 2.2b shows ascending hysteresis loops taken from Figure 2.2a and plotted from the same level together with the hysteron distribution function used in the DST simulations. An important finding in Figure 2.2b is that all measured inner loops follow the same ascending curve. This means that the hysteron distribution function can be gradually filled. An important concern regarding the applicability of the DST model to our system is related to the average domain size in the P(VDF-TrFE) material. This is because the applicability of Preisach-type models demands that the domains are small compared to the size of the device. In (unpublished) previous work we used scanning probes to locally pole and switch ferroelectric P(VDF-TrFE) film. Individual domains with an average size much smaller than 100 nm were observed, which is in line with previously reported values.[22,23] That is orders of magnitude smaller than the size of the devices investigated here. In other words, the organic ferroelectric copolymer P(VDF-TrFE) seems to meet all the requirements to be described in terms of the DST mentioned above.

A next step was to study in detail the hysteron distribution function of the P(VDF-TrFE) ferroelectric capacitor. To do this the saturated hysteresis loop was fitted in the framework of the DST. For a given externally applied electric field a polarization of the ferroelectric capacitor is calculated according to the following expression:

$$P(U_0) = \int_0^{|U_0|} \text{sgn}(\ E\ ) \rho (|E|) dE \qquad (2.2)$$

Here U_0 denotes an externally applied field, $\rho(E)$ is the hysteron distribution function.

The history dependent effects are taken into account by keeping track of the applied fields to the capacitor and the corresponding polarization values of the ferroelectric. For example in case of the hysteron distribution function filled according to the advanced preparation scheme, shown in Figure 2.5a,b, the resultant polarization of the ferroelectric capacitor can be calculated as following:

$$P = \int_0^{V_4} \rho(E)dE + \int_{V_3}^{V_2} \rho(E)dE + \int_{V_1}^{V_0} \rho(E)dE - \int_{V_4}^{V_3} \rho(E)dE - \int_{V_2}^{V_1} \rho(E)dE \qquad (2.3)$$

Here the first three terms correspond to the parts of the hysteron distribution function filled with positively oriented hysterons (up), whereas the last two terms – to the negatively oriented hysterons (down).
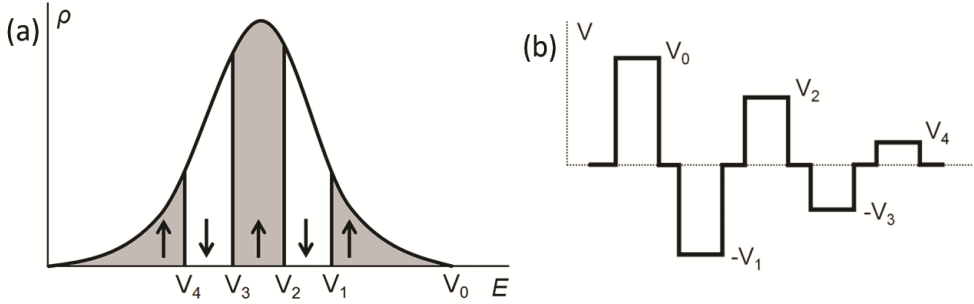
Figure 2.5: (a) Schematic representation of the hysteron distribution function filled according to the preparation scheme in panel (b).

The dashed black curve in Figure 2.2a demonstrates the excellent quality of the resulting fit; the corresponding hysteron distribution function is shown in Figure 2.2b. The obtained hysteron distribution function was subsequently used for simulating the inner hysteresis loops without any further parameter adjustments. The dashed curves in Figure 2.2a show the corresponding predicted inner polarization loops of the P(VDF-TrFE) capacitor. Although the overall agreement is quite good, some systematic differences arise, especially at intermediate applied voltages where the measured inner loops show larger values for the saturated polarization as compared to the simulated loops. This is most likely due to the broadening effect explained in Figure 2.4d: there is some fraction of hysterons with coercive fields above the maximum applied field that is still switched, as well as some (smaller) fraction of hysterons with coercive fields below the maximum applied field that are not switched. In Figure 2.4d solid and dashed curves represent the switching charges measured upon fully and partially inverting the polarization of a ferroelectric capacitor, respectively. The solid line indicates the maximum applied voltage V_0 used for partial switching. Shaded light and shaded dark areas represent hysterons that are not switched respectively additionally switched due to the broadening effect. This means that upon partial poling the broadening effect significantly changes the shape and the integral of the actual hysteron distribution function. Assuming a more or less constant shape of the broadening function the largest difference between measured and simulated loops is expected for inner loops close to the maximum of the hysteron distribution function. This is indeed observed, as seen in the 3rd curve, counted from the smallest loop, of Figure 2.2a. Since the DST does not account for any broadening effects we can conclude that the calculated data is in a good agreement with the experimental results.

2.2.3 Multi-bit states in P(VDF-TrFE)-based capacitor

A next step was to study in more detail the partial filling and reading of the hysteron distribution function of the P(VDF-TrFE) ferroelectric capacitor. To do that a specific polarization state of the ferroelectric was prepared and subsequently probed. Again the quasi-static approach of the DWM was used. Figure 2.6a,b show the filling and probing of the hysteron distribution function of the P(VDF-TrFE) ferroelectric capacitor. Colored solid curves are the switching current of the ferroelectric capacitor as prepared by the signals shown in the left insets. The first pulse of the preparation signal was used for erasing previous memory effects and preparing a fully up (a) or down (b) polarized ferroelectric capacitor. The second pulse of the preparation signal created the desired polarization state of the ferroelectric. The right insets give a schematic representation of the expected hysteron distribution functions as prepared by the corresponding preparation signals. Positive and negative signs represent the two possible orientations of hysterons: up or down. Colored vertical dashed lines correspond to the amplitude of the variable second pulse of the preparation signal shown in the left insets.

To probe the created polarization state of the ferroelectric capacitor two probing triangular pulses were used. In order to probe the state of the entire hysteron distribution the amplitude of the probing pulses was chosen to be higher than the coercive voltage of the ferroelectric capacitor. The sign of the readout pulse was such that hysterons switched in the second preparation pulse are read out, *i.e.* are switched again and give rise to a current response. It is important to stress that in this probing scheme hysterons with a polarization state that corresponds to the first preparation pulse do not give a current response. Black solid curves correspond to the switching of a fully polarized ferroelectric capacitor, *i.e.* the
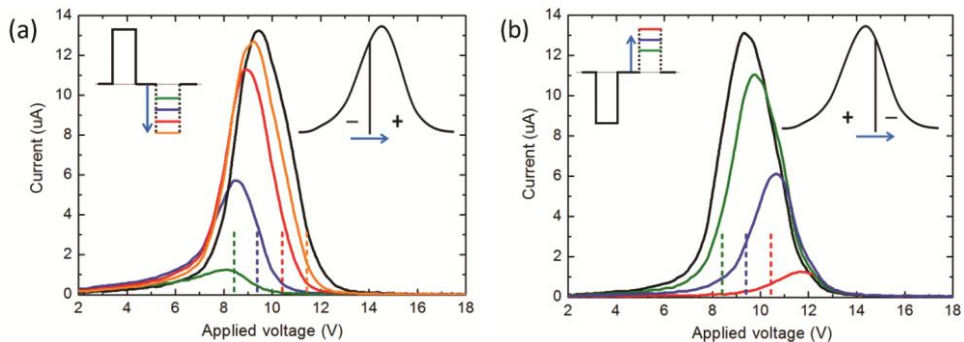
Figure 2.6: Filling and probing a distribution function of a 200 nm thick Au/P(VDF-TrFE)/Au ferroelectric capacitor. Colored solid curves describe the switching of the ferroelectric capacitor with the distribution function filled with negatively oriented hysterons from the left (see Figure 2.6a) and right side (see Figure 2.6b). Left insets: corresponding preparations signals. Right insets: schematic representation of the resulting hysteron distribution functions. Colored dashed lines indicate the amplitudes of the variable 2nd part of the preparation signals shown in the left insets.

largest amplitude of the second polarization pulse. The measured signals in Figure 2.6a,b show that hysterons with low and high coercive fields can be poled in opposite directions: the readout peak grows with the (magnitude of the) second preparation pulse, and, importantly, maintains its shape with a maximum shifting to the higher (see panel a) or lower voltage (see panel b). This means that the hysteron distribution function can indeed be gradually filled as described in the right-side insets of Figure 2.6. It should also be noted that the current traces in Figure 2.6 extend beyond the dashed lines, i.e. the magnitude of the second preparation pulse. This is another manifestation of the broadening effect discussed in Figures 2.2 and 2.4.

The important consequence of the data in Figure 2.6 is that the polarization of any ferroelectric material that follows the DST can contain more information than just 'up' or 'down'. A well-known consequence is that the total polarization state of ferroelectrics can be continuously tuned between full polarization in up and down directions. This underlies the multi-level memory demonstrated in Ref. 12. However, the mean of a distribution does not contain the full information. In particular, we shall demonstrate below that the possibility to tailor the distribution function can be used to store multi-bit information in a single memory element.

Figure 2.7 demonstrates 3-bit data storage realized in a single P(VDF-TrFE) ferroelectric capacitor. The figure displays the most demanding polarization states '010' and '101' with black and red solid curves respectively. The left and right insets describe the preparation signals and a schematic representation of the corresponding hysteron distribution functions. Colored dashed lines correspond to the amplitudes of the last two pulses of the preparation signals shown in the left inset. Like in Figure 2.6 the first pulse of the preparation signal fully polarized the ferroelectric capacitor. The second and the third pulses subsequently created the desired polarization state of the ferroelectric as sketched in the right insets. As before two triangular probing pulses were used for reading out the
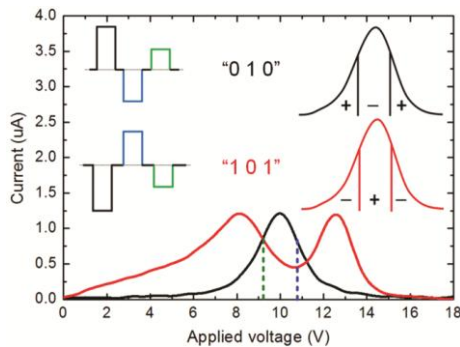
Figure 2.7: 3-bit data storage in a single 200 nm thick Au/P(VDF-TrFE)/Au ferroelectric capacitor. Left insets: preparation signals. Right insets: schematic representations of the corresponding hysteron distribution functions. Colored vertical dashed lines represent the amplitudes of the last two pulses of the preparation signals shown on the left insets. The readout voltages are positive such that 'down' hysterons give a current response.

created polarization states of the ferroelectric. Clearly '010' and '101' preparation pulses give rise to well distinguishable peaks and valleys at the anticipated positions: the data storage is binary. Hence three bits of information can be stored in such single memory element.

Although the same ramping speed in the readout pulses was used in Figures 2.6 and 2.7, the current signal in the latter was much reduced. The reason is the broadening effect discussed before. Especially in the '101' response (red line) it is clear that the middle part of the distribution function not completely separates the outer two. Since the probing scheme measures, at each point in the distribution function, the difference between the up and down fractions, this leads to the observed signal reduction. As a consequence, the '010' state cannot be obtained unambiguously by subtraction of the '101' state from the '111' state in our device. The latter corresponds to the fully switched ferroelectric polarization shown by the black lines in Figure 2.6 a and b. In passing we also note that the lowest peaks in Figure 2.6 (green in panel a and red in b) correspond to the '100' and '001' signals.

Finally, we should address some practical aspects of these devices. First, these devices were not optimized in any way. Au and P(VDF-TrFE) were taken for ease of fabrication and availability. However, P(VDF-TrFE) is known for its excellent retention and great environmental stability. All programmed signals were stable over at least several tens of hours suggesting that the hysteron distribution function is time stable. Moreover all measured devices showed good state reproducibility, as may be expected from the simple processing, and therefore may be expected to have a potentially great scalability.

2.3 Conclusions

In summary, we have introduced multi-bit data storage with binary readout from a simple capacitor structure. The working principle of our multi-bit device is completely general and only demands the applicability of the dipole switching theory (DST). The DST considers ferroelectric material as a collection of micro dipoles (hysterons) described by a specific Preisach distribution function. We showed experimentally that the organic ferroelectric copolymer P(VDF-TrFE) meets all the requirements to be described in terms of the DST. All basic ferroelectric properties together with the hysteron distribution function of P(VDF-TrFE) ferroelectric capacitors were studied using the quasi-static double-wave method. In addition, ferroelectric properties of the device were modeled in the framework of the DST. Finally, we demonstrate a 3-bit data storage element. As a first example we show the possibility to independently program and subsequently read out the lower, middle and upper parts of the hysteron distribution function, yielding a 3-bit memory in a single capacitor structure. All measured devices show good state reproducibility, high endurance and potentially great scalability. Hence we expect that our findings will be

interesting for the realization of multi-bit organic ferroelectric-based memories for low-cost large area electronics.

2.4 Experimental

Poly(vinylidene fluoride-trifluoroethylene P(VDF-TrFE) (M_n = 220 kDa, 2.3 < D < 2.8 with a 77/23 VDF/TrFE ratio) was supplied by Solvay Specialty Polymers. Devices were made by spin-coating a 200 nm thick film of P(VDF-TrFE) ferroelectric polymer on top of glass substrates with patterned gold electrodes: 1.2 × 1.2 mm^2, 700 × 700 μm^2, 400 × 400 μm^2, 250 × 250 μm^2. After spin coating, the films were annealed for 1 hour at 135 °C followed by the deposition of the top Au electrode thorough a shadow mask. Using surface profilometry the layer thickness of the P(VDF-TrFE) was determined to be ≈ 200 ± 10 nm. *P-V* characteristics and the properties of the hysteron distribution function were measured using an Agilent function generator 33120A (source), an external high speed voltage amplifier Falco Systems WMA-300 and a Keithley picoammeter 6485 (sense).

2.5 References

[1]   H.-S. P. Wong, S. Raoux, S. Kim, J. Liang, J.P. Reifenberg, B. Rajendran, M. Asheghi, K.E. Goodson, Phase change memory, *P. IEEE* **2010**, *98*, 2201.

[2]   F. Verbakel, S.C.J. Meskers, R.A.J. Janssen, H.L. Gomes, M. Cölle, M. Büchel, D.M. de Leeuw, Reproducible resistive switching in nonvolatile organic memories, *Appl. Phys. Lett.* **2007**, *91*, 192103.

[3]   M. Cölle, M. Büchel, D.M. de Leeuw, Switching and filamentary conduction in non-volatile organic memories, *Org. Electron.* **2006**, *7*, 305.

[4]   Q.-D. Ling, D.-J. Liaw, C. Zhu, D.S.-H. Chan, E.-T. Kang, K.-G. Neoh, Polymer electronic memories: materials, devices and mechanisms, *Prog. Polym. Sci.* **2008**, *33*, 917.

[5]   P. Heremans, G. H. Gelinck, R. Müller, K.-J. Baeg, D.-Y. Kim, Y.-Y. Noh, Polymer and organic nonvolatile memory devices, *Chem. Mater.* **2011**, *23*, 341-358.

[6]   B.H. Park, B.S. Kang, S.D. Bu, T.W. Noh, J. Lee, W. Jo, Lanthanum-substituted bismuth titanate for use in non-volatile memories, *Nature* **1999**, *401*, 682.

[7]   I. Jung, J.Y. Son, A nonvolatile memory device made of a grapheme nanoribbon and a multiferroic BiFeO$_3$ gate dielectric layer, *Carbon* **2012**, *50*, 3854.

[8]   I. Stolichnov, S.W.E. Riester, H.J. Trodahl, N. Setter, A.W. Rushforth, K.W. Edmonds, R.P. Campion, C.T. Foxon, B.L. Gallagher, T. Jungwirth, Non-volatile ferroelectric control of ferromagnetism in (Ga,Mn)As, *Nat. Mater.* **2008**, *7*, 464.

[9]   T. Kawahara, K. Ito, R. Takemura, H. Ohno, Spin-transfer torque RAM technology: review and prospect, *Microelectron. Reliab.* **2012**, *52*, 613.

[10]   R.C. Sousa, I.L. Prejbeanu, Non-volatile magnetic random access memories (MRAM), *C. R. Phys.* **2005**, *6*, 1013.

[11]   A.K. Tripathi, A.J..J.M. van Breemen, J. Chen, Q. Gao, M.G. Ivan, K. Reimann, E.R. Meinders, G.H. Gelinck, Multilevel information storage in ferroelectric polymer memories, *Adv. Mater.* **2011**, *23*, 4146.

[12]   D. Lee, S.M. Yang, T.H. Kim, B.C. Jeon, Y.S. Kim, J.-G. Yoon, H.N. Lee, S.H. Baek, C.B. Eom, T.W. Noh, Multilevel data storage memory using deterministic polarization control, *Adv. Mater.* **2012**, *24*, 402.

[13]   L. Wang, J. Yu, Y. Wang, G. Peng, F. Liu, J. Gao, Modeling ferroelectric capacitors based on the dipole switching theory, *J. Appl. Phys.* **2007**, *101*, 104505.

[14]   F. Yang, M.H. Tang, Y.C. Zhou, X.J. Zheng, F. Liu, J.X. Tang, J.J. Zhang, J. Zhang, C.Q. Sun, A model for the polarization hysteresis loops of the perovskite-type ferroelectric thin films, *Appl. Phys. Lett.* **2007**, *91*, 142902.

[15]   C.H. Tsang, C.K. Wong, F.G. Shin, Modeling saturated and unsaturated ferroelectric hysteresis loops: An analytical approach, *J. Appl. Phys.* **2005**, *98*, 084103.

[16]   Y.J. Park, J. Chang, S.J. Kang, C. Park, Polarization retention of thin ferroelectricya capacitors, *Appl. Phys. Lett.* **2009**, *95*, 102902.

[17]   K.-H. Kim, Properties of ferroelectric VDF-TrFE copolymer capacitors directly deposited on Si wafers, *J. Korean Phys. Soc.* **2008**, *52*, 88.

[18]   M. Fukunaga, Y. Noda, Improvement of the double-wave method for ferroelectric hysteresis loops and its application to multiferroic $EuMn_2O_5$, *J. Korean Phys. Soc.* **2009**, *55*, 888.

[19]   M. Fukunaga, Y. Noda, New technique for measuring ferroelectric and antiferroelectric hysteresis loops, *J. Phys. Soc. Jpn.* **2008**, *77*, 064706.

[20]   N. Tsutsumi, X. Bai, W. Sakai, Towards nonvolatile memory devices based on ferroelectric polymers, *AIP Adv.* **2012**, *2*, 012154.

[21]   S.L. Miller, J.R. Schwank, R.D. Nasby, M.S. Rodgers, Modeling ferroelectric capacitor switching with asymmetric nonperiodic input signals and arbitrary initial conditions, *J. Appl. Phys.* **1991**, *70*, 2849.

[22]   B.J. Rodriguez, S. Jesse, S.V. Kalinin, J. Kim, S. Ducharme, V.M. Fridkin, Nanoscale polarization manipulation and imaging of ferroelectric Langmuir-Blodgett polymer films, *Appl. Phys. Lett.* **2007**, *90*, 122904.

[23]   P. Sharma, T. Nakajima, S. Okamura, A. Gruverman, Effect of disorder potential on domain switching behavior in polymer ferroelectric films, *Nanotechnology* **2013**, *24*, 015706.

Chapter 3

Nanoscale ferroelectric diodes

Ferroelectric diodes function by grace of nanoscale phase separation in a blend of a semiconducting and a ferroelectric polymer that is sandwiched between metallic electrodes. In this chapter, various scanning probe techniques are combined with numerical modeling to unravel their operational mechanism. Resistive switching is shown to result from modulation of the charge injection barrier at the semiconductor-electrode interfaces. The modulation is driven by the stray field of the polarization charges in the ferroelectric phase, and consequently is restricted to regions where semiconductor and ferroelectric phases exist in close vicinity. Since each semiconductor domain can individually be switched and read out a novel, nanoscale memory element is demonstrated. An ultimate information density of ≈ 30 Mb/cm^2 is estimated for this bottom-up defined memory device.

3.1 Introduction

There exists an ongoing and actually increasing search for novel, non-volatile memory elements. Any viable novel technology in this direction should offer low cost, easy processing, high on/off ratio, scalability, good endurance and easy readout. For the latter, it is strongly preferred to read the (binary) data directly in the form of a high or low current or resistance, rather than indirectly via *e.g.* detection of a (lack of) response of a polarization switching pulse. The simplest and cheapest resistance readout scheme, the crossbar array, puts the additional constraint on the memory element that it has to be rectifying in order to prevent crosstalk between neighboring bits.[1] For these reasons significant efforts have been directed at inorganic multiferroic/ferroelectric materials such as $BiFeO_3$ (BFO). In these materials the polarization state directly affects the resistance of the device.[2,3] It was recently demonstrated that lithographically defined $\approx$ 70 nm sized pillars of BFO could be individually switched and read out.[4] Also metal oxide memristors of reduced size were demonstrated[5]; it should however be noted that some of these devices do not rectify and consequently need additional electronic components in the readout scheme. A major drawback of many such inorganic devices is the need for advanced materials engineering and complicated device fabrication.[6,7] Very recently it was shown that 100 nm sized pillars of the organic ferroelectric P(VDF-TrFE) could be created by an imprinting process and could be ferroelectrically switched and read out by a scanning probe tip.[8] Due to the insulating nature of P(VDF-TrFE) these structures cannot be read out resistively.

An extremely promising alternative was recently proposed by Asadi *et al.*, who showed in a series of papers that thin, phase separated films of a blend of a ferroelectric and a semiconducting polymer fulfill the criteria listed above. A major advantage of this approach is that the (ferroelectric) switching and (resistive) readout functionalities are distributed over different materials and consequently can be individually optimized.[9,10] The crucial ability to downscale the bit size was, however, not experimentally addressed. Moreover, the operational mechanism has so far remained disputed.[11]

The structure and the proposed working principle of the device are described in Chapter 1. It has to be noted that the ferroelectric diode makes it possible to combine the key properties of the ferroelectrics (non-volatile data storage) with the beneficial properties of the semiconductors (conductivity/rectification) in one device. Such fully organic rewritable memory element has great potential for memory applications as it can be driven in a simple crossbar array.[12]

In this chapter, we address the related questions regarding the unknown operational mechanism of these devices, and their minimal bit size. We demonstrate that the resistivity of individual, nanosized semiconductor domains can be switched and read out. In contrast to their inorganic counterparts, these nanostructures spontaneously form in a bottom-up process – spinodal decomposition during film drying.[13] In addition, our results prove that the stray field of the ferroelectric polarization effectively in- or decreases the

injection barrier in the vicinity of the semiconductor/ferroelectric interface. The modulation of theinjection barrier translates into the resistance modulation that is used for read out. These findings point at an interesting parallel between the present organic devices and the switching in inorganic BFO diodes: in both cases the ferroelectric polarization modulates a Schottky-like injection barrier.[4,11]

3.2 Results and discussion

3.2.1 Morphology and ferroelectric properties of the blend at the local scale

The active layer in this work is formed by a continuous film of a 1:9 wt/wt blend of F8BT and P(VDF-TrFE). The film was spincoated on top of glass substrates with patterned gold electrodes and annealed at 135 °C for 1 hour to enhance the crystallinity of the ferroelectric phase. Using surface profilometry we determined the layer thickness of the P(VDF-TrFE):F8BT blend to be ≈ 200 nm.

First, the morphology and the ferroelectric properties of the P(VDF-TrFE):F8BT blend at the nanoscale were characterized. The switching voltage of a capacitor with this layer thickness, based solely on the ferroelectric component of the blend, was found at ≈ |10| V. This corresponds to a coercive field (E_C) of approximately 50 MV/m of the ferroelectric polymer.[14] Figure 3.1a shows a typical topography of a ferroelectric diode without the top electrode obtained by atomic force microscopy (AFM). The topography image clearly shows that the blend consists of round, 300 – 750 nm sized semiconducting (F8BT) domains in a homogeneous crystalline ferroelectric P(VDF-TrFE) matrix, in line with previous observations using other polymer semiconductors.[13,15] Both semiconducting and ferroelectric phases are essentially pure, *i.e.* phase separation is (almost) 100 %.[13] The thickness of the inner part of the F8BT domains is in most cases less than the thickness at the perimeter, *i.e.* most domains are concave. In order to probe the ferroelectric properties of the blend, the inner part (10×10 μm^2) of Figure 3.1a was polarized by applying – 15 V (*i.e.* above the coercive voltage of ≈ |10| V of the ferroelectric film) to the AFM tip while scanning in contact-mode. Figure 3.1b shows the corresponding piezoresponse force microscopy (PFM) image of the complete area after poling. The dark region of the image corresponds to the polarized region, oriented from the bottom contact to the surface of the blend. The PFM signal comes only from the ferroelectric phase of the blend, not from the semiconducting phase of the blend. In general, written patterns were stable over at least several tens of hours meaning that the depolarization effects[16-18] are negligible on this time-scale. Scanning with a reverse bias (*e.g.* + 15 V) inverted the polarization state (not shown). We find that the devices can be reversibly switched by AFM for many cycles without noticeable traces of degradation.
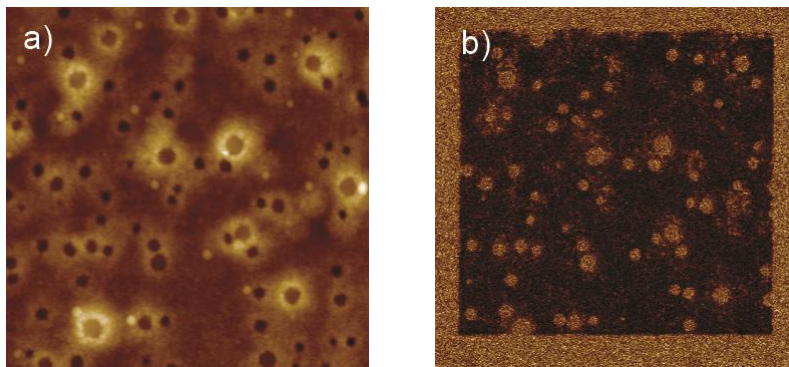
Figure 3.1: PFM-images (12.5×12.5 μm^2) of a P(VDF-TrFE):F8BT (9:1 w/w) blend cast on Au electrode (a) Topography (total vertical scale 160 nm). (b) Corresponding piezoresponse image (total vertical scale 150 mV). The dark area on the PFM image shows the area polarized by scanning a 10×10 μm^2 area with the tip biased at -15 V, corresponding to upward polarization (oriented from the bottom contact to the surface of the blend).

3.2.2 Electrical properties of the device at the local scale

Now we have established that the polarization state of the ferroelectric phase can be reversibly changed, we address the nanoscale electrical behavior. We recorded the current from the poled region of the blend to investigate the influence of the ferroelectric polarization. Figures 3.2a,b show conductive AFM (C-AFM) topography and current map images taken on the blend at $+15$ V applied to the bottom Au electrode, which provides the same poling conditions as in Figure 3.1. The current distribution image from Figure 3.2b shows an unambiguous correlation between the semiconducting domains in the blend and regions of high local conductivity. Although the sign of the C-AFM current depends on the applied bias, the sign of the charge carriers involved cannot directly be determined on basis of these measurements. Since the energies of highest occupied molecular orbital (HOMO) and lowest unoccupied molecular orbital (LUMO) of F8BT amount to 5.9 eV and 3.3 eV respectively,[19] the gold bottom electrode is most likely to provide hole injection into the F8BT over an injection barrier in the order of 1 eV. The work function of the Pt/Ir AFM tip is similar to or higher than the work function of gold[20,21] and therefore unlikely to facilitate electron injection into F8BT. Hence, we assume to probe hole transport.

A crucial feature of the current map in Figure 3.2b is the enhancement in the extracted current at the perimeter of the semiconductor domains. This is shown in more detail in the cross-sections over three, arbitrarily selected, conducting domains shown in Figure 3.2c. They reveal an approximately up to fivefold current enhancement at the

Figure 3.2: C-AFM–images (10×10 μm^2) of a P(VDF-TrFE):F8BT (9:1 w/w) blend on Au. (a) Topography (total vertical scale 110 nm). A few selected convex domains are marked with white squares. (b) Corresponding current map taken with C-AFM at + 15 V applied bias to the bottom electrode (total vertical scale 120 pA). The applied bias is above the coercive voltage of the ferroelectric layer, meaning that the ferroelectric layer is poled. The white squares correspond to the selected areas on Figure 3.2a. (c) Line sections over three (labeled with colored arrows) conductive domains indicated in Figure 3.2b.

ferroelectric/semiconductor interface. The current profiles therefore form the first experimental proof of the current enhancement in the semiconducting material by the proximity of the nearby ferroelectric material. As such they support the stray field model proposed in Ref. 11 and described in Chapter 1. However, since such fields only exist in close vicinity of the ferroelectric/semiconductor interface, a measurable charge injection from the tip would intuitively only be expected at the perimeter of the semiconducting domains. This is however not observed. Substantial currents are also measured in the middle of the domains, corroborating the absence of significant electron injection from the tip into the F8BT. In contrast, holes that have been injected from the positively biased bottom electrode can move from the perimeter of the semiconductor domains, where they are injected, to the inner part of the domains, leading to a non-zero current being extracted from the center part of the domains. The radius of the tip-sample contact radius was calculated using the Hertz model[22,23] to be about 10 nm. This excludes the instrument resolution as being the reason for the non-zero level of the current in the middle area of the conductive domains. Also from the maximum steepness of the curves in panel c an upper limit for the contact radius can be estimated as 20 nm, further excluding a limited resolution as cause for the finite current in the middle of the semiconductor domains. Moreover, comparison between the tip-sample contact radius and the typical domain size eliminates cross-correlation between topographical features of the blend and the measured current enhancement at the perimeter of the semiconductor domains. Finally, an independent confirmation of this experiment was successfully performed and described in Appendix A.
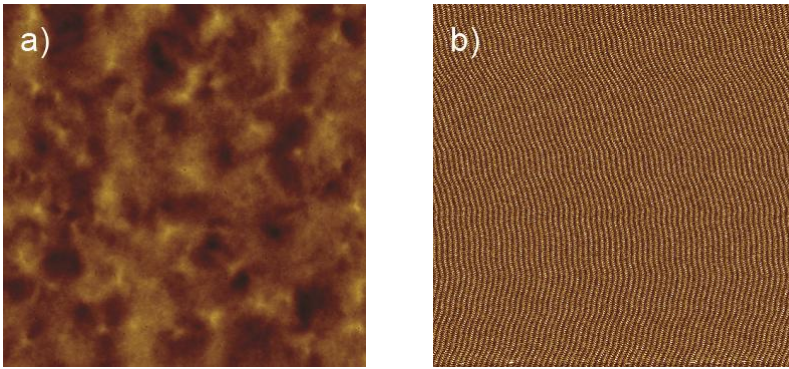
Figure 3.3: C-AFM–images (10×10 µm^2) of a F8BT on Au. (a) Topography (total vertical scale 20 nm). (b) Corresponding current map at + 20 V applied bias (total vertical scale 0.8 pA). The C-AFM image shows no current above the sensitivity of the C-AFM setup ($\approx$ 1 pA).

To exclude the possibility that the current in Figure 3.2b is due to the large field at the apex of the tip[24,25] and not related to the ferroelectric polarization, the same measurements were done on pure F8BT films. In case of pure F8BT there is no sign of any current above the sensitivity ($\approx$ 1 pA) of the C-AFM setup, even at larger applied voltages (see Figure 3.3).

An important finding in Figure 3.2a,b is the fact that most convex domains carry no measurable current and the concave domains are mainly responsible for the current in the device. In the convex domains the current is most likely blocked by a thin layer of P(VDF-TrFE). Because P(VDF-TrFE) is an excellent insulator, a 10 nm thick P(VDF-TrFE) film would be sufficient for complete blocking of the charge transfer. From an application point of view, the non-contributing convex domains are to be avoided. To analyze this in more detail, additional AFM images of the blend on smaller areas were recorded in tapping (or intermittent contact) mode (TM). Figure 3.4a shows a few convex and concave domains marked with circles and squares respectively. Since TM-AFM phase imaging provides detailed nanometer-scale information about surface visco-elastic properties it can readily detect variations in top layer composition. The TM-AFM phase image shown in Figure 3.4b shows a clear contrast between F8BT (dark) and the stiffer (bright) regions of the crystallized P(VDF-TrFE) in both convex and the concave domains. This strongly suggests that the top surface in all domains consists of F8BT. In the convex domains the F8BT phase does not extend all the way down to the bottom electrode but is effectively interrupted by a buried layer of P(VDF-TrFE).
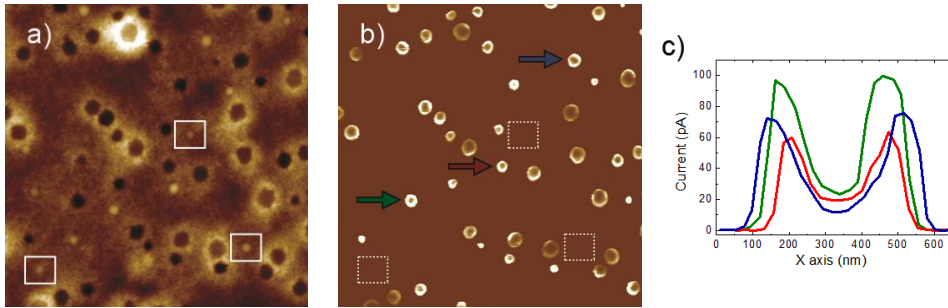
Figure 3.4: TM-AFM–images (5×5 μm^2) of a P(VDF-TrFE):F8BT (9:1 w/w) blend on Au. (a) Topography (total vertical scale 110 nm). A few selected convex and concave domains are marked with white circles and squares respectively. (b) Phase (total vertical scale 120 deg). The white circles and squares correspond to the selected areas on Figure 3.4a.

Further insight in the electrical connectedness of the concave and convex domains to the bottom electrode can be obtained from scanning kelvin probe microscopy (SKPM). Figure 3.5a,b show SKPM images measured on the P(VDF-TrFE):F8BT blend. Comparison between the surface potential map and simultaneously recorded topographical image reveals that the bright spots correspond to the F8BT domains, whereas the dark background is related to the P(VDF-TrFE) matrix. The presence of such pronounced contrast cannot be explained in terms of metal-insulator-metal model where the surface potential is determined by the work function difference between the Pt/Ir AFM tip and the Au bottom electrode. The measured variation of the surface potential over the semiconducting domains is most likely due to the positive charge accumulation at the interface between F8BT and bottom Au electrode.[26] The carrier density in the semiconductor at the bottom contact interface is related to the magnitude of the hole injection barrier. Since this barrier is much larger for the ferroelectric part of the blend the bright spots correspond to the semiconducting phase. Another important issue is that the surface potential over the convex domains is remarkably lower than the surface potential measured on the concave ones, see circles in Figure 3.5a,b. Moreover, the surface potential map reveals the mismatch between the topographical size of the convex domains and the corresponding surface potential profiles. These effects are most likely due to the presence of an insulating layer underneath the convex F8BT domains and also because the convex domains are partially buried in the ferroelectric matrix.
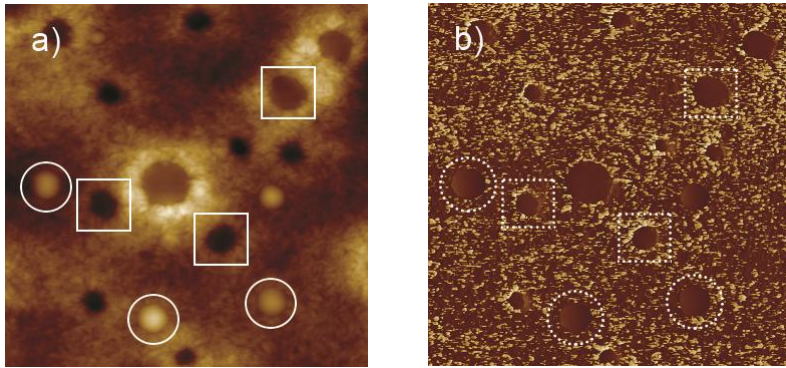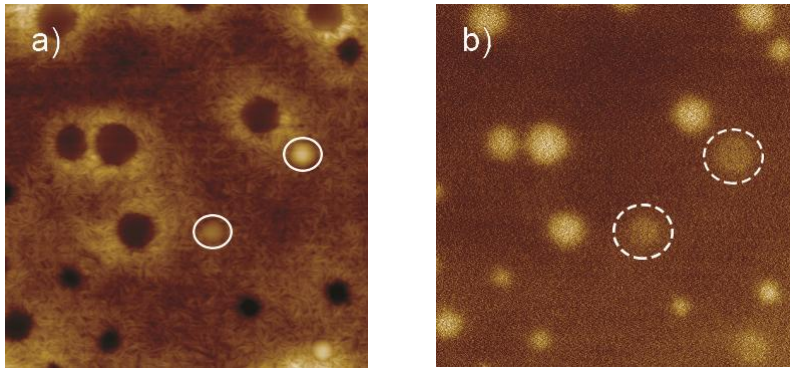
Figure 3.5: AFM-SKPM–images (5×5 µm^2) of a P(VDF-TrFE):F8BT (9:1 w/w) blend on Au (a) Topography (total vertical scale 110 nm). Two selected convex domains are marked with white circles. (b) Corresponding surface potential map (total vertical scale 0.2 V). The white circles correspond to the selected areas on Figure 3.5a.

3.2.3 Modeling of the electrical properties of the device at the local scale

In order to interpret the measurements presented above in more detail a 2D model of the ferroelectric diode was developed. The phase separated morphology is simplified to a 2D structure of alternating ferroelectric and semiconducting slabs (see Figure 1.5c, Chapter 1). Motion of electrons and holes is described by the transport, continuity and Poisson equations that are numerically solved on a rectangular grid.[11,27,28] The parameters of the blend used in the simulation and the electrical transport model are explained in detail in the Experimental Section and Appendix A respectively.

First the C-AFM measurements were simulated. A 2D representation of the current distribution in a single semiconducting domain shows that the charge carriers are injected at the ferroelectric/semiconductor interface in agreement with the stray field model (see Figure 3.6). Figure 3.7a shows a joint plot of the measured and the simulated C-AFM data. The colored dotted curves represent normalized C-AFM current line sections measured over five randomly chosen semiconducting domains with a diameter of about 450 nm. The simulated current profile is shown by the black solid curve. There is good agreement between calculated and measured data. Note in particular that the nonzero current in the middle of the semiconductor domain discussed above is reproduced by the simulation. Hence, we conclude that the stray field model is an accurate description of the device operation.
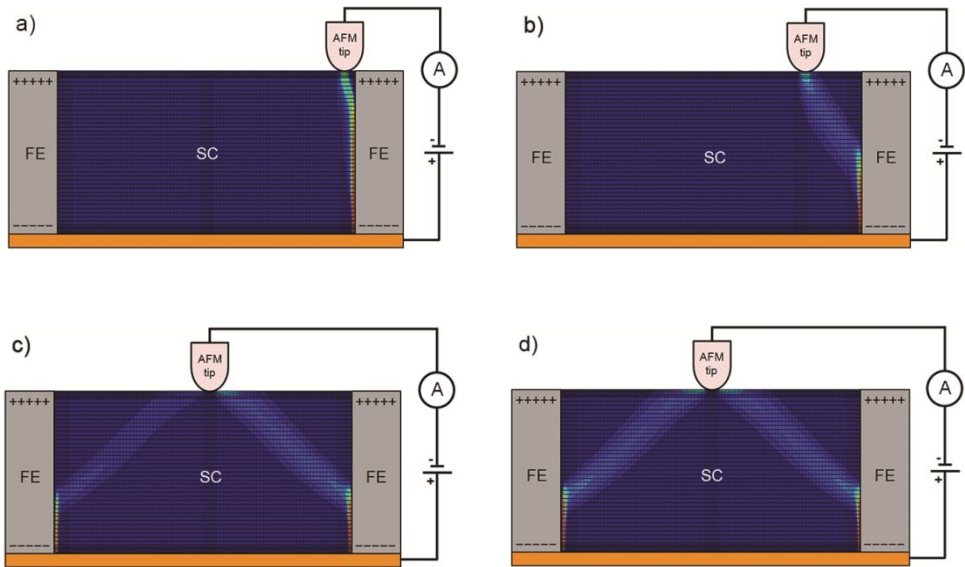
Figure 3.6: 2D simulation of the C-AFM experiments. 2D representation of the current distribution in a single semiconducting domain calculated for four different positions of the AFM probe: (a) edge position (b) intermediate position (c) near middle position (d) middle position. Minuses (−) and pluses (+) indicate polarization charges in the ferroelectric.

SKPM measurements were also simulated, using the same parameter set. Figures 3.7b,c compare measured and calculated SKPM experiments. The gray and the black curves represent experimentally measured and smoothed local surface potential profiles over the semiconducting domains. The red curves show the modeled surface potential profiles over the same domains. The insets describe the structure of the two domain shapes used in the simulations. Figure 3.7b shows the data measured over one of the concave domains shown in Figure 3.5a,b. Such domains are believed to be completed *i.e.* electrically connected to the bottom electrode. The geometrical parameters of the completed domain are derived from the AFM topography image shown in Figure 3.5a. The modeled data is in a good agreement with the measured curve. A small difference at the edges of the peak is most likely related to the partial screening of the ferroelectric polarization charges. Figure 3.7c shows the same comparison as Figure 3.7b for one of the convex domains in Figure 3.5a,b. As it is shown in the inset of Figure 3.7c such domains 'float' in the ferroelectric matrix and are partially buried in it. This means that the real geometrical parameters of such domains cannot be directly measured. Therefore the full diameter of the floating domain was first estimated from the AFM topography image and then corrected on basis of the resultant modeled potential profile. Figure 3.7d shows a joint plot of the measured and the

43
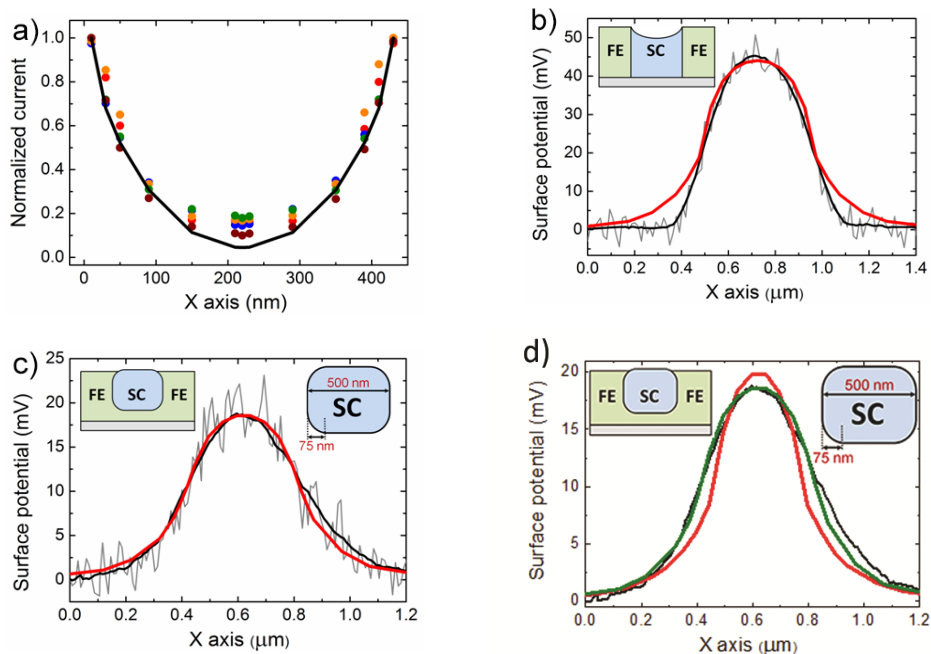
Figure 3.7: Measured and simulated C-AFM and SKPM experiments. (a) Normalized current line sections over five typical conductive domains with a diameter of about 450 nm are shown (different colored symbols). The black line is the calculated profile. (b) Measured and smoothed surface potential profiles over one of the completed domains shown by gray and black curves respectively. The calculated profile is shown in red. The inset shows the structure of the semiconducting domain embedded in the ferroelectric. (c) As panel b for a floating domain. The geometrical parameters of the domain used in the simulation are shown in the right inset. The full diameter and undercut of the domain, are 500 nm and 75 nm, respectively, as shown in the right inset. The topographically estimated diameter is 350 nm. (d) Joint plot of the measured and the calculated potential profiles over the floating semiconducting domain. The black curve is the experimentally obtained smoothed potential profile. Red and green curves represent the modeled potential profiles based on the topographically estimated and corrected geometrical parameters of the semiconducting domain, respectively. The geometrical parameters of the domain used in the simulation are the same as in (c).

calculated potential profiles. The modeled curves are based on both the estimated and the corrected diameters of the semiconducting domains. Thus, the SKPM measurements confirm the structure of the floating semiconducting domains found from the C-AFM and the TM-AFM measurements.

3.2.4. Single domain poling

Using local probing techniques we can investigate the limits of the attainable bit density. Figure 3.8 shows that individual domains can potentially be used as individual information storing bits. The white arrow on the topography image (see Figure 3.8a) points to the domain which was chosen for individual poling. A poling voltage of + 16 V was used. The dark area on the piezoresponse image, Figure 3.8b, shows that the area around this domain has been selectively poled with upward polarization. Figure 3.8c presents the current map. The selected domain displays clear current enhancement as a result of the ferroelectric poling of the surrounding P(VDF-TrFE) matrix. In passing we note that this experimentally confirms that the current switching by the lowering of the effective injection barrier is only driven by the ferroelectric polarization charges in the immediate vicinity of the semiconductor/ferroelectric interface.
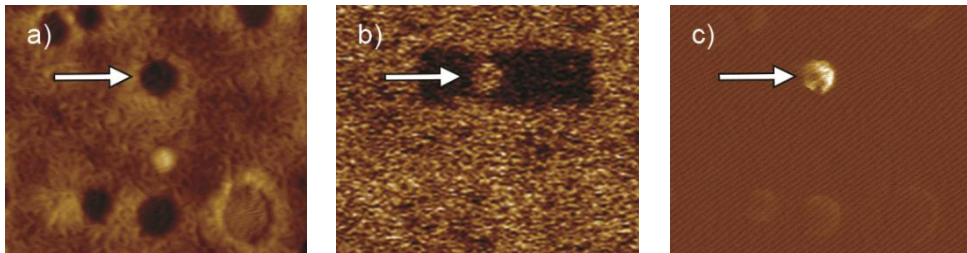
Figure 3.8: PFM– and C-AFM–images (4 × 3.5 µm^2) of a P(VDF-TrFE):F8BT (9:1 w/w) blend on Au after selective poling around a single domain (indicated by the arrow). (a) Topography (total vertical scale 110 nm). (b) Corresponding piezoresponse image (total vertical scale 120 mV). (c) Corresponding current map, subsequently taken with C-AFM at + 6 V bias applied to the back contact (total vertical scale 10 pA).

For the investigated blend, 300 nm is the approximate lower limit on the attainable feature size of the semiconducting domains. Since the writing resolution of *ca.* 100 nm is smaller than this value, the ultimate data density can be estimated as $1/4 \times F^2$, with F the feature size of 300 nm.[11] Note that this feature size is achieved in an electrical readout scheme and is virtually identical to the feature size achieved by Chen *et al.* by reading and writing the polarization state of ferroelectric nano-pillars by PFM.[8] Thus, for a memory crossbar array with properly aligned semiconducting domains at the intersections between word and bit lines a rewritable information density of the order of 30 Mb/cm^2 could in principle be achieved.

3.3 Conclusions

In summary, we have studied the operating mechanism of ferroelectric diodes based on a phase separated blend of ferroelectric and semiconducting polymers at the nanometer scale by a combination of SPM techniques and numerical modeling. We measure a direct correlation between the extracted current from the semiconducting domains and the polarization state of the ferroelectric surrounding the domains. Device operation is therefore intimately linked to the phase separated morphology. Depending on the local polarization state of the P(VDF-TrFE) matrix surrounding a specific domain, the current in that semiconductor domain is enhanced or not. The fact that the current density was found to be higher at the perimeter of the semiconductor domains is unambiguous proof that charges are predominantly injected at the perimeter of the domains. These results are therefore in line with the proposed theoretical model that the stray field of the polarization charges in the ferroelectric phase can modulate charge injection from the electrode into the semiconductor in the regions where semiconductor and ferroelectric phases exist in close vicinity.

Moreover, we have proven that the semiconductor domains can be individually addressed, both in writing and reading. As such, each domain can be regarded as a bottom-up nanosized memory element. For the present blends this translates into a potential maximum memory density in the order of 30 Mb/cm^2, enough for low-cost applications based on printed electronics.

It is, finally, interesting to point out that the operational mechanism of the present ferroelectric diodes is extremely similar to the proposed mechanism of memory diodes based on inorganic ferroelectric materials as BiFeO$_3$. In both cases the ferroelectric polarization charges modulate the Schottky-like barrier for charge injection into the conducting phase.[4,11]

3.4 Experimental

Poly(vinylidene fluoride-trifluoroethylene) P(VDF-TrFE) (M_n = 220 kDa, 2.3 < D < 2.8 with a 77/23 VDF/TrFe ratio) was supplied by Solvay Specialty Polymers. Poly[(9,9-di-n-octylfluorenyl-2,7-diyl)-alt-(benzo[2,1,3]thiadiazol-4,8-diyl)] F8BT (M_n = 13 kDa, D = 2.0) was synthesized according to a modified Suzuki-polymerization.[29,30] Devices were made by spin-coating a 200 ± 10 nm thick film of a 9:1 w/w P(VDF-TrFE):F8BT blend on top of glass substrates with patterned gold electrodes. After spin coating, the films were annealed for 1 hour at 135 °C. Since SPM techniques require a direct contact of the probe with the studied material the deposition of the top contact was omitted meaning that the AFM tip served as a top electrode.

Conductive atomic force microscopy (C-AFM), piezoresponse force microscopy (PFM) and scanning kelvin probe microscopy (SKPM) are employed to locally probe

current pathways, polarization states and electrostatic potentials, respectively. The C-AFM, PFM and SKPM schemes were implemented on a commercial AFM system (Veeco MultiMode NS-IIIA) equipped with an external signal generator/lock-in amplifier. The C-AFM and the PFM measurements were performed using Pt/Ir coated Si tips (Nanosensors, spring constant $k \approx 5$ N/m). The PFM images were acquired using a modulation voltage of 2 $V_{p.p.}$ at a frequency of 100 kHz, *i.e.* well below the first contact resonance. All SPM measurements were performed under ambient conditions. The C-AFM current was detected using a high sensitivity current amplifier (TUNA module, 10^{11} V/A, Veeco). In our setup, C-AFM and PFM could be switched easily without disturbing the alignment of the AFM tip, allowing in situ conductivity and polarization characterization of the same area. The surface potential map was measured using Al coated Si tips (Nanosensors, spring constant $k \approx 12.5$ N/m).

The employed 2D model for ferroelectric diodes takes into account the phase separated morphology. The ferroelectric P(VDF-TrFE) is characterized by a zero mobility because of its insulating properties. In the ferroelectric slab a surface polarization charge density $\sigma_p \approx 70$ mC/m^2 is fixed on the first grid points, 2 nm above the bottom electrode and below the top surface of the blend. A static relative dielectric constant $\varepsilon_r = 10$ was used. The organic semiconducting slab F8BT was characterized by a typical (constant) hole mobility, $\mu_p = 6.5 \times 10^{-11}$ m^2/(V·s) and $\varepsilon_r = 3$. The LUMO and the HOMO levels of the semiconductor are set at around 3.3 eV and 5.9 eV respectively. The hole injection barrier at the bottom electrode is fixed at 0.9 eV. The work function of the AFM probe is estimated to be around 5.6 eV. A field-dependent charge injection into the semiconductor is implemented by using the Emtage/O'Dwyer model.[31,32]

3.5 References

[1] K. Asadi, M. Li, P.W.M. Blom, M. Kemerink, D.M. de Leeuw, Organic ferroelectric opto-electronic memories, *Mater. Today* **2011**, *14*, 592.

[2] T. Choi, S. Lee, Y.J. Choi, V. Kiryukhin, S.-W. Cheong, Switchable ferroelectric diode and photovoltaic, *Science* **2009**, *324*, 63.

[3] A.Q. Jiang, C. Wang, K.J. Jin, X.B. Liu, J.F. Scott, C.S. Hwang, T.A. Tang, H.B. Lu, G.Z. Yang, A resistive memory in semiconducting BiFeO$_3$ thin-film capacitors, *Adv. Mater.* **2011**, *23*, 1277.

[4] S. Hong, T. Choi, J.H. Jeon, Y. Kim, H. Lee, H.-Y. Joo, I. Hwang, J.-S. Kim, S.-O. Kang, S.V. Kalinin, B.H. Park, Large resistive switching in ferroelectric BiFeO$_3$ nano-island based switchable diodes, *Adv. Mater.* **2013**, *25*, 2339.

[5] D.J. Kim, H. Lu, S. Ryu, C.-W. Bark, C.-B. Eom, E.Y. Tsymbal, A. Gruverman, Ferroelectric tunnel memristor, *Nano Lett.* **2012**, 12, 5697.

[6] J. Mannhart, D.G. Schlom, Oxide interfaces – an opportunity for electronics, *Science* **2010**, *327*, 1607.

[7] S.D. Ha, S. Ramanathan, Adaptive oxide electronics: A review, *J. Appl. Phys.* **2011**, *110*, 071101.

[8]   X.-Z. Chen, Q. Li, X. Chen, X. Guo, H.-X. Ge, Y. Liu, Q.-D. Shen, Nano-imprinted ferroelectric polymer nanodot arrays for high density data storage, *Adv. Funct. Mater.* **2013**, *23*, 3124.

[9]   K. Asadi, D.M. de Leeuw, B. de Boer, P.W.M. Blom, Organic non-volatile memories from ferroelectric phase- separated blends, *Nat. Mater.* **2008**, *7*, 547.

[10]   K. Asadi, T.G. de Boer, P.W.M. Blom, D.M. de Leeuw, Tunable injection barrier in organic resistive switches based on phase-separated ferroelectric–semiconductor blends, *Adv. Funct. Mater.* **2009**, *19*, 3173.

[11]   M. Kemerink, K. Asadi, P.W.M. Blom, D.M. de Leeuw, The operational mechanism of ferroelectric-driven organic resistive switches, *Org. Electron.* **2012**, *13*, 147.

[12]   K. Asadi, P.W.M. Blom, D.M. de Leeuw, The MEMOLED: active addressing with passive driving, *Adv. Mater.* **2011**, *23*, 865.

[13]   C.R. McNeill, K. Asadi, B. Watts, P.W.M. Blom, D.M. de Leeuw, Structure of phase-separated ferroelectric/semiconducting polymer blends for organic non-volatile memories, *Small* **2010**, *6*, 4, 508.

[14]   S. Bauer, Poled polymers for sensors and photonic applications, *J. Appl. Phys.* **1996**, *80*, 5531.

[15]   J.J. Michels, A.J.J.M. van Breemen, K. Usman, G.H. Gelinck, Liquid phase demixing in ferroelectric/semiconducting polymer blends: an experimental and theoretical study, *J. Polym. Sci. Part B: Polym. Phys.* **2011**, *49*, 1255.

[16]   P. Wurfel, I.P. Batra, J.T. Jacobs, Polarization instability in thin ferroelectric films, *Phys. Rev. Lett.* **1973**, *30*, 1218.

[17]   P. Wurfel, I.P. Batra, Depolarization-field-induced instability in thin ferroelectric films–experiment and theory, *Phys. Rev. B* **1973**, *8*, 5126.

[18]   I.P. Batra, P. Wurfel, B.D. Silverman, Phase transition, stability, and depolarization field in ferroelectric thin films, *Phys. Rev. B* **1973**, *8*, 3257.

[19]   Y. Zhang, P.W.M. Blom, Electron and hole transport in poly(fluorene-benzothiadiazole), *Appl. Phys. Lett.* **2011**, *98*, 143504.

[20]   C.J. Chen, Introduction to scanning tunneling microscopy; Oxford: Oxford University Press, **1993**.

[21]   D.R. Lire, CRC Handbook of chemistry and physics; 72nd ed.; CRC Press, Boca Raton, **1991**.

[22]   G.G. Adams, M. Nosonovsky, Contact modeling — forces, *Tribol. Int.* **2000**, *33*, 431.

[23]   N.N. Gosvami, S.K. Sinha, W. Hofbauer, S.J. O'Shea, Solvation and squeeze out of hexadecane on graphite, *J. Chem. Phys.* **2007**, *126*, 214708.

[24]   M. Kemerink, S.F. Alvarado, P. Müller, P.M. Koenraad, H.W.M. Salemink, J.H. Wolter, R.A.J. Janssen, Scanning tunneling spectroscopy on organic semiconductors: experiment and model, *Phys. Rev. B* **2004**, *70*, 045202.

[25]   O.G. Reid, K. Munechika, D.S. Ginger, Impact of nanoscale heterogeneity on organic solar cell performance, *Nano Lett.* **2008**, *8*, 1602.

[26]   M. Kemerink, J.M. Kramer, H.H.P. Gommans, R.A.J. Janssen, Temperature-dependent built-in potential in organic semiconductor devices, *Appl. Phys. Lett.* **2006**, *88*, 192108.

[27]   K. Maturova, M. Kemerink, M.M. Wienk, D.S.H. Charrier, R.A.J. Janssen, Scanning kelvin probe microscopy on bulk heterojunction polymer blends, *Adv. Funct. Mater.* **2009**, *19*, 1379.

[28]   K. Maturova, S.S. van Bavel, M.M. Wienk, R.A.J. Janssen, M. Kemerink, Description of the morphology dependent charge transport and performance of polymer: fullerene bulk heterojunction solar cells, *Adv. Funct. Mater.* **2011**, *11*, 261.

[29]   T. van Woudenbergh, J. Wildeman, P.W.M. Blom, J.J.A.M. Bastiaansen, B.M.W. Langeveld-Voss, Electron-enhanced hole injection in blue polyfluorene-based polymer light-emitting diodes, *Adv. Funct. Mater.* **2004**, *14*, 677.

[30]   N. Miyaura, A. Suzuki, Palladium-catalyzed cross-coupling reactions of organoboron compounds, *Chem. Rev.* **1995**, *95*, 2457.

[31]   P.R. Emtage, J.J. O'Dwyer, Richardson-Schottky effect in insulators, *Phys. Rev. Lett.* **1966**, *16*, 356.

[32]   J.J.M. van der Holst, M.A. Uijttewaal, R. Balasubramanian, R. Coehoorn, P.A. Bobbert, G.A. de Wijs, R.A. de Groot, Modeling and analysis of the three-dimensional current density in sandwich-type single-carrier devices of disordered organic semiconductors, *Phys. Rev. B* **2009**, *79*, 085203.

Chapter 4

3D-morphology reconstruction of nanoscale phase-separation in polymer memory blends

In many organic electronic devices functionality is achieved by blending two or more materials, typically polymers or molecules, with distinctly different optical or electrical properties in a single film. The local scale morphology of such blends is vital for the device performance. In this chapter, a simple approach to study the full 3D morphology of phase-separated blends, taking advantage of the possibility to selectively dissolve the different components is introduced. This method is applied in combination with AFM to investigate a blend of a semiconducting and ferroelectric polymer typically used as active layer in ferroelectric diodes. It is found that the blend consists of a ferroelectric matrix with three types of embedded semiconductor domains and a thin wetting layer at the bottom electrode. Statistical analysis of the obtained images excludes the presence of a fourth type of domains. Criteria for the applicability of the presented technique are discussed.

4.1 Introduction

Soluble organic semiconductors are receiving increasing attention as they enable emerging applications such as flexible and low-cost organic photovoltaics (OPV),[1] light emitting diodes (OLED),[2] field effect transistors (OFET),[3] and memories.[4-8] For all these devices, performance can be optimized by blending two components to obtain a (controlled) phase separated morphology. For OPV, the use of separate donor and acceptor moieties is imperative to achieve efficient charge generation.[9] Likewise, data storage in two-terminal organic ferroelectric resistive memories is intimately related to phase separation between the blend components.[10] 3D morphology control in polymer resistive memories has recently been shown to result in enhanced functional device performance.[11,12] High-performance uni- and ambipolar OFETs can be made from phase separated polymer blends.[13] In such blend systems the small molecule component and the polymer binder are responsible for high charge carrier mobility and formation of smooth, uniform films respectively.

Accurate characterization of the blend morphology is challenging due to the relatively high chemical and mechanical similarity of the components and the small length scales involved.[14,15] Although atomic force microscopy (AFM), transmission/scanning electron microscopy (TEM/SEM), and scanning near-field optical microscopy (SNOM) provide sufficient resolution it is quite difficult for these techniques to recognize different components of the blend. In addition, TEM/SEM and SNOM require specific sample preparation and advanced practical knowledge of the setups. It has to be noticed that in most cases direct measurements by AFM provides information only about the topography of the top surface of the blend. Alternatively, scanning transmission X-ray microscopy (STXM) can be used to study the blend morphology, but it requires synchrotron access.[10] Therefore a strong demand exists for a simple and an easily accessible method that can provide detailed information about the 3D-structure of organic blend morphologies at the local scale.

A system in which there is a clear need for enhanced insight in the 3D morphology is the ferroelectric diode,[4-8] described in detail in Chapter 1. The resistivity of such memories can be switched between two distinct levels that retain their states when the power is shut off. Another important feature of the memory is the possibility of non-destructive read out, making the ferroelectric diode an extremely promising candidate for low-cost non-volatile reprogrammable memory applications.[16] Its active layer consists of a phase-separated blend of a ferroelectric and semiconducting polymer processed from a common solution. During casting and solvent evaporation the final blend morphology forms via spinodal decomposition.[17,18] The final dry film consists of semiconducting domains embedded in a polycrystalline ferroelectric matrix.[10] Transport of charge carriers occurs in the semiconducting phase. The underlying switching mechanism is based on a modulation of the injection barrier by the stray field of the ferroelectric polarization charges

in the vicinity of the ferroelectric/semiconductor interface.[19,20] It has been shown that the operation of ferroelectric diodes strongly depends on the 3D-morphology of the phase-separated blend.[10,17] Hence detailed information about the blend structure is not only crucial for complete understanding, but also for further optimization and miniaturization.

In this chapter, we present a combined technique of selective dissolution and statistical analysis – a simple and powerful tool for studying the 3D structure of the blend at submicron length scales. It takes advantage of selective solubility of different components of the blend. Hence different components of the blend are selectively dissolved and the remaining structures together with the as-processed blend are studied by AFM. Combination of all measured topography images gives the possibility to reconstruct the 3D-structure of the blend. The technique should be applicable to any demixed blend system based on components with sufficiently mutual repulsion to allow for selective dissolution and a morphology that is 'sufficiently coarse'; more specific criteria are discussed at the end.

4.2 Results and discussion

4.2.1 Selective dissolution approach

The studied system is a continuous film of a 1:9 wt/wt blend of the polymeric semiconductor F8BT, and the ferroelectric polymer P(VDF-TrFE). The film was spin coated from 50 mg/mL a cyclohexanone (CH) and tetrahydrofuran (THF) mixture (75:25 v/v) on top of glass substrates with gold electrodes (3000 rpm, 60 sec) and annealed at 135 °C for 1 hour to enhance the crystallinity of the ferroelectric phase. Using surface profilometry we determined the average layer thickness of the P(VDF-TrFE):F8BT blend to be $\approx$ 200 nm and the rms (root mean square) roughness to be below 20 nm. All technical details of the selective dissolution procedure can be found in the experimental section and in Ref. 11. As has been proposed for this particular system[11] as well as for such blends with other polymeric semiconductors, like P3HT[4,5] and PFO,[21] the ternary blend of solvent/semiconductor/P(VDF-TrFE) demixes during solvent evaporation to give (for a 9:1 w/w P(VDF-TrFE):F8BT ratio) a dispersed phase of disk-like domains consisting of virtually pure semiconductor in a matrix of P(VDF-TrFE).[10] Despite the fact that this is generally true for all polymeric semiconductors used so far in combination with P(VDF-TrFE), subtle differences remain.

In case of P(VDF-TrFE):F8BT processed from cyclohexanone/THF on gold, the blend films typically exhibit four types of semiconducting domains[11,15] (see Figure 4.1); i) electrically functional 'Type-1' domains that locally bridge the total thickness of the film (see Figure 4.2), ii) electrically non-functional 'Type-2' domains locally protruding from the
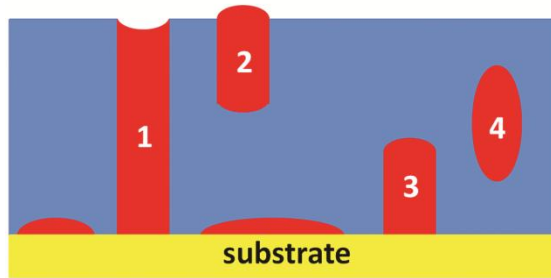
Figure 4.1: Schematic cross-sectional representation of the P(VDF-TrFE):F8BT blend film on gold; F8BT and P(VDF-TrFE) phases are indicated in red and blue, respectively.

top region of the ferroelectric matrix but not connecting to the Au substrate, iii) electrically non-functional 'Type-3' domains, that reside on the substrate but are buried by the matrix phase, iv) fully embedded 'Type-4' domains, and v) very thin (< 30 nm) regions on the substrate comprising F8BT, reminiscent of a 'partial wetting layer'. As the wetting layer can potentially form a semi-continuous layer it is treated separately and not as another domain type. Since the substrate was constantly moved during the dissolution process and flushed with solution afterwards, Type-2 and Type-4 domains were prevented to adhere to the substrate and being wrongly interpreted as Type-3 domains. In passing we note that the observed concave top of Type-1 domains has a beneficial effect on the device performance.
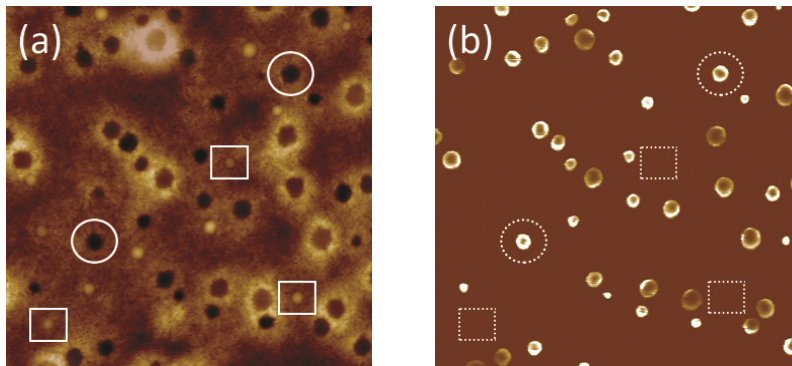
Figure 4.2: C-AFM images ($10 \times 10 \ \mu m^2$) of a P(VDF-TrFE):F8BT (9:1 w/w) blend cast on Au electrode. (a) Topography (total vertical scale 110 nm). A few selected convex and concave domains are marked with white squares and circles respectively. (b) Corresponding current map taken with C-AFM at + 15 V applied bias to the bottom electrode (total vertical scale 120 pA). The applied bias is above the coercive voltage of the ferroelectric layer, meaning that the ferroelectric layer is poled. The white squares and circles correspond to the selected areas on Figure 4.2a, showing that concave (convex) domains are typically (not) connected to the bottom electrode.
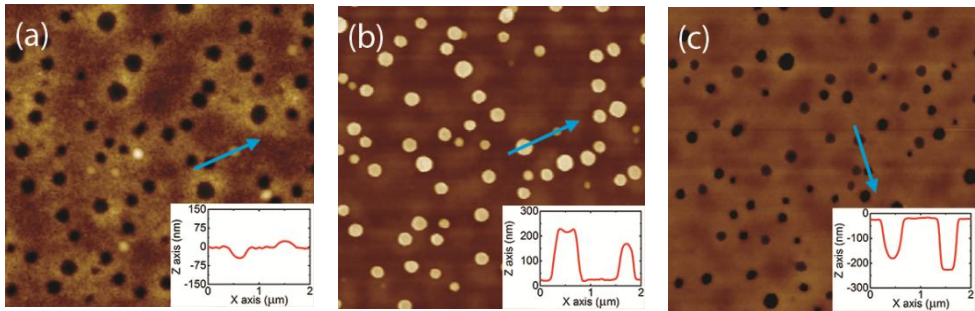
Figure 4.3: Selective dissolution method applied on a P(VDF-TrFE):F8BT (9:1 w/w) blend deposited on a Au substrate. AFM topography images (10×10 μm^2) of: (a) as processed blend. (b) the remaining structure of the blend after selectively dissolving the ferroelectric phase. (c) the remaining structure of the blend after selectively dissolving the semiconductor (F8BT) phase. Insets indicate line sections over the blend shown with blue arrows. The total vertical scale is 300 nm in all panels.

On basis of numerical simulations it was found that domains with a concave top yield enhanced switching compared those with convex or flat tops due to the closer proximity of the injection point to the ferroelectric polarization charges.[22] In the AFM topography images of the P(VDF-TrFE):F8BT blend in Figure 4.3, the first three domain types can all be identified. Figure 4.3 shows height scans of the as-processed blend film (see Figure 4.3a), taken after selective removal of the ferroelectric matrix (see Figure 4.3b), and upon selective removal of the F8BT material that is accessible from the top surface of the film. The exact procedure followed to selectively dissolve the phases is mentioned in the Experimental Section. The elegance of selective phase dissolution is that the resulting topology images provide complementary pieces of information that together allow reconstruction of the full 3D morphology of the phase separated blend film.

From Figure 4.3a (blend film), together with conductive force microscopy described in Chapter 3 and in Ref. 20 (see Figure 4.2), we deduce that the electrically active Type-1 domains are situated within the concave ('dark') circular areas, *i.e.* below the average height of the matrix phase. The circular convex ('light') shapes in Figure 4.3a correspond to Type-2 domains, which protrude from the film but do not contact the substrate. The concave top surface of Type-1 domains that is visible in the cross-sectional scan (see inset Figure 4.3a) seems confirmed by Figure 4.3b (matrix removed). In contrast, the lower features in Figure 4.3b are convex and assigned to be Type-3 domains, *i.e.* initially covered by the P(VDF-TrFE) and hence not visible in Figure 4.3a. It is important that the shape of the side part of the domains is affected by the convolution with the AFM tip and reflects the opening angle of the probe. However, the geometry of the tip together with extremely slow scanning speed allows easy detection of all types of the domains and cavities associated with them. We note that removal of the matrix phase leads to the removal of the Type-2 and Type-4 domains in Figure 4.3b and therefore does not allow their detection.

The occurrence of Type-1 and Type-2 domains is further supported by Figure 4.3c (F8BT removed). Of the circular holes resulting after selective dissolution only the deeper ones have a flat bottom surface, strongly indicating the hole to persist all the way down to the substrate and to have been occupied by a Type-1 F8BT domain. In contrast, holes with relatively small diameters do not extend towards the substrate (see inset Figure 4.3c), and would therefore have been occupied by a Type-2 domain. It is noted that the selective dissolution procedure does not allow for direct identification of Type-4 domains, as they would be undetectable in the pristine blend film, screened against selective dissolution, and removed unselectively upon matrix dissolution.

The images in Figure 4.3 show that most of the semiconducting material resides in the lower region of the blend film. This finding, together with the appearance of low contrast features in Figure 4.3b that we interpret as a 'partial wetting layer' of F8BT, indicates a favorable interaction between F8BT and gold.[23] The non-isotropic distribution of the semiconducting material along the *z*-axis suggests the aforementioned spinodal decomposition[24] to be surface-directed. It is thought that an initially lamellar morphology resulting from pronounced stratification breaks up into a droplet-like morphology during later stages. To what extent demixing is surface-directed depends on i) the difference in interaction strength of the individual blend components with the air- and substrate interfaces and ii) the ratio of the diffusive and evaporative time scales. Once break-up of the lamellae has occurred, interfacial forces would prevent the reformation of elongated fluid structures. For this reason it is not surprising that the Type-1 domains are both higher and wider than the Type-3 (or Type-2) domains.

Concave features in the Type-1 domains may be explained in terms of the difference in solvent compatibility of the polymeric blend components.[25] They originate in the final stages of drying of the blend, during which the more diluted phase collapses around, or in between structures representing the already vitrified concentrated phase. An alternative explanation for the concave nature of the Type-1 domains may be resumed wetting of the gold substrate by F8BT during annealing. The elevated temperature can potentially reintroduce some mobility to the blend components, possibly allowing for F8BT structures to slowly spread onto the gold substrate and locally extend under the P(VDF-TrFE) matrix. This might also explain the fact that the matrix is consistently elevated at the edge of the Type-1 domains.

It is important to point out that the presence of the Type-1 domains is crucial for the device performance. In contrast, the electrically non-addressable Type-2, Type-3, Type-4 domains and the wetting layer represent a significant waste of the semiconductor material in the blend.

The presence of the Type-1 and Type-2 domains was independently confirmed by a combination of scanning probe microscopy techniques, including conductive-AFM, on the same blend.[20] In Ref. 20 and in Figure 4.2 it is shown that only Type-1 domains are responsible for the current in the device whereas Type-2 domains carry no measurable current.

4.2.2 Statistical analysis of the blend morphology

Having identified and confirmed the existence of various types of domains, we proceed with a quantitative assessment of the amount of material in each of the different phases. For the memory diode this is an important measure for the effective active area of the device and for the potential for improvement (by avoiding non-Type-1 domains). In order to estimate the volume fraction of electrically functional F8BT material in the blend films (*i.e.* represented by the Type-1 domains), we subjected the AFM topography data corresponding to Figures 4.3b and 4.3c to statistical analysis in terms of domain diameter and height. A statistically relevant sample size was obtained by considering a field of view of 20×20 μm^2, rather than 10×10 μm^2 (see Figure 4.4). Statistical data was obtained by quantitative analysis of the digital AFM images using commercial image processing software – Image-Pro Premier. Figures 4.5 and 4.6 show the resulting distribution functions – probability density function (PDF) and cumulative distribution function (CDF) for domain height and diameter (or hole depth and diameter), as well as a graph wherein the height (depth) of individual domains (holes) has been plotted against diameter. It has to be noted that the domain height in Figure 4.5 as well the hole depth in Figure 4.6 correspond to the average values obtained from the AFM topography data. Both figures represent the same types of the domains mentioned above, and are in agreement with the film thickness.
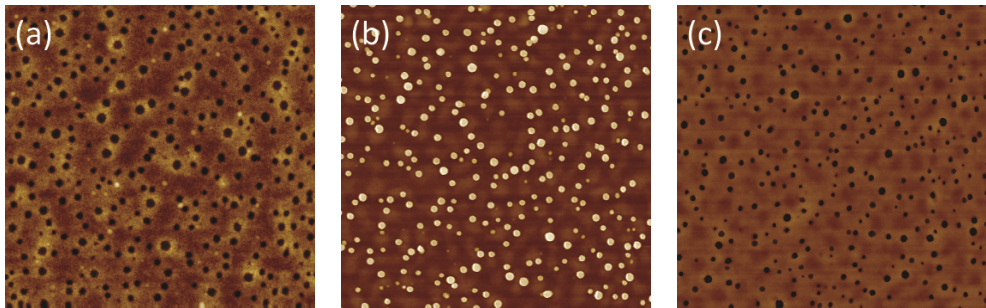
Figure 4.4: Selective chemical dissolution approach applied to a P(VDF-TrFE):F8BT (9:1 w/w) blend deposited on a Au substrate. AFM topography images (20×20 μm^2) of (a) as processed blend (total vertical scale 110 nm); (b) the remaining structure of the blend after selectively dissolving the ferroelectric (P(VDF-TrFE)) phase (total vertical scale 500 nm); (c) the remaining structure of the blend after selectively dissolving the semiconductor (F8BT) phase (total vertical scale 500 nm).

The bell-shaped distribution functions (see Figure 4.5a and Figure 4.5b) clearly demonstrate the presence of dominant length scales in the analyzed morphologies, which is indicative for spinodal demixing. Interestingly, the distribution functions are bimodal: two characteristic length scales (domain sizes) are observed. We recall that for 'classical' thermally quenched systems spinodal decomposition is characterized by only a single dominant length scale but numerical simulations exclusively based on diffusive dynamics
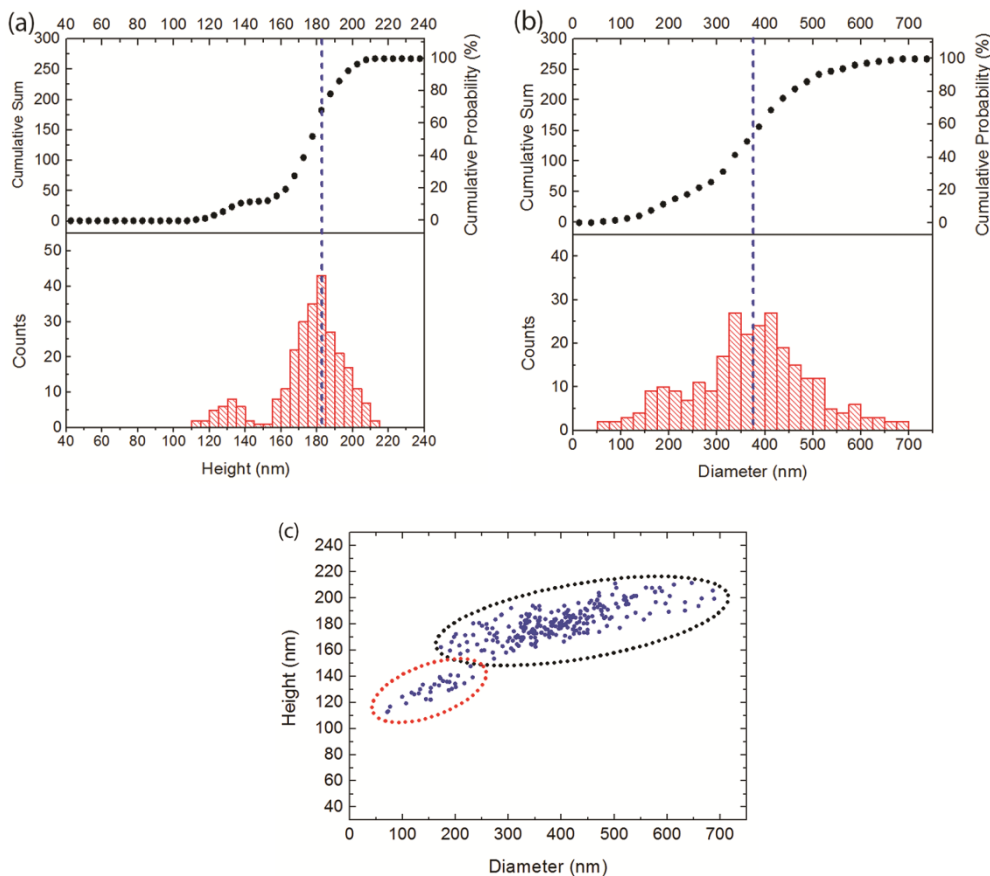
Figure 4.5: Statistical analysis of the AFM images (20 × 20 μm^2) (see Figure 4.4b) taken on selectively dissolved P(VDF-TrFE) phase of a P(VDF-TrFE):F8BT (9:1 w/w) blend on Au electrode shown in Figure 4.3b. (a). Domain height distribution (histogram, cumulative probability and cumulative sum). (b). Domain diameter distribution (histogram, cumulative probability and cumulative sum). (c). Plot of domain diameter *vs.* domain height. Black and red dashed ellipses represent two distinct clusters of points which correspond to the Type-1 and Type-3 domains respectively.

have recently shown the emergence of a second dominant length scale in spinodally demixed polymer/polymer/solvent and polymer/solvent systems to result from mass redistribution as a consequence of solvent evaporation.[26]

The positive tilt with respect to the horizontal axis of the ellipses marked in Figures 4.5c and 4.6c illustrate the remark made above that the highest domains are also expected to have the largest diameter, as interfacial forces limit the aspect ratio of structures in the demixed fluid.

An important finding in Figure 4.5c and Figure 4.6c is the fact that the data points form two distinct clusters. Detailed statistical analysis of the data and comparison with the AFM topography images suggests that the majority of each type of the domains (Type-1, Type-2 or Type-3, in Figure 4.1) reside in a particular cluster. This gives the possibility to estimate the total volume occupied by the specific type of the domains. For simplicity, for the volume calculation every domain was considered to be cylindrically-shaped with flat top and bottom parts.
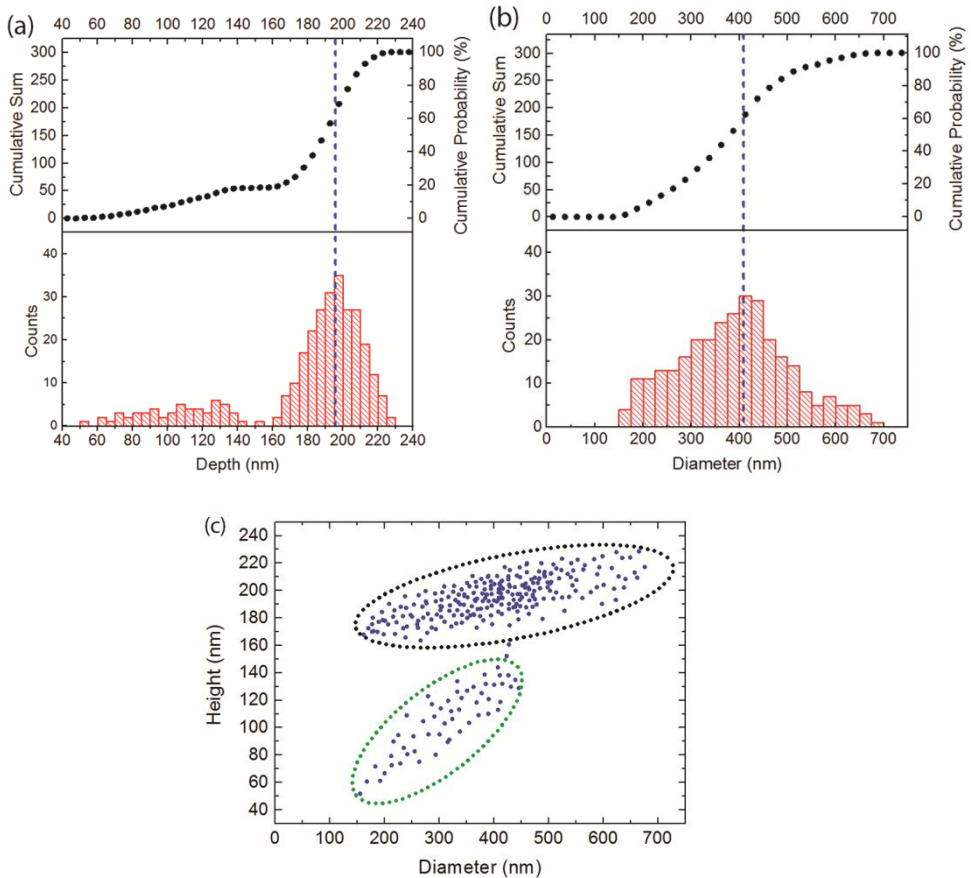
Figure 4.6: Statistical analysis of the AFM images (20 × 20 μm²) (see Figure 4.4c) taken on selectively dissolved F8BT phase of a P(VDF-TrFE):F8BT (9:1 w/w) blend on Au electrode shown in Figure 4.3c. (a). Hole depth distribution (histogram, cumulative probability and cumulative sum). (b). Hole diameter distribution (histogram, cumulative probability and cumulative sum). (c). Scatter plot of hole diameter *vs.* hole depth. Black and green dashed ellipses represent two distinct clusters of points which correspond to the Type-1 and Type-2 domains respectively.

The volume fraction of each type of the domains was calculated based on the initial volume of the semiconductor polymer in the initial solution and the average thickness of the blend. The Type-1, Type-2, Type-3 domains and the wetting layer yield around 67 ± 0.5 %, 2 ± 0.5 %, 8 ± 0.5 % and 23 ± 0.5 % of the total volume of the semiconductor respectively. The fact that these add up to ≈ 100 % excludes the existence of Type-4 domains. Thus, by combining topographical images with a full statistical analysis, the selective dissolution method provides detailed information about the 3D-structure of the blend at the local scale. It has to be noted that the reconstructed blend structure is in a good agreement with previously studied similar blend - P(VDF-TrFE):P3HT.[10,17] It has to be mentioned that the presence of the vertical, columnar-like – domains, *i.e.* Type-1-like, in that blend was also found by SEM, SNOM[19] and STXM[10] techniques.

We shall now briefly address the requirements that should be met by the phase separated blend to enable the application of the presented selective dissolution technique. First, the need for selective solvents does not imply the necessity of pure phase domains even though the presence of mixed phase domains will make it harder to find orthogonal solvents. Second, it is clear that the feature sizes in the present system are far from the ultimate limit for the technique. From an AFM perspective minimum feature sizes could in principle be in the nanometer range. However, tip convolution effects associated with typical tip radii around 10 nm and tip cone angles around 30° will put an upper limit to the aspect ratio of 'workable' features of around 2, *i.e.* 50 nm wide for a 100 nm high feature. High-aspect ratio tips can push this limit considerably further. From the morphology perspective the major concern is that the dissolution of one phase has to leave a 'representative' topography of the other phase. Hence, remaining features should also be morphologically stable, *i.e.* should not collapse. This excludes finely intermixed phases of soft materials, as *e.g.* found in many optimized organic photovoltaic bulk heterojunctions. Finally, the phase separation should lead to mostly bicontinuous phases, *i.e.* no, or only a small fraction of each phase should be completely surrounded by the other phase, *c.f.* domain Type-4 in Figure 4.1 that could be excluded for the present system but would be washed away by dissolving the surrounding P(VDF-TrFE).

4.3 Conclusions

In summary, we have introduced a selective dissolution approach for studying the 3D-morphology of phase-separated blends at the local scale. The method takes advantage of the selective solubility of different components of the blend. The two component blend of a semiconductor (F8BT) and a ferroelectric (P(VDF-TrFE)) polymer was investigated in this work. This system is a representative example of an active layer in ferroelectric diode. It was found that three distinct types of nearly pure semiconductor domains are present in the blend. A possible fourth type could be ruled out on basis of a statistical analysis. Thus, the selective dissolution approach is a simple and powerful technique that provides

information about the 3D-structure of phase separated blends at the local scale. The method is potentially applicable to a wider range of phase separated blends meeting criteria that are discussed above; roughly spoken, features should be predominantly vertical and have an aspect ratio below ~ 2, *i.e.* 50 nm wide for a height of 100 nm.

4.4 Experimental

Poly[(9,9–di–n–octylfluorenyl–2,7–diyl) – alt(benzo[2,1,3]thiadiazol-4,8-diyl)] F8BT (M_n = 4.9 kDa, D = 1.8) was synthesized according to a modified Suzuki polymerization.[27,28] The ferroelectric polymer, poly(vinylidene fluoride-trifluoroethylene) P(VDF-TrFE) (M_n = 220 kDa, $2.3 < D < 2.8$ with a 77/23 VDF/TrFe ratio) was supplied by Solvay Specialty Polymers. Blend solutions were prepared by co-dissolving P(VDF-TrFE) and F8BT (9:1 w/w) in a mixture of cyclohexanone and tetrahydrofurane 75:25 (v/v) at 50 °C overnight. Cleaned glass substrates with litho patterned gold were used. Blend films were then spin coated in a nitrogen-filled glove box. The average thickness of the film was measured with a DEKTAK profilometer and found to be ≈ 200 ± 10 nm. Subsequently, the samples were annealed at 135 °C for 1 hour.

For the dissolution technique dimethylsulfoxide (DMSO) and toluene were used to selectively dissolve the ferroelectric (P(VDF-TrFE)) and the semiconductor (F8BT) parts of the blend respectively.

Surface topography of the dried blend films was examined by atomic force microscopy (AFM, Veeco MultiMode NS-IIIA). Topography is measured using a sharp (apex radius < 10 nm) AFM tip in tapping-mode. The AFM measurements were performed using Al coated Si tips (Nanosensors, spring constant $k \approx$ 12.5 N/m). The C-AFM current was detected using a high sensitivity current amplifier (TUNA module, 10^{11} V/A, Veeco) together with Pt/Ir coated Si tips (Nanosensors, spring constant $k \approx$ 5 N/m).

Statistical analysis of the selective dissolution data was performed using commercial image analysis software Image-Pro Premier. Diameter and height of each domain, as well as of the (partial) wetting layer at the bottom surface, were identified by the software based on pixel intensity values.

4.5 References

[1]   C.J. Brabec, M. Heeney, I. McCulloch, J. Nelson, Influence of blend microstructure on bulk heterojunction organic photovoltaic performance, *Chem. Soc. Rev.* **2011**, *40*, 1185.

[2]   A.C. Morteani, A.S. Dhoot, J.S. Kim, C. Silva, N.C. Greenham, C. Murphy, E. Moons, S. Ciná, J.H. Burroughes, R.H. Friend, Barrier-free electron–hole capture in polymer blend heterojunction light-emitting diodes, *Adv. Mater.* **2003**, *15*, 1708.

[3]   A.C. Arias, F. Endicott, R.A. Street, Surface-induced self-encapsulation of polymer thin-film transistors, *Adv. Mater.* **2006**, *18*, 21, 2900.

[4]   K. Asadi, D.M. de Leeuw, B. de Boer, P.W.M. Blom, Organic non-volatile memories from ferroelectric phase-separated blends, *Nature Mater.* **2008**, *7*, 547.

[5]   K. Asadi, T.G. de Boer, P.W.M. Blom, D.M. de Leeuw, Tunable injection barrier in organic resistive switches based on phase-separated ferroelectric−semiconductor blends, *Adv. Funct. Mater.* **2009**, *19*, 3173.

[6]   J. Hu, J. Zhang, Z. Fu, J. Weng, W. Chen, S. Ding, Y. Jiang, G. Zhu, Fabrication of electrically bistable organic semiconducting/ferroelectric blend films by temperature controlled spin coating, *ACS Appl. Mater. Interfaces* **2015**, *7*, 6325.

[7]   M.A. Khan, U.S. Bhansali, D. Cha, H.N. Alshareef, All-polymer bistable resistive memory device based on nanoscale phase-separated PCBM-ferroelectric blends, *Adv. Funct. Mater.* **2013**, *23*, 2145.

[8]   T. Braz, Q. Ferreira, A.L. Mendonca, A.M. Ferraria, A.M.B. do Rego, J. Morgado, Morphology of ferroelectric/conjugated polymer phase-separated blends used in nonvolatile resistive memories. Direct evidence for a diffuse interface, *J. Phys. Chem. C* **2015**, *119*, 1391.

[9]   R.A.J. Janssen, J. Nelson, Factors limiting device efficiency in organic photovoltaics, *Adv. Mater.* **2013**, *25*, 1847.

[10]   C.R. McNeill, K. Asadi, B. Watts, P.W.M. Blom, D.M. de Leeuw, Structure of phase-separated ferroelectric/semiconducting polymer blends for organic non-volatile memories, *Small* **2010**, *6*, 4, 508.

[11]   A.J.J.M. van Breemen, T. Zaba, V. Khikhlovskyi, J. Michels, R. Janssen, M. Kemerink, G. Gelinck, Surface directed phase separation of semiconductor ferroelectric polymer blends and their use in non-volatile memories, *Adv. Funct. Mater.* **2015**, *25*, 278.

[12]   S.H. Sung, B.W. Boudouris, Systematic control of the nanostructure of semiconducting-ferroelectric polymer composites in thin film memory devices, *ACS Macro Lett.* **2015**, *4*, 293.

[13]   X. Yang, Semiconducting polymer composites: principles, morphologies, properties and applications, WILEY-VCH, **2012**, *7*, 191.

[14]   X. Yang, J. Loos, S. C. Veenstra, W.J.H. Verhees, M.M. Wienk, J.M. Kroon, M.A.J. Michels, R.A.J. Janssen, Nanoscale morphology of high-performance polymer solar cells, *Nano Lett.* **2005**, *5*, 4, 579.

[15]   S.S. van Bavel, E. Sourty, G. de With, J. Loos, Three-dimensional nanoscale organization of bulk heterojunction polymer solar cells, *Nano Lett.* **2009**, *9*, 2, 507.

[16]   A.J.J.M. van Breemen, J.-L. van der Steen, G. van Heck, R. Wang, V. Khikhlovskyi, M. Kemerink, G.H. Gelinck, Crossbar arrays of nonvolatile, rewritable polymer ferroelectric diode memories on plastic substrates, *Appl. Phys. Express* **2014**, *7*, 031602.

[17]   K. Asadi, H.J. Wondergem, R.S. Moghaddam, C.R. McNeill, N. Stingelin, B. Noheda, P. W. M. Blom, D. M. de Leeuw, Spinodal decomposition of blends of semiconducting and ferroelectric polymers, *Adv. Funct. Mater.* **2011**, *21*, 1887.

[18]   J.J. Michels, A.J.J.M. van Breemen, K. Usman, G.H. Gelinck, Liquid phase demixing in ferroelectric/semiconducting polymer blends: an experimental and theoretical study, *J. Polym. Sci. Part B: Polym. Phys.* **2011**, *49*, 1255.

[19]   M. Kemerink, K. Asadi, P.W.M. Blom, D.M. de Leeuw, The operational mechanism of ferroelectric-driven organic resistive switches, *Org. Electron.* **2012**, *13*, 147.

[20] V. Khikhlovskyi, R. Wang, A.J.J.M. van Breemen, G.H. Gelinck, R.A.J. Janssen, M. Kemerink, Nanoscale organic ferroelectric resistive switches, *J. Phys. Chem. C* **2014**, *118*, 3305.

[21] M. Li, N. Stingelin, J.J. Michels, M.-J. Spijkman, K. Asadi, R. Beerends, F. Biscarini, P.W.M. Blom, D.M. de Leeuw, Processing and low voltage switching of organic ferroelectric phase-separated bistable diodes, *Adv. Funct. Mater.* **2012**, *22*, 2750.

[22] R. Wang, V. Khikhlovskyi, M. Kemerink, *unpublished*.

[23] A. Budkowski, A. Bernasik, P. Cyganik, J. Rysz, R. Brenn, Surface-directed phase separation in nanometer polymer films: self-stratification and pattern replication, *e-Polymers* **2002**, *6*, 1.

[24] C.C. Lin, H.S. Jeon, N.P. Balsara, B. Hammouda, Spinodal decomposition in multicomponent polymer blends, *J. Chem. Phys.* **1995**, *103*, 5, 1957.

[25] S. Walheim, M. Bölltau, J. Mlynek, G. Krausch, U. Steiner, Structure formation via polymer demixing in spin-cast films, *Macromolecules* **1997**, *30*, 4995.

[26] C. Schaefer, P. van der Schoot, J.J. Michels, Structuring of polymer solutions upon solvent evaporation, *Phys. Rev. E* **2015**, *91*, 022602.

[27] T. van Woudenbergh, J. Wildeman, P.W.M. Blom, J.J.A.M. Bastiaansen, B.M.W. Langeveld-Voss, Electron-enhanced hole injection in blue polyfluorene-based polymer light-emitting diodes, *Adv. Funct. Mater.* **2004**, *14*, 677.

[28] N. Miyaura, A. Suzuki, Palladium-catalyzed cross-coupling reactions of organoboron compounds, *Chem. Rev.* **1995**, *96*, 2457.

Chapter 5

Surface directed phase separation of semiconductor ferroelectric polymer blends and their use in non-volatile memories

The polymer phase separation of P(VDF-TrFE):F8BT blends is studied in detail. Its morphology is a key to the operation and performance of the ferroelectric diodes. In this chapter, the possibility to direct the semiconducting domains of a phase-separating mixture of P(VDF-TrFE) and F8BT in a thin film into a highly ordered 2D lattice by means of surface directed phase separation is demonstrated. Numerical simulation of the surface-controlled de-mixing process provides insight in the ability of the substrate pattern to direct the phase separation, and hence the regularity of the domain pattern in the final dry blend layer. By optimizing the ratio of the blend components, the number of electrically active semiconductor domains is maximized. Pattern replication on a cm-scale is achieved, and improved functional device performance is demonstrated in the form of a tenfold increase of the ON-current and a sixfold increase in current modulation. This approach therefore provides a simple and scalable means to higher density integration, the ultimate target being a single semiconducting domain per memory cell.

5.1 Introduction

Solution-processed polymer semiconductors offer the possibility to mix together active components having markedly different electronic and/or optical properties in a common solvent.[1] Upon solvent extraction, the polymers typically demix and a thin film with a phase separated morphology is formed. Previously reported work in the field of photovoltaics,[2] light emitting diodes[3] and transistors[4] provides clear examples of the efficiency of this approach, as well as some of its limitations. Recently,[5] Asadi *et al.* used a phase separated blend of semiconducting and ferroelectric polymers to make non-volatile memories. In all these device types, the electronic characteristics depends critically on the final morphology, and better insights into the phase separation, mechanism, and control thereof will ultimately enhance our ability to engineer greater functionality into future organic electronics systems. Bulk demixing of binary polymer mixtures has been studied extensively during the last decades and is reasonably well understood.[6] Most previous studies focused on de-mixing phenomena in polymer melts. In organic electronics applications, however, thin films are prepared by a sudden extraction of a solvent. Due to their intrinsic immiscibility, polymer mixtures typically de-mix during solvent evaporation. The resulting phase separated morphology may be far from thermodynamic equilibrium, and relaxation toward equilibrium may be hindered by kinetic barriers formed by the nonequilibrium phase morphology. Furthermore, surface effects can play a role. Phase separation in bulk mixtures commonly leads to an isotropic, disordered morphology of the coexisting phases, whereas the influence of a surface may lead to preferential segregation of one of the components near the surface, for instance in the form of a wetting layer. In Asadi's new polymer non-volatile memory, described in detail in Chapter 1, the blend of semiconducting and ferroelectric polymers is sandwiched between two metal electrodes.[5] The ferroelectric polymer provides the binary state and data retention, whereas the semiconducting polymer domains provides the means to probe that state via an electrical current. More specifically, the polarization-induced field of the ferroelectric polymer modulates the injection barrier at the semiconductor-electrode interface leading to bistable current switching.[7] Numerical calculations indicate that the stray field of the polarized ferroelectric laterally permeates at most a few tens of nm into the semiconductor.[8] Hence, control over the semiconductor domain size is crucial. It was shown[9] that the solvent-processed phase separated blend is comprised of disk-shaped submicrometer sized domains of the semiconducting polymer (*i.e.*, poly(3-hexylthiophene) (P3HT)), dispersed in a matrix of the ferroelectric copolymer poly(vinylidene fluoride-trifluoroethylene) (P(VDF-TrFE)). A similar morphology was observed when P(VDF-TrFE) was mixed with other polymeric semiconductors such as poly(9,9'-dioctyl fluorene) (PFO)[10] and poly[(9,9-di-n-octylfluorenyl-2,7-diyl)-alt-(benzo[2,1,3]thiadiazol-4,8-diyl)] (F8BT)[11] as well as molecular semiconductors such as [6,6]-phenyl-C_{61}-butyric acid methyl ester (PCBM).[12] It has been shown that liquid phase de-mixing of the blend components occurs via surface-

directed spinodal decomposition during solution casting.[13] Surface tension differences determine to what extent one of the phases is preferred at an interface, and thus whether surface-directed stratification plays a (dominant) role in establishing the final phase geometry.[14–17] In all these previous studies the final blend morphology is characterized by a random distribution of semiconductor domains, both in domain size as well as location. However, size, shape, distribution, percolation, and orientation of the semiconducting domains have been shown to determine the ultimate performance of the device.[7,8] Precise control over the morphology of phase separated blends is therefore highly desirable in order to achieve improved functionality. Moreover, it will facilitate further miniaturization of these memory diodes to smaller feature size and/or higher integration density.

In this chapter we demonstrate that it is possible to direct the semiconducting domains of a phase-separating mixture of P(VDF-TrFE) and F8BT in a thin film into a highly ordered 2D lattice by means of surface directed phase separation. Numerical simulation of the surface-controlled de-mixing process provides insight in the ability of the substrate pattern to direct the phase separation, and hence the regularity of the domain pattern in the final dry blend layer. Pattern replication on a cm-scale is achieved, and improved functional device performance is demonstrated in the form of a tenfold increase of the ON-current and a sixfold increase in current modulation. This approach therefore provides a simple and scalable means to higher density integration, the ultimate target being a single semiconducting domain per memory cell.

5.2 Results and discussion

5.2.1 Blend layer processing on non-patterned substrates

Figure 5.1 shows schematically the cross-section of a phase separated blend of P(VDF-TrFE) and F8BT sandwiched between the two metallic electrodes. As bottom electrode are used: i) gold (Au) and ii) Au fully passivated with a monolayer of 11-mercapto-1-undecanol (OH-SAM, see Figure 5.3b). Blend films with $h \approx 250 \pm 10$ nm are spin-coated on bare Au or patterned OH-SAM–passivated Au electrodes and subsequently annealed at 135 °C for 1 hour to facilitate development of the ferroelectric β-phase of P(VDF-TrFE).[18] The diodes are finished by evaporating a 100 nm top barium/aluminum (Ba/Al) cathode through a shadow mask. Ba/Al cathode was chosen in order to fabricate the devices with asymmetric I-V characteristics.

Table 5.1 lists the measured total surface energies (γ) and their disperse (γ^d) and polar (γ^p) contributions, together with the calculated interfacial energies (γ_{L-i}) for all blend components and substrates under consideration. The method used for obtaining γ^d and γ^p is the one proposed by Owens *et al.*,[19,20] whereas the interfacial tensions are calculated according to the Fowkes procedure.[21] The preference of a given component for a certain substrate depends on the interfacial energy between the two: the lower the interfacial
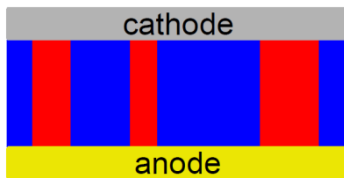
Figure 5.1: Schematic representation of a phase separated blend memory diode consisting of F8BT domains (red).

energy, the more the component is preferred at the given substrate. From this it can be inferred that P(VDF-TrFE) is preferred at Au and OH-SAM interfaces (see Table 1). Here, specific coordination between substrate and substance (*e.g.*, gold and sulfur) is neglected.

Table 5.1: Surface- and interfacial energies of the individual components of a blend consisting of solvent (cyclohexanone), P(VDF-TrFE), and F8BT, processed on a gold substrate, either or not covered with an OH-terminated SAM.

	Au	OH-SAM	solvent	P(VDF-TrFE)	F8BT
γ (mN/m)	53.3	75.1	34.0	29.3	32.8
γ^d (mN/m)	44.7	44.4	31.4	24.4	32.6
γ^p (mN/m)	8.6	30.7	2.6	4.9	0.2
$\gamma_{i\text{-Au}}$ (mN/m)	0	–	2.9	3.6	7.1
$\gamma_{i\text{-OH SAM}}$ (mN/m)	–	0	16.5	14.1	26.8

Figure 5.2 (top row) shows the surface morphology of films spin-coated on bare Au (see Figure 5.2b,d), and on OH-SAM monolayer-covered Au substrates (see Figure 5.2c,e), as measured using AFM. We used two different weight ratio's, *i.e.*, a 9:1 and 4:1 (w/w) P(VDF-TrFE):F8BT blend ratio respectively. In all cases, disk-like entities of the minor component (*i.e.*, F8BT) embedded in a matrix of the major component (*i.e.*, P(VDF-TrFE)) are observed, similar to the morphology previously observed for blends of P(VDF-TrFE):P3HT[9] and P(VDF-TrFE):PFO.[10,13] Changing the surface of the underlying gold substrate, by means of OH-SAM, has a strong influence on the phase separation. The OH-SAM-treated substrate shows smaller F8BT disks. The 9:1 blend film processed on bare Au (see Figure 5.2b top row) reveals two types of semiconductor domains. 40 % (10 per 100 μm^2) of the F8BT domains have a concave top surface (F8BT curves inward) and an average diameter of 500 nm, whereas 60 % has a convex top surface, that is, F8BT is protuberant. The convex domains typically have a larger average diameter of 800 nm. On OH-SAM passivated Au (see Figure 5.2c top row) the 9:1 blend film shows a large increase in number

density of both the concave and convex domain types to 40 and 70 per 100 μm^2, respectively. The average domain size of the concave domains remains more or less constant, whereas that of the convex domains is reduced to 600 nm. Increasing the relative amount of F8BT by going to a 4:1 blend ratio results in almost exclusively convex, F8BT domains with large diameter ($\langle d \rangle \approx 2$ μm) on bare Au (see Figure 5.2 d). OH-SAM passivation again leads to a suppression of the average size of the convex domains ($\langle d \rangle \approx$ 1.2 μm), at a significantly increased number density of 45 per 100 μm^2.
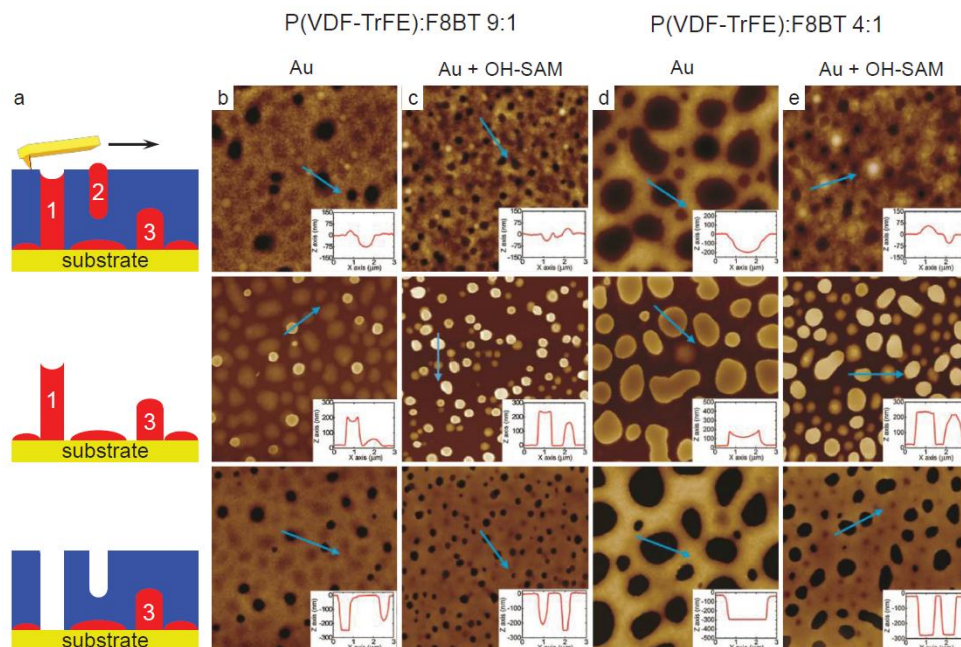
Figure 5.2: (a) Schematic representation of the films studied. Top row: as processed blend. Middle row: the ferroelectric was selectively removed. Bottom row: semiconductor was selectively removed. See text for more experimental details on the procedure to selectively remove a single polymer component from the blend. (b) AFM images (10 × 10 μm^2) of 9:1 w/w blend deposited on an Au substrate. (c) 9:1 w/w blend deposited on an Au substrate covered with OH-SAM. (d) 4:1 w/w blend deposited on Au electrode. (e) 4:1 w/w blend deposited on an Au substrate covered with OH-SAM. Insets indicate line sections over the blend shown with blue arrows.

To gain further information on the morphology throughout the blend film, we selectively removed one of the polymers from the blend films. Dimethyl sulfoxide (DMSO) was found to selectively dissolve P(VDF-TrFE), whereas toluene could be used to dissolve F8BT. Figure 5.2 shows AFM topography images obtained after the films have been treated

with DMSO (middle row) and toluene (bottom row), respectively. The images in the middle row reveal pillar-, as well as drop-like F8BT domains. These are labelled as '1' and '3' in Figure 5.2a. The images in the bottom row show assemblies of depressions of different depths in the P(VDF-TrFE) matrix. Putting these images together, we can distinguish three types of F8BT domains: 'bridging' (Type-1), 'floating' (Type-2), and 'buried' (Type-3) domains. This is illustrated in Figure 5.2a. Line scans consistently reveal the top surface of the Type-1 domains to be convex, whereas a concave top surface is encountered for the Type-2 and Type-3 domains. Line scans across the depressions originally occupied by Type-1 and Type-2 domains reveal the flat bottom surface of the substrate. Finally, we see evidence of a very thin (40 nm or less) F8BT wetting layer in the 9:1 blend processed on bare Au. This wetting layer is absent in the OH-SAM treated substrate. We therefore attribute the formation of the wetting layer to a specific coordinative interaction between the sulfur atoms of the F8BT and Au, a phenomenon also observed for a similar sulfur-containing polymeric semiconductor on Au.[15]

Only the Type-1 F8BT domains are electrically active,[8] as they bridge both electrodes in a memory device. Quantitative analysis reveals that the number density of Type-1 domains increases from 15 to 65 per 100 μm^2 upon OH-SAM passivation. Increasing the relative amount of F8BT by going from a 9:1 to a 4:1 blend ratio, results in large ($\langle d \rangle \approx 2$ μm) F8BT droplets on bare Au (see Figure 5.2d), as sufficient semiconductor is now provided for the wetting layer to absorb all material. Although in this situation virtually all domains are 'bridging', and therefore electrically active, such large domains are to be avoided. Numerical calculations and conductive AFM experiments[8] have shown that the stray field of the polarized ferroelectric laterally permeates at most a few tens of nm into the semiconductor. Hence, the current predominantly flows through the perimeter of the semiconducting domains[8] and it is preferred to have more domains with a smaller diameter.

Table 5.2: Number density and average diameter of Type-1 F8BT domains *vs.* electrode and blend ratio, as estimated from AFM images (see Figure 5.2 and Figure 5.3). Mean value of I_{ON} and I_{ON}/I_{OFF} ratio measured at a bias of + 6 V of 25 diodes fabricated with a P(VDF-TrFE):F8BT 9:1 or 4:1 w/w blend using either a patterned or non-patterned Au bottom electrode.

bottom electrode	blend ratio (w/w)	# type-1 (per 100 μm^2)	$\langle d \rangle$ [nm]	I_{ON} [μA]	I_{ON}/I_{OFF}
bare Au	9:1	15	800 ± 150	0.60 ± 0.04	1500 ± 90
bare Au	4:1	27	2000 ± 350	0.69 ± 0.04	1800 ± 100
OH-SAM	9:1	65	600 ± 100	–	–
OH-SAM	4:1	45	1200 ± 200	–	–
μCP OH-SAM	9:1	14	500 ± 50	0.63 ± 0.08	1700 ± 250
μCP OH-SAM	4:1	100	600 ± 75	6.02 ± 0.34	8900 ± 380

Au passivation with OH-SAM leads to suppression of the average size of the Type-1 domains ($\langle d \rangle \approx 1.2$ μm), at a number density of 45 per 100 μm^2. Nevertheless, some material remains inactive due to the occurrence of Type-3 features. As for device performance the number and diameter of the Type-1 F8BT domains are most relevant, we list these parameters for the different films studied in Table 5.2.

5.2.2 Blend layer processing on substrates with patterned SAMs

It has previously been shown that the domains of a phase-separating mixture of polymers in a thin film can be guided into periodic structures by a surface with a pre-patterned variation of surface energies.[22,23] This pioneering work focused on the methodology of this approach rather than incorporating these patterned layers in electronic devices. Morphology control by surface directed phase separation was explored in organic light emitting diodes,[24–26] photovoltaics[27] and thin film transistors.[28,29] Next, we show that this bottom-up approach also works for ferroelectric-semiconductor blends.
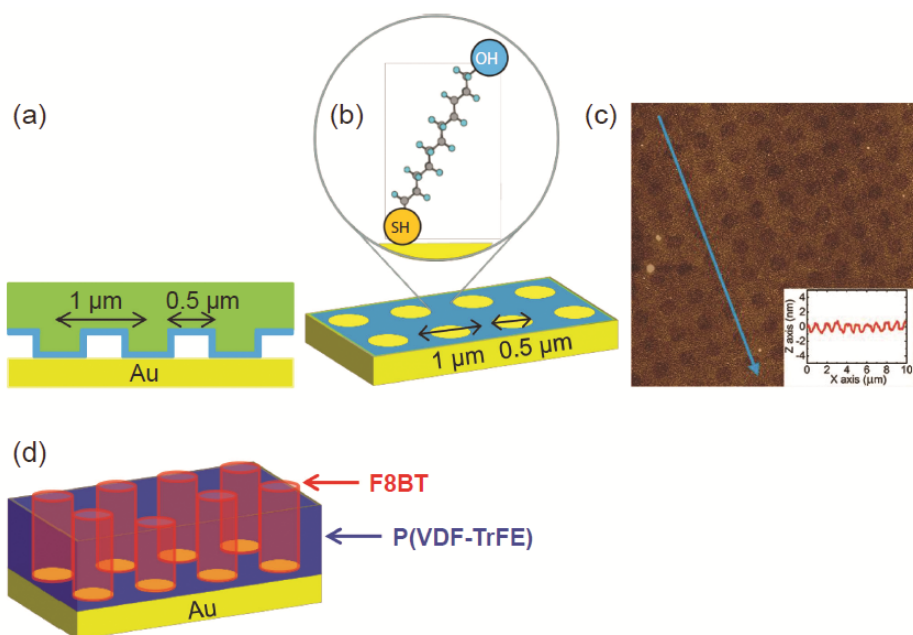
Figure 5.3: (a) Schematic representation of the μCP process using a PDMS stamp featuring a rectangular array of circular posts with a diameter of 0.5 μm and a pitch of 1 μm. b) Schematic representation of geometrically controlled OH-SAM passivation of the Au substrate. c) AFM image (10×10 μm^2) of Au substrate micro-contact printed with OH-SAM. Inset: line scan of the patterned substrate taken at the position indicated by the blue arrow. (d) Geometrically controlled phase separation induced by local OH-SAM passivation of the Au substrate. The strong F8BT-Au interaction is utilized to allow for selective adsorption of the semiconductor onto the Au electrode.

As mentioned above, F8BT has a coordinative interaction towards Au, which can be nullified by monolayer passivation of the gold surface. In addition, the calculated interfacial energies between SAM-passivated gold and the individual blend components (see Table 5.1), reveal that P(VDF-TrFE) is preferred at an OH-SAM-passivated Au substrate. These findings can be used to gain better control over the morphology of solution processed P(VDF-TrFE):F8BT blends. The strong F8BT-Au interaction is utilized to allow for adsorption of the semiconductor onto designated areas by geometrically controlled OH-SAM-passivation of the gold substrate prior to casting the P(VDF-TrFE):F8BT blend solutions (see Figure 5.3). Type-1 F8BT domains are therefore only in physical contact with bare gold, and possible effects of the OH-SAM changing the workfunction of the gold electrodes are therefore not relevant in this study.

The OH-SAM is deposited locally using micro-contact printing (μCP).[30,31] Figure 5.3a shows a schematic representation of the patterning process of the Au electrode, together with the dimensions of the features of the PDMS stamp. Figure 5.3b represents a schematic side view of a μCP Au electrode. OH-SAM is deposited everywhere except for small circular areas. These circular areas have a nominal diameter of 500 nm and are periodically placed on a rectangular grid with a periodicity of 1 μm. The molecular structure of the OH-SAM is also shown. Figure 5.3c shows the AFM topography image of the patterned Au electrode. The dark circular features in Figure 5.3c correspond to the bare Au areas, whereas the interstitial area is coated with OH-SAM. The average diameter of the circular features, as well as the center-to-center distance agree well with the expected values based on the stamp. Spreading of the OH-SAM ink is limited. The OH-SAM thickness as determined by AFM is ≈ 2 nm, which is in good agreement with literature values.[32] These results clearly demonstrate that this OH-SAM can be transferred to Au with excellent pattern replication using μCP.

Figure 5.4 shows AFM topography images of the P(VDF-TrFE):F8BT (9:1 w/w) and (4:1 w/w) blends spincoated on the Au substrates patterned with OH-SAM, together with images obtained after selective removal of one of the polymers from the blend films. Well-ordered 2D arrays of F8BT domains are observed that nicely replicate the μCP pattern. In fact, pattern replication was achieved over complete cm^2-area samples, that is, much larger length scales than shown in the AFM images in Figure 5.4. Pattern fidelity is particularly good for the 9:1 w/w blend. However, from the low average height (≈ 100 – 150 nm) of the F8BT domains compared to the blend film thickness of 250 nm, we conclude that about 80 % of the F8BT domains of the patterned 9:1 blend are of non-bridging Type-3. This assessment is confirmed in the images with the F8BT selectively removed (bottom row) where only a small number of pits goes all the way down to the substrate.

Numerical modeling of the phase separation process (see below) predicts that the number of Type-1 F8BT domains can increase by increasing the relative amount of F8BT. This is indeed experimentally confirmed by the AFM topography images of the 4:1 (w/w)

blend (see Figure 5.4b). Almost all F8BT domains have a height that closely matches the thickness of the as-processed blend film, implying that they are of Type-1. Furthermore, the average lateral domain size of 0.5 μm at the bottom of the film (lower panel in Figure 5.4b) is close to the μCP pattern. These results demonstrate that local deposition of OH-SAM by μCP patterning prior to blend deposition is a simple and powerful technique to influence the morphology and increase the number of electrically active Type-1 domains.

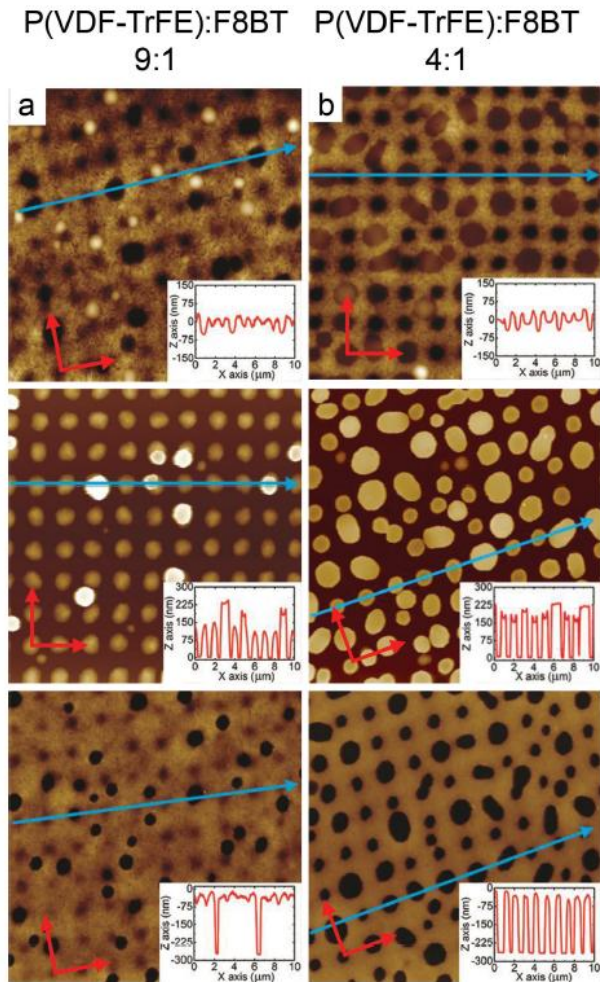**Figure 5.4:** (a) AFM images (10×10 μm^2) of P(VDF-TrFE):F8BT (9:1 w/w) blend coated on OH-SAM patterned Au electrode. Top panel: as processed blend. Middle panel: selectively removed P(VDF-TrFE). Bottom panel: selectively removed F8BT. Insets indicate line sections over the blend shown with blue arrows. (b) Idem for P(VDF-TrFE):F8BT (4:1 w/w) blend.

5.2.3 Simulations

Time-resolved numerical modeling of the phase separation process can provide highly valuable information on the origin of specific features of the phase morphology of semiconductor/P(VDF-TrFE) mixtures. Fluid phase spinodal decomposition of the solvent/P(VDF-TrFE)/F8BT ternary under evaporative conditions is modeled by a Cahn-Hilliard-Cook-deGennes type square gradient approximation. We refer to the Experimental section for more details regarding the modeling approach. Representation and discussion of the complete evolution of the microstructure is outside the scope of this chapter. Here we resort to discussing one (and the same) single time simulation snapshot for both blend P(VDF-TrFE)/F8BT ratios on patterned and nonpatterned monolayers. The snapshot represents a transient stage in the coarsening regime which allows the study of critical features preserved in the dried film.

Figure 5.5 shows simulation results by representing top view, as well as 3D tilted view images of the phase separated solvent/P(VDF-TrFE):F8BT morphology. The simulation results for a 9:1 blend ratio reproduce well the regular spacing of the F8BT domains on the areas without OH-SAM (see Figure 5.4a). The contact line diameter is more or less equal to the diameter of the dot itself. This seemingly trivial observation suggests that the spinodal wavelength (which is an intrinsic feature of the blend at a given composition) is at least of the same order as the dot spacing of the substrate pattern and that gradient energy contributions are high enough to prevent break-up of transient F8BT-rich domains into smaller droplets residing on the same dot. In line with the observed morphology, the numerical model also reproduces that pattern replication of the 9:1 blend is slightly better than that of the 4:1 blend ratio. Experiments and simulations (see Figure 5.4b and Figure 5.5d) also agree on the somewhat more pronounced lateral scrambling of the substrate pattern in case of the 4:1 blend, as compared to the 9:1 blend. In contrast, scrambling of the pattern in the vertical direction is more strongly observed for the 9:1 blend (see Figure 5.4a and Figure 5.5c). The latter observation explains the relatively abundant occurrence of both Type-2 and Type-3 F8BT domains in the 9:1 blend layers, at the expense of the desired Type-1 features. Relating to this, the 3D images in Figure 5.5d clearly show that the features observed at the substrate interface and at the top of the wet film in most cases belong to the same F8BT-rich domains, suggesting a 4:1 blend ratio to eventually yield a larger number of Type-1 domains as compared to patterned films produced from a 9:1 blend. The latter observation is verified by the AFM analysis given in Figure 5.4.

Interestingly, the simulations suggest that especially in case of the 9:1 blend F8BT-rich domains can exist that are not in direct contact with either surface (see Figure 5.5a,c). These domains originate from rupture of preceding stratified phase morphology, induced by surface tension differences between the blend components and/or differences in the time scales of diffusion and evaporation.[33] Merging of these encapsulated F8BT droplets with Type-2, or Type-3 domains during later stages of drying is expected to

partially account for the occurrence of Type-1 F8BT domains. They thus form a very important intermediate state. Direct experimental evidence for the occurrence of these domains in the actual films is difficult to obtain. Because these domains are fully encapsulated by the P(VDF-TrFE)-rich matrix, they do not appear in the AFM measurements of the full blend layer, and they are prone to lift off the substrates upon selective dissolution of the P(VDF-TrFE) matrix.
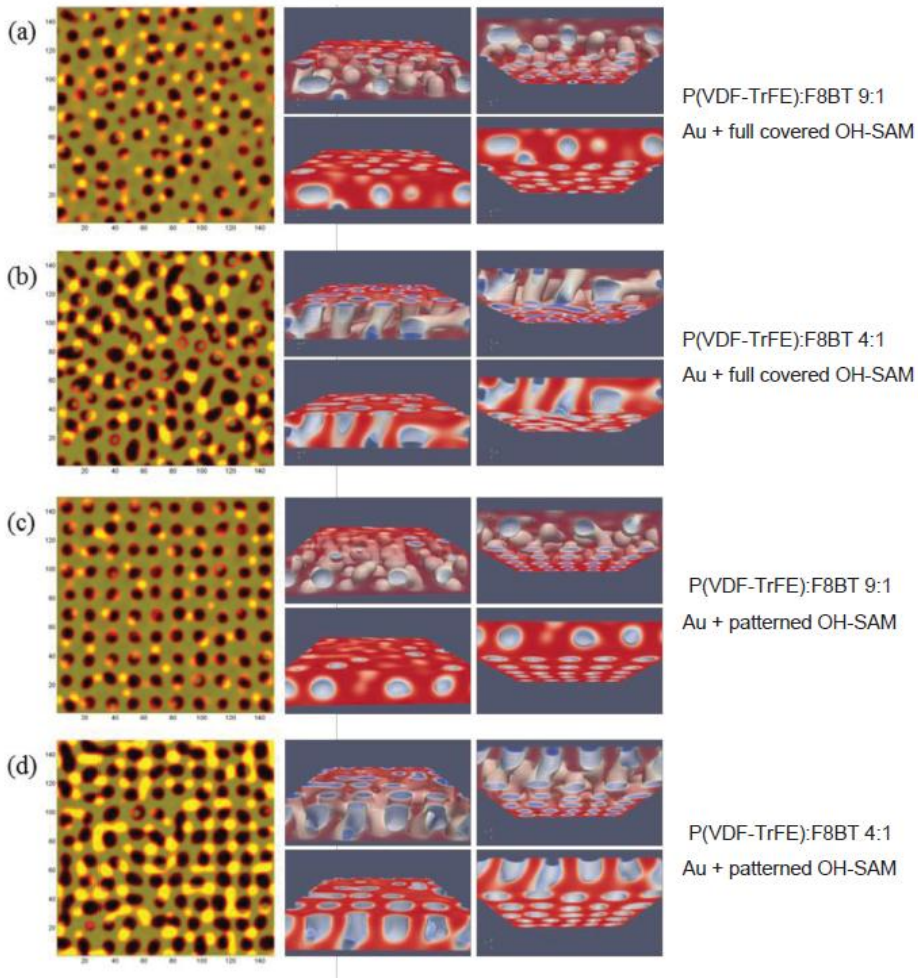
Figure 5.5: Numerical simulation of spinodal decomposition of the P(VDF-TrFE):F8BT blend solution during solvent evaporation on Au electrodes that are (a, b) fully and (c, d) partially covered with OH-SAM for 9:1 (a, c) and 4:1 (b, d) blend ratios; left panels: overlay of the lateral concentration fields of P(VDF-TrFE) and F8BT at the substrate (dark: F8BT-rich) and air (bright: F8BT-rich) interfaces; right panels: tilted 3D top and bottom view images of the phase separated blend layers: P(VDF-TrFE)-rich (red), F8BT-rich (grey); the same image is shown with a transparent (top) and solid (bottom) matrix phase.

5.2.4. Electrical characterization of polymer blend films in ferroelectric diodes

Memory diodes were made by spincoating a continuous P(VDF-TrFE):F8BT film on top of i) gold, ii) gold coated with OH-SAM, and iii) gold coated with patterned OH-SAM. Ba/Al is used as top electrode in all cases. For unclear reasons all (25) memory diodes made on gold fully covered with OH-SAM were shorted. The typical characteristics of the memory diodes with bare gold and gold coated with patterned OH-SAM are shown in Figure 5.6. Ferroelectric polarization reversal occurs at $\approx |10|$ V, *i.e.*, close to the coercive electric field of 50 MV/m measured for P(VDF-TrFE) capacitors.[34] The polarization is stable at lower electric fields. Because the perpendicular device current depends on the direction of the polarization state, this state can be read out repeatedly (non-disturb) at lower voltages. This forms the basis for these devices as non-volatile, reprogrammable memories.
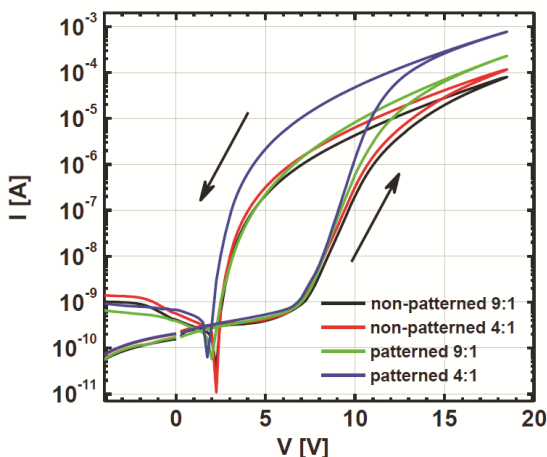
Figure 5.6: Current *vs.* voltage (*I-V*) hysteretic sweeps of ferroelectric diodes fabricated with a P(VDF-TrFE):F8BT 9:1 or 4:1 w/w blend using either a patterned or non-patterned Au anode. In all cases Ba/Al is used as cathode. The diode is swept between + 18.5 and − 18.5 V. Arrows indicate the scan direction.

As can be seen in Figure 5.6, the average ON-current of the diode with 9:1 w/w blend and Au electrode (no patterned OH-SAM) is 0.60 ± 0.04 µA at a gate bias of + 6 V. The average OFF-current (I_{OFF}) is 0.55 ± 0.01 nA. The current modulation I_{ON}/I_{OFF}, therefore, amounts to 1500. This value is already relatively high, and allows integration of these diodes in 1 kilobit memory arrays.[11] I_{OFF} is likely dominated by the leakage currents caused by nonintrinsic effects like slow depolarization and ionic movement, and seems to be independent of both the P(VDF-TrFE):F8BT ratio and regularity of the semiconducting domain pattern. Relative to the 9:1 blend diodes with Au electrodes, 9:1 w/w diodes with

patterned OH-SAM as well as 4:1 w/w diodes with no OH-SAM have a similar value for I_{ON}, and therefore similar I_{ON}/I_{OFF} modulation. The I_{ON} of the 4:1 w/w diode with patterned OH-SAM increases nearly one order of magnitude. Table 5.2 shows the mean value of I_{ON} and the ON- to OFF- current ratio (I_{ON}/I_{OFF}) measured at a bias of + 6 V over 25 memory diodes of each type. These results can be correlated to the number density and average size of electrically active Type-1 F8BT domains. Except for the 4:1 w/w diode with patterned OH-SAM, the Type-1 F8BT domains have a low density (14 – 27 per 100 μm^2). Furthermore, the semiconductor domain diameter of 4:1 w/w diodes with no OH-SAM of 2000 nm is undesirably large. Therefore, a similar I_{ON} is expected in a zero-order approximation for these diodes. The Type-1 F8BT domain number density in case of the 4:1 w/w diode with patterned OH-SAM reaches an almost maximum number density per 100 μm^2. This high density is combined with an average lateral domain size of $\approx$ 600 nm because demixing is largely directed by the applied μCP SAM pattern. As a result, a close to tenfold increase of the ON-current and a sixfold larger current modulation was found in memory diodes with geometrically controlled phase separation.
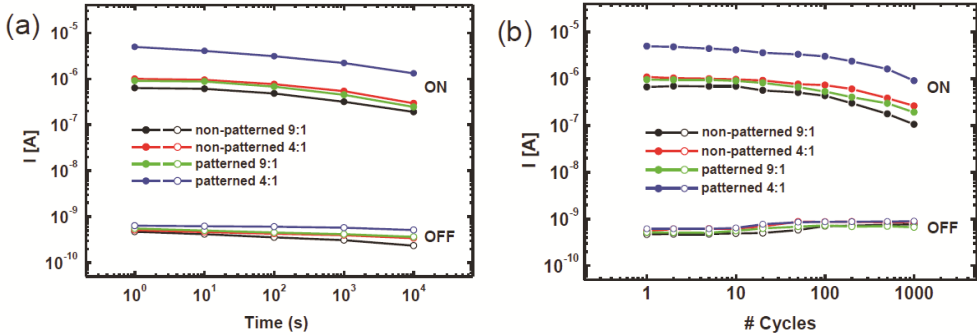
Figure 5.7: (a) Data retention: Evolution of current in the ON- state and OFF- state as a function of time after programming at a bias of + 6 V. (b) Endurance data: Reversible ON- and OFF- switching – for 1000 consecutive program-erase cycles, readout at + 6 V.

Data retention was examined by programming the device once to the ON- or OFF-state by applying a + 18.5 and – 18.5 V pulse respectively, and then monitoring the current over time at + 6 V (see Figure 5.7a). All memory devices show excellent retention. Both I_{ON} and I_{OFF} do not change more than a factor of 3, effectively resulting in a I_{ON}/I_{OFF} ratio of three orders of magnitude after 10 000 s. We see no significant differences in current over time for the different memories. Because of its higher initial ON-current the 4:1 patterned devices proved to have the highest I_{ON}/I_{OFF} ratio of 1800 after 10 000 s.

In Figure 5.7b the low conductance OFF-state and high conductance ON-state are measured, while the memory device is repeatedly switching between ON- and OFF- state by applying program and erase pulses of ± 18.5 V. All memory diodes show reversible

switching over many cycles. After 1000 cycles an I_{ON}/I_{OFF} ratio of over 10^3 is obtained for the 4:1 w/w diode with patterned OH-SAM.

5.3 Conclusions

In summary, we have studied in detail the polymer phase separation of P(VDF-TrFE):F8BT blends. Its morphology is the key to the operation and performance of memory diodes. Selective dissolution of the individual blend components in combination with AFM analysis showed that only a limited fraction of the semiconductor domains are electrically active. In addition, a semi-continuous, thin (< 40 nm) wetting layer of F8BT was found in case of a reference gold electrode. The specific coordinative interaction between F8BT and gold has been utilized to allow for adsorption of the semiconductor onto designated areas by geometrically controlled monolayer passivation of the gold substrate prior to casting of the P(VDF-TrFE):F8BT blend solutions. Tuning of the P(VDF-TrFE):F8BT blend ratio resulted in a further optimization of the morphology by maximizing the number of electrically active semiconducting domains. Thus, size, position and number density of these domains closely replicated the underlying chemical pattern induced by microcontact printing.

Full 3D numerical simulation of the surface-controlled demixing process has provided insight in the ability of the substrate pattern to direct the phase separation, and hence the regularity of the domain pattern in the final dry blend layers.

The electrical performance of memory diodes could be significantly improved by blend patterning and composition optimization. A close to tenfold increase of the ON-current and sixfold larger current modulation was found for memory diodes in which the number density of electrically active domains was maximized by morphology control. Hence, the general concept shown here provides a basis to satisfy the demand of improved functionality and further miniaturization of these memory diodes to smaller feature size and/or higher integration density.

5.4 Experimental

Poly[(9,9-di-n-octylfluorenyl-2,7-diyl) $-$ alt $-$ (benzo[2,1,3]thiadiazol-4,8-diyl)] F8BT (M_n = 4.9 kDa, D = 1.8) was synthesized according to a modified Suzuki-polymerization.[35,36] The ferroelectric polymer, poly(vinylidene fluoride-trifluoroethylene) P(VDF-TrFE) (M_n = 220 kDa, 2.3 < D < 2.8 with a 77/23 VDF/TrFe ratio) was supplied by Solvay Specialty Polymers. Blend solutions were prepared by co-dissolving P(VDF-TrFE) and F8BT (9:1 or 4:1 weight ratio) in a mixture of cyclohexanone and tetrahydrofurane 75:25 (v/v) at 50 °C overnight. Cleaned glass substrates with litho patterned gold were used. Blend films were then spin-coated in a nitrogen-filled glove box. The thickness of the film was measured with a DEKTAK profilometer and varied between 200 – 230 nm.

Subsequently, the samples were annealed at 135 °C for 5 min. Finally, the Ba/Al cathode is evaporated through a shadow mask, followed by thin film encapsulation. Surface topography of the dried blend films was examined by atomic force microscopy. Topography is measured using a sharp (apex radius < 10 nm) AFM tip in tapping-mode (TM). The AFM measurements were performed using Al coated Si tips (Nanosensors, spring constant $k \approx 12.5$ N/m).

Contact angle measurements were performed at room temperature (22 °C) on an Easydrop Standard (Krüss) goniometer using a drop size of 2 µL. Surface-directed phase separation of semiconductor ferroelectric polymer blend films using the microcontact printing technique was performed on patterned UV-ozone cleaned gold electrodes. A h-poly(dimethylsiloxane) PDMS stamp, featuring a 2D pillar grid of 475 – 565 nm wide dots with 1000 nm ± 3% pitch, was used. Stamps were inked by immersing them in 11-mercapto-1-undecanol solution (1 mM in ethanol) for about 10 min. After removal from the ink solutions, all stamps were rinsed with ethanol and dried in a stream of nitrogen for about 30 s. Stamping was performed manually for 20 s by using tweezers for stamp handling and by taking advantage of the natural stamp-substrate adhesion. No extra pressure was applied. A blend of P(VDF-TrFE):F8BT (9:1 or 4:1 weight ratio) in a mixture of cyclohexanone and tetrahydrofurane 75:25 (v/v) was then spin-coated in a nitrogen-filled glove box onto this patterned surface at 2500 rpm for 60 s and subsequently annealed for 5 min at 135 °C.

Fluid phase spinodal de-mixing of the solvent/P(VDF-TrFE)/F8BT blend under evaporative conditions is modeled by a Cahn-Hilliard-Cook-deGennes type square gradient approximation,[37–39] involving a ternary Flory-Huggins local mixing free energy.[40,41] The usual bulk free energy functional comprising local and non-local contributions is augmented with terms describing the interaction between the blend components and the substrate- and air interfaces as effective interaction parameters[42] adopting non-zero values only at, respectively, $z = 0$ and $z = h$. Solvent evaporation is treated according to a previously published procedure,[43] which at each time step calculates an instantaneous global evaporation rate based on a (relative) mass transfer coefficient and the mean volume fraction of solvent in the top of the fluid layer. The mass loss due to evaporation is then compensated for by downscaling the grid spacing in the z-dimension.[44] The model does not take the final stages of drying into account. The input parameters for the simulations are summarized by the tables shown in the supplementary info. Table 5.3 lists the Flory-Huggins parameters (*i.e.*, effective degree of polymerization N_i and mutual interaction parameter χ_{ij}), whereas Table 5.4 gives the air and substrate interaction parameters. The effective degrees of polymerization are obtained by scaling the average molar volume of the polymers to that of the solvent (cyclohexanone). Solvent-polymer interaction parameters χ_{1j} are chosen to comply with the constraint of compatibility with both polymers ($\chi_{1j} < 0.5$), whereby it is assumed that P(VDF-TrFE) is somewhat better soluble than F8BT ($\chi_{13} < \chi_{12}$). Polymer-polymer interaction parameter χ_{23} is taken sufficiently high so as to avoid the formation of mixed binodal phases, that is, in agreement with experimental

findings.[13] Surface interaction parameters χ_i^a and χ_i^s are quantified via the method explained in another study[42] involving the measured disperse (γ^d) and polar (γ^p) surface energy contributions of the blend components and the substrate (see Table 5.1). As mentioned, the coordinative interaction between F8BT and Au cannot be defined by the method of surface energy measurement. Instead, a highly negative (attractive) value of $\chi_2^s = -200$ is assumed to model the coordination. The choice of this number is admittedly arbitrary, but its exact value is not influencing the outcome of the simulations on a qualitative level.

Table 5.3: Flory-Huggins parameters (effective degree of polymerization and interaction parameters) for the ternary blend solvent/F8BT/P(VDF-TrFE)

		χ_{ij}		
	N_i	Solvent	F8BT	P(VDF-TrFE)
Solvent*)	1	0	0.4	0.3
F8BT	77	0.4	0	0.8
P(VDF-TrFE)	1180	0.3	0.8	0

Table 5.4: Substrate and air-interaction parameters for the ternary blend solvent/F8BT/P(VDF-TrFE)

	solvent	F8BT	P(VDF-TrFE)
$\chi^s_{i\text{-Au}}$	0.1	-200	0.1
$\chi^s_{i\text{-OH}}$	0.6	0.9	0.5
χ^a	1.1	1.1	1.0

The data in Table 5.4 allows computational reproduction of the experimental dot-pattern in the Au substrate passivation by the microcontact printed OH-SAM by assigning the $\chi^s_{i\text{-Au}}$ and $\chi^s_{i\text{-OH}}$ parameters for each blend component to specified clusters of elements on a periodic 2D grid which functions as the substrate in the 3D simulations. 100- or 25-fold replication of the single-dot unit cell in a square geometry is respectively implemented on a 150×150 or 75×75 grid. At the air interface the surface tension for each pure component is represented isotropically by χ^a.[42]

5.5 References

[1]   J. Smith, R. Hamilton, I. McCulloch, N. Stingelin-Stutzmann, M. Heeney, D.D.C. Bradley, T.D. Anthopoulos, Solution-processed organic transistors based on semiconducting blends, *J. Mater. Chem.* **2010**, *20*, 2562, and references cited therein.

[2]   C.J. Brabec, M. Heeney, I. McCulloch, J. Nelson, Influence of blend microstructure on bulk heterojunction organic photovoltaic performance, *Chem. Soc. Rev.* **2011**, *40*, 1185.

[3]   A.C. Morteani, A.S. Dhoot, J.S. Kim, C. Silva, N.C. Greenham, C. Murphy, E. Moons, S. Ciná , J.H. Burroughes, R.H. Friend, Barrier-free electron–hole capture in polymer blend heterojunction light-emitting diodes, *Adv. Mater.* **2003**, *15*, 1708.

[4]   A.C. Arias, F. Endicott, R.A. Street, Surface-induced self-encapsulation of polymer thin-film transistors, *Adv. Mater.* **2006**, *18*, 2900.

[5]   K. Asadi, D.M. de Leeuw, B. de Boer, P.W.M. Blom, Organic non-volatile memories from ferroelectric phase-separated blends, *Nature Mater.* **2008**, *7*, 547.

[6]   Polymer Blends Handbook, (Ed: L. A. Utracki), Kluwer Academic Publishers, Dordecht **2002**.

[7]   M. Kemerink, K. Asadi, P.W.M. Blom, D.M. de Leeuw, The operational mechanism of ferroelectric-driven organic resistive switches, *Org. Electronics* **2012**, *13*, 147.

[8]   V. Khikhlovskyi, R. Wang, A.J.J.M. van Breemen, G.H. Gelinck, R.A.J. Janssen, M. Kemerink, Nanoscale organic ferroelectric resistive switches, *J. Phys. Chem. C* **2014**, *11*, 3305.

[9]   K. Asadi, H.J. Wondergem, R.S. Moghaddam, C.R. McNeill, N. Stingelin, B. Noheda, P.W.M. Blom, D.M. de Leeuw, Spinodal decomposition of blends of semiconducting and ferroelectric polymers, *Adv. Funct. Mater.* **2011**, *21*, 1887.

[10]   M. Li, N. Stingelin, J.J. Michels, M.-J. Spijkman, K. Asadi, R. Beerends, F. Biscarini, P.W.M. Blom, D.M. de Leeuw, Processing and low voltage switching of organic ferroelectric phase-separated bistable diodes, *Adv. Funct. Mater.* **2012**, *22*, 2750.

[11]   A.J.J.M. van Breemen, J.-L. van der Steen, G. van Heck, R. Wang, V. Khikhlovskyi, M. Kemerink, G.H. Gelinck, Crossbar arrays of nonvolatile, rewritable polymer ferroelectric diode memories on plastic substrates, *Appl. Phys. Expr.* **2014**, *7*, 031602.

[12]   M.A. Khan, U.S. Bhansali, D. Cha, H.N. Alshareef, All-polymer bistable resistive memory device based on nanoscale phase-separated PCBM-ferroelectric blends, *Adv. Funct. Mater.* **2013**, *23*, 2145.

[13]   J.J. Michels, A.J.J.M. van Breemen, K. Usman, G.H. Gelinck, Liquid phase demixing in ferroelectric/semiconducting polymer blends: an experimental and theoretical study, *J. Polymer. Sci. Part B: Polymer. Phys.* **2011**, *49*, 1255.

[14]   S.Y. Heriot, R.A.L. Jones, An interfacial instability in a transient wetting layer leads to lateral phase separation in thin spin-cast polymer-blend films, *Nat. Mater.* **2005**, *4*, 782.

[15]   C.M. Björström, S. Nilsson, A. Bernasik, A. Budkowski, M. Andersson, K.O. Magnusson, E. Moons, Vertical phase separation in spin-coated films of a low bandgap polyfluorene/PCBM blend–effects of specific substrate interaction, *Appl. Surf. Sci.* **2007**, *253*, 3906.

[16]   R. Hamilton, J. Smith, S. Ogier, M. Heeney, J.E. Anthony, I. McCullogh, J. Veres, D.D.C. Bradley, T.D. Anthopoulos, High-performance polymer-small molecule blend organic transistors, *Adv. Mater.* **2009**, *21*, 1166.

[17]   A. Bernasik, J. Wlodarczyk-Miskiewicz, W. Luzny, K. Kowalski, J. Raczkowska, J. Rysz, A. Budkowski, Lamellar structures formed in spin-cast blends of insulating and conducting polymers, *Synth. Met.* **2004**, *144*, 253.

[18]   T. Fukuma, K. Kobayashi, T. Horiuchi, H. Yamada, K. Matsushige, Nanometer-scale characterization of ferroelectric polymer thin films by variable-temperature atomic force microscopy, *Jap. J. Appl. Phys.* **2000**, *39*, 3830.

[19]   D.K. Owens, R.C. Wendt, Estimation of the surface free energy of polymers, *J. Appl. Polym. Sci.* **1969**, *13*, 1741.

[20]   D.Y. Kwok, A.W. Neumann, Contact angle measurement and contact angle interpretation, *Adv. Colloid Interface Sci.* **1999**, *81*, 167.

[21]   F.M. Fowkes, Attractive forces at interfaces, *Ind. Eng. Chem.* **1964**, *56*, 40.

[22]   M. Böltau, S. Walheim, J. Mlynek, G. Krausch, U. Steiner, Surface-induced structure formation of polymer blends on patterned substrates, *Nature* **1998**, *391*, 877.

[23]   K.-H. Yim, Z. Zheng, R.H. Friend, W.T.S. Huck, J.-S. Kim, Surface-directed phase separation of conjugated polymer blends for efficient light-emitting diodes, *Adv. Funct. Mater.* **2008**, *18*, 2897.

[24]   A. Budkowski, A. Bernasik, P. Cyganik, J. Rysz, R. Brenn, Surface-directed phase separation in nanometer polymer films: self-stratification and pattern replication, *e-Polym.* **2013**, *2*, 88.

[25]   G. Fichet, N. Corcoran, P.K.H. Ho, A.C. Arias, J.D. Mackenzie, W.T.S. Huck, R.H. Friend, Self-organized photonic structures in polymer light-emitting diodes, *Adv. Mater.* **2004**, *16*, 1908.

[26]   N. Corcoran, P.K.H. Ho, A.C. Arias, J.D. Mackenzie, R.H. Friend, G. Fichet, W.T.S. Huck, Highly-efficient broadband waveguide outcoupling in light-emitting diodes with self-organized polymer blends, *Appl. Phys. Lett.* **2004**, *85*, 2965.

[27]   L.-M. Chen, Z. Xu, Z. Honga, Y. Yanga, Interface investigation and engineering – achieving high performance polymer photovoltaic devices, *J. Mater. Chem.* **2010**, *20*, 2575.

[28]   X. Wang, W.H. Lee, G. Zhang, X. Wang, B. Kang, H. Lu, L. Qiu, K. Cho, Self-stratified semiconductor/dielectric polymer blends: vertical phase separation for facile fabrication of organic transistors, *J. Mater. Chem. C* **2013**, *1*, 3989.

[29]   C. Liu, Y. Li, M.V. Lee, A. Kumatania, K. Tsukagoshi, Self-assembly of semiconductor/insulator interfaces in one-step spin-coating: a versatile approach for organic field-effect transistors, *Phys. Chem. Chem. Phys.* **2013**, *15*, 7917.

[30]   J.L. Wilbur, A. Kumar, H.A. Biebuyck, E. Kim, G.M. Whitesides, Microcontact printing of self-assembled monolayers: applications in microfabrication, *Nanotechnology* **1996**, *7*, 452.

[31]   A. Perl, D.N. Reinhoudt, J. Huskens, Microcontact printing: limitations and achievements, *Adv. Mater.* **2009**, *21*, 2257.

[32]   C.D. Bain, E.B. Troughton, Y.-T. Tou, J. Evall, G.M. Whitesides, R.G. Nuzzo, Formation of monolayer films by the spontaneous assembly of organic thiols from solution onto gold, *J. Am. Chem. Soc.* **1989**, *111*, 321.

[33]   O. Wodo, B. Ganapathysubramanian, Modeling morphology evolution during solvent-based fabrication of organic solar cells, *Comput. Mater. Sci.* **2012**, *55*, 113.

[34]   T. Furukawa, Ferroelectric properties of vinylidene fluoride copolymers, *Phase Trans.* **1989**, *18*, 143.

[35]   T. van Woudenbergh, J. Wildeman, P.W.M. Blom, J.J.A.M. Bastiaansen, B.M.W. Langeveld-Voss, Electron-enhanced hole injection in blue polyfluorene-based polymer light-emitting diodes, *Adv. Funct. Mater.* **2004**, *14*, 677.

[36]   N. Miyaura, A. Suzuki, Palladium-catalyzed cross-coupling reactions of organoboron compounds, *Chem. Rev.* **1995**, *96*, 2457.

[37]   J.W. Cahn, J.E. Hilliard, Free energy of a nonuniform system. I. Interfacial free energy, *J. Chem. Phys.* **1958**, *28*, 258.

[38]   H.E. Cook, Brownian motion in spinodal decomposition, *Acta Metall.* **1970**, *17*, 297.

[39]   P.G. de Gennes, Scaling concepts in polymer physics, *Cornell University Press*, Ithaca, NY **1979**.

[40]   P.J. Flory, Principles of polymer chemistry, *Cornell University Press, Ithaca*, NY **1953**.

[41]   The simulations involve a single solvent rather than a mixture to allow for reasonable computation times. The effect of an actual binary solvent system is outside the scope of this paper.

[42]   J.J. Michels, E. Moons, Simulation of surface-directed phase separation in a solution-processed polymer/PCBM blend, *Macromolecules* **2013**, *46*, 8693.

[43]   C.-S. Kim, D.M. Saylor, M.K. McDermott, D.V. Patwardhan, J.A. Warren, Modeling solvent evaporation during the manufacture of controlled drug-release coatings and the impact on release kinetics, *J. Biomed. Mater. Res. Part B: Appl. Biomater.* **2009**, 688.

[44]   G.A. Buxton, N. Clarke, Ordering polymer blend morphologies via solvent evaporation, *Eur. Polym. Lett.* **2007**, *78*, 56006.

Chapter 6

Detailed study of the wetting layer and its influence on the performance of the ferroelectric diode

It has become evident from Chapter 5 that the same materials can exhibit a wide range of performances depending on variations in the phase-separated morphology of the blend, induced by, amongst others, different processing conditions. In this chapter, as natural next step, we aim at understanding the structure of the wetting layer, described in Chapters 4 and 5, and its influence on the device performance. A combination of AFM, PFM and selective dissolution was used. We show that the wetting layer makes it impossible to fully pole the ferroelectric in the reverse direction. We propose an optimal and simple fabrication recipe to avoid the formation of the wetting layer and to provide an improved blend structure. Finally, it was found experimentally that the devices without wetting layer demonstrate much better endurance characteristics.

6.1 Introduction

It has become evident from Chapter 5 that the same materials can exhibit a wide range of performances depending on variations in the phase-separated morphology of the blend, induced by, amongst others, different processing conditions.[1] In Chapter 4 and 5 the full 3D structure of the blend was reconstructed: three types of domains and a wetting layer on the substrate were found in the blend. In Chapter 3 it was shown that the ferroelectric polarization is crucial for the modulation of the injection barrier in the device. However, the presence of the wetting layer might influence the switching properties of the blend[2-4] and therefore harm the device performance.

In this chapter, as natural next step, we aim at understanding the structure of the wetting layer and its influence on the device performance. We use a combination of atomic force microscopy (AFM) and piezoresponse force microscopy (PFM) to probe the topography of the wetting layer, study its influence on the ferroelectric properties of the blend and hence the device performance. We proposed an optimal and simple fabrication recipe that provides an improved blend structure which does not suffer from the wetting layer. It was found experimentally that the devices without wetting layer demonstrate much better endurance characteristics.

6.2 Results and discussion

6.2.1 Detailed study of the wetting layer

Detailed study of the wetting layer is essential for understanding its influence on the device performance. Similar to Chapter 4 and 5, the selective dissolution technique was used to reveal the 3D structure and hence the wetting layer of the blend deposited on two different substrates: Au and Mo/MoO$_x$. Figures 6.1a,b show topography images of the blend deposited on Au and Mo/MoO$_x$ substrates respectively, obtained by selective dissolution of the ferroelectric component. Both images show a 'forest' of vertical semiconducting domains. However, a remarkable feature in Figure 6.1a is the wetting layer, in our case apparent as a large number of wide semiconducting islands with a height of around 30 nm which is significantly lower than the average thickness of the blend. The presence of the wetting layer leads to a smaller number of electrically active domains (Type-1, see Chapters 3 and Chepter 4). In contrast, the blend deposited on Mo/MoO$_x$ substrate in Figure 6.1b does not show any wetting layer, which is most likely explained by the modified surface energy of the substrate (see Chapter 5).[1]
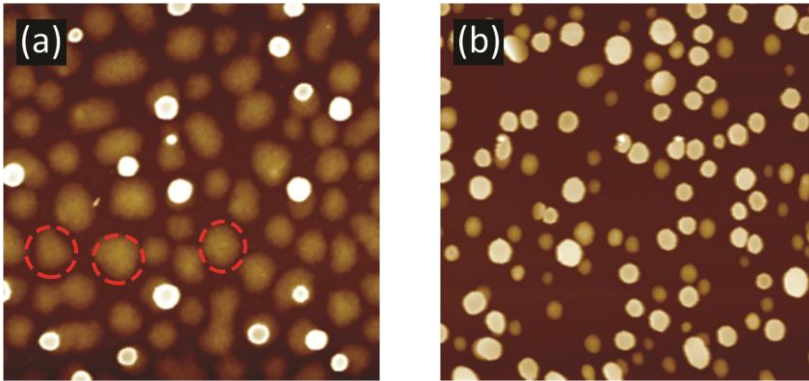
Figure 6.1: AFM topography images (10×10 μm^2) of a P(VDF-TrFE):F8BT (9:1 w/w) blend with selectively dissolved P(VDF-TrFE) phase: (a) Deposited on Au. Three arbitrarily chosen islands corresponding to the wetting layer are shown with red dashed circles. (b) Deposited on Mo/MoO$_x$ substrates. Total vertical scale – 500 nm.

It has already been shown in Chapter 3 that the ferroelectric polarization is crucial for the modulation of the injection barrier in the device. Hence the correlation between the wetting layer and the corresponding ferroelectric properties of the blend at the local scale was investigated. Figure 6.2 presents topography (a, c) and piezoresponse (b, d) of the blend deposited on Au under various polarization conditions. In order to emphasize the effect of the poling, a smaller area of (8×8 μm^2) concentric with the (10×10 μm^2) image was negatively polarized (upward polarization, oriented from the bottom contact to the surface of the blend) and positively (downward) polarized by applying − 20 V and + 20 V to the tip, respectively. Note that poling needs to apply a voltage between the sample and the tip that is above the coercive voltage of the ferroelectric film, *i.e.* in this case ≈ |10| V (see Chapter 2).[5] The AFM tip is then scanned in contact mode over the desired area. In the case of negative poling, the comparison between the topography in panel a and the PFM amplitude in panel b shows that, as expected, the piezoresponse comes only from the ferroelectric matrix phase of the blend, and not from the semiconducting phase. All semiconductor domains appear in the piezoresponse image as dark spots, corresponding to zero piezoresponse. In case of a positive poling voltage, panels c and d, the PFM signal reveals to be significantly inhomogeneous with pronounced 'blind' islands, *i.e.* regions that give zero PFM signal. Comparison between Figure 6.1a and Figure 6.2d suggests that such islands most likely correspond to regions under which a wetting layer is buried: the pattern of the islands in the selective dissolved topography image of the same blend, shown in Figure 6.1a, matches the pattern of the unpoled regions in Figure 6.2d. And interestingly, most of the protruding domains partially or fully coincide with the islands as shown in Figure 6.3. This is in a good agreement with selective dissolved topography image of the same blend shown in Figure 6.1a in which the network of the islands matches the structure of the wetting layer.
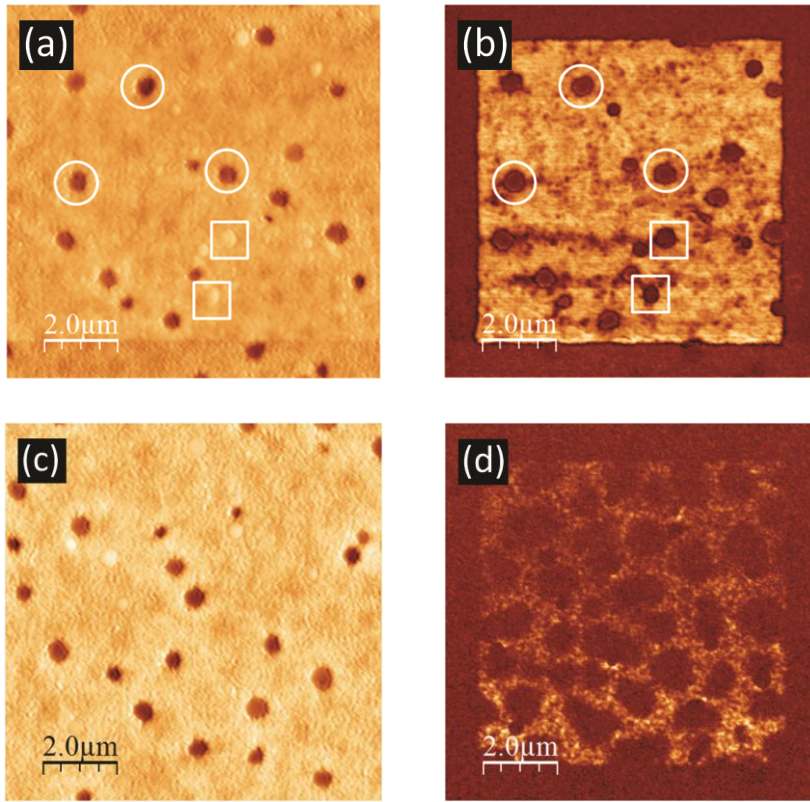
Figure 6.2: PFM–images ($10 \times 10 \ \mu m^2$) of a P(VDF-TrFE):F8BT blend deposited on Au electrode, with from left to right: (a) The topography, (b) The piezoforce amplitude in the case of negative polarization (upwards), and (c), (d) respectively for positive polarization (downwards). Note that the poling was performed on $8 \times 8 \ \mu m^2$ concentric areas to emphasize its effect. Selected full and floating domains are marked with white circles and squares respectively.

The network of the blind islands in Figure 6.2d originates from the fact that the ferroelectric material requires a sufficient number of compensation charges in the contacts in order to pole and stabilize its polarization state.[2-4] Figure 6.4 gives a detailed explanation of the observed phenomenon by showing a schematic representation of the voltage distribution with and without the wetting layer. The ferroelectric and semiconductor layers act as two capacitors in series. In case the semiconductor provides a sufficient number of compensation charges it effectively becomes part of the contact. This means that the full applied voltage drops over the ferroelectric layer which therefore can be poled, as shown in Figure 6.4a. Hence the PFM signal in the FE-phase in Figure 6.2b is homogeneous. In contrast, if the semiconductor does not provide enough compensation charges it acts together with the ferroelectric layer as a voltage divider. Hence the voltage drops mostly over the layer with lowest dielectric constant, *i.e.* the semiconductor and the ferroelectric

cannot be poled as described in Figure 6.4b. Hence the absence of the PFM signal on such islands is due to the fact that the semiconductor polymer F8BT is a poor electron transporter.[6] This makes it impossible to pole and stabilize the ferroelectric polarization for positive applied tip voltages at places where semiconductor material is located at the bottom electrode.
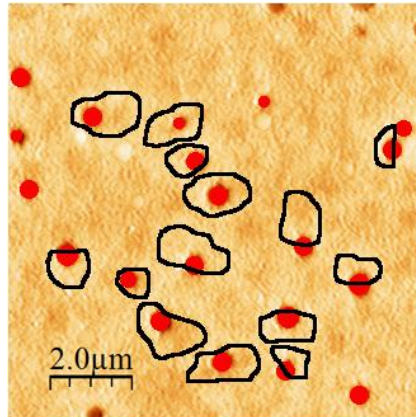
Figure 6.3: AFM topography image (10×10 μm^2) of a P(VDF-TrFE):F8BT blend deposited on a Au electrode (see Figure 6.2c). Red circles correspond to the completed semiconducting domains whereas dark contours represent the boundaries of the islands corresponding to the wetting layer of the blend revealed by PFM (see Figure 6.2d).
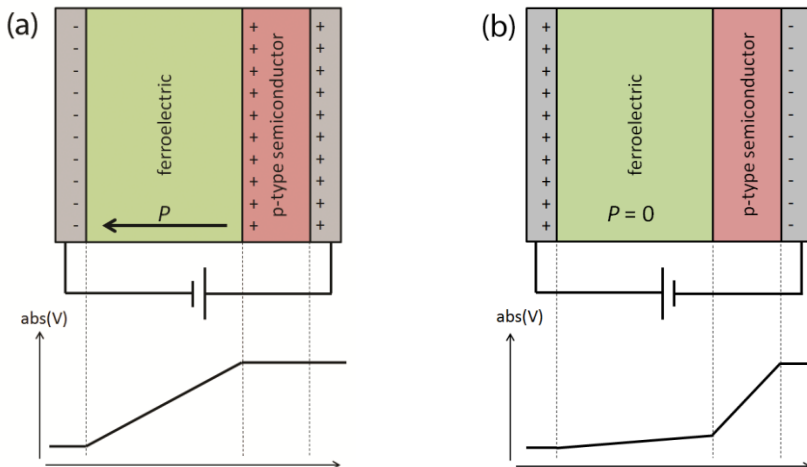
Figure 6.4: Schematic representation of the ferroelectric polarization in a M/FE/SC/M structure. (a) Ferroelectric polarization is preserved and stabilized by holes in the *p*-type semiconductor. (b) Ferroelectric polarization is absent as the *p*-type semiconductor cannot provide electrons. Graphs below the figures sketch the voltage distribution in the corresponding devices.

This finding is further supported by a similar measurement set on blend layers deposited on a Mo/MoO$_x$ substrate, shown in Figure 6.5a–d. As compared to Figure 6.1b, a first observation is that the semiconducting domains have in average a significantly smaller diameter, but their density is larger. Second, the measured piezoresponse of the ferroelectric phase for positive applied voltage (see panel d) is way more homogeneous and comparable to that of the negatively poled situation (see panel b). This is consistent with the morphology of the blend revealed in Figure 6.1b. The most important observation is that the morphology of the blend deposited on Mo/MoO$_x$ substrate demonstrates a similar morphology to the blend deposited on Au substrates covered with an OH-terminated SAM (see Figure 5.2, Chapter 5).[1] However, the fabrication recipe for the Mo/MoO$_x$ – based device is much better in terms of the reproducibility and simplicity since it does not require a preparation of the solution and an overnight deposition (complexity) of the full-coverage (reproducibility) OH-terminated SAM.

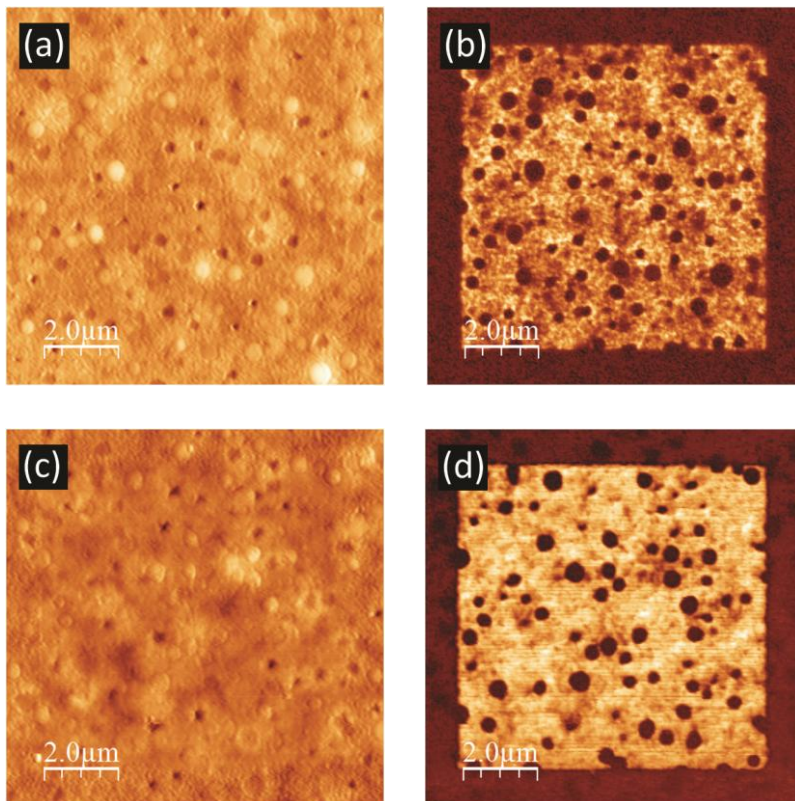**Figure 6.5:** PFM–images (10×10 μm^2) of a P(VDF-TrFE):F8BT blend deposited on a Mo/MoO$_x$ electrode, with from left to right: the topography (a), the piezoresponse amplitude (b), in the case of negative polarization (upwards), and (c), (d) the same for positive polarization (downwards). Again the poling was performed on 8×8 μm^2 concentric areas to emphasize its effect.

A next step was to check the performance of the Mo/MoO$_x$ – based devices and compare them with the Au – based devices. Figure 6.6a,b shows the endurance data of the Mo/MoO$_x$/P(VDF-TrFE):F8BT/Ba/Al and Au/P(VDF-TrFE):F8BT/Ba/Al devices respectively. Both graphs describe the evolution of the *I-V* characteristics upon consecutive program-erase cycles. Despite the fact that Mo/MoO$_x$ – based device has no wetting layer at the bottom electrode, it does not show significantly higher currents in the (positive) forward direction than the Au-based device, similar to the OH-terminated SAM devices (see Figure 5.6, Chapter 5). In fact, this lack of difference is not surprising: at forward bias, the bottom contact is positive, which means that an eventual wetting layer has to provide holes to enable poling the ferroelectric matrix, which is no problem for the *p*-type semiconductor used.

In view of the above, the effect of the absence or presence of the wetting layer on the *I-V* characteristics of the blend would likely be more clearly reflected on devices with symmetric electrodes. However, the effect can also be seen for the current, asymmetric devices. This is visible in Figure 6.6 where the Mo/MoO$_x$/P(VDF-TrFE):F8BT/Ba/Al-device provides an (undesirable) higher current at reverse bias as compared to the Au/P(VDF-TrFE):F8BT/Ba/Al-device because of the presence of the wetting layer, which hampers the charge injection in the device, in the latter case.

Finally, from Figure 6.6, it turned out that the Mo/MoO$_x$ – based device demonstrates much better endurance characteristics than the Au – based one. The reason for this is unclear at present, nor is it evident that this is related to the absence of a wetting layer. Hence using Mo/MoO$_x$ as the bottom electrode provides an easier fabrication recipe, higher reproducibility and improved endurance characteristics.
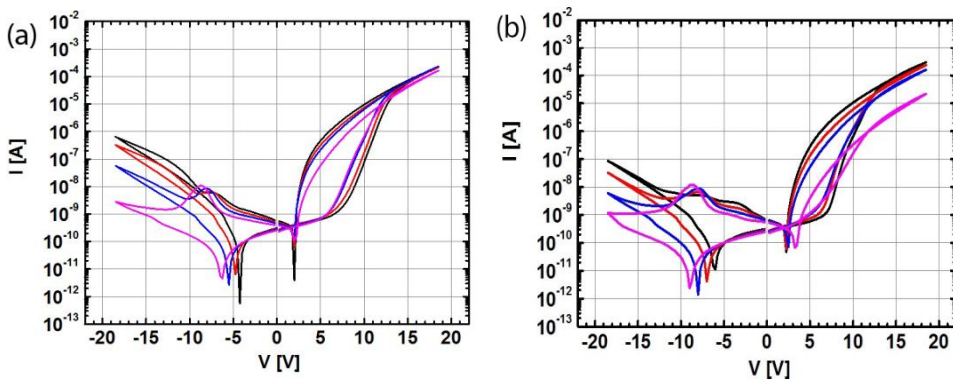

Figure 6.6: Endurance data: Reversible ON- and OFF- switching of the devices: (a) Mo/MoO$_x$/P(VDF-TrFE):F8BT/Ba/Al (b) Au/P(VDF-TrFE):F8BT/Ba/Al. Black, red, blue and purple curves correspond to 1, 10, 100 and 1000 consecutive program-erase cycles respectively.

6.3 Conclusions

In summary, we have studied the structure of the wetting layer and its influence on the device performance. We used a combination of atomic force microscopy (AFM) and piezoresponse force microscopy (PFM) to probe the topography of the wetting layer, study its influence on the polarizibility of the blend and hence the device performance. We showed that the wetting layer makes it impossible to pole large parts of the device in the reverse direction. We proposed an optimal and simple fabrication recipe, making it possible to improve blend structure preventing suffering from the wetting layer. Finally, it was found experimentally that the devices without wetting layer demonstrate much better endurance characteristics.

6.4 Experimental

Poly(vinylidene fluoride-trifluoroethylene) P(VDF-TrFE) (M_n = 220 kDa, 2.3 < D < 2.8 with a 77/23 VDF/TrFe ratio) was supplied by Solvay Specialty Polymers. Poly[(9,9-di-n-octylfluorenyl-2,7-diyl)-alt-(benzo[2,1,3]thiadiazol-4,8-diyl)] F8BT (M_n = 13 kDa, D = 2.0) was synthesized according to a modified Suzuki-polymerization.[7,8]

The active layer in this work is formed by a continuous film of a 1:9 wt/wt blend of F8BT and P(VDF-TrFE). The blend film was spin-coated on top of glass substrates with patterned bare Au and Mo/MoO$_x$ (thin layer of $\approx$ 1 nm of MoO$_x$ was deposited on Mo substrate) electrodes and subsequently annealed at 135 °C for 1 h to enhance the crystallinity of the ferroelectric phase. Using surface profilometry we determined the layer thickness of the P(VDF-TrFE):F8BT blend to be $\approx$ 200 $\pm$ 10 nm.

In order to reconstruct the 3D structure of the self-assembled blend, selective chemical dissolutions of both polymers were performed. Dimethyl sulfoxide (DMSO) was used to dissolve the ferroelectric P(VDF-TrFE) and toluene for the semiconductor (F8BT) parts of the blend.

Atomic force microscopy (AFM) and piezoresponse force microscopy (PFM) were employed to locally probe topography and polarization states respectively. Standard PFM measurements were performed using a high-resolution MFM from the company NanoScan (Switzerland), in contact mode and operated in air, at room temperature. An additional lock-in amplifier (Zürich Instruments, Switzerland) was used to feedback and measure the PFM signal.

6.5 References

[1]   A.J.J.M. van Breemen, T. Zaba, V. Khikhlovskyi, J. Michels, R.A.J. Janssen, M. Kemerink, G.H. Gelinck, Surface directed phase separation of semiconductor ferroelectric polymer blends and their use in non-volatile memories, *Adv. Funct. Mater.* **2015**, *25*, 278.

[2]   I.P. Batra, P. Wurfel, B.D. Silverman, Phase-transition, stability and depolarization ferroelectric thin-films, *Phys. Rev. B* **1973**, *8*, 7, 3257.

[3]   P. Wurfel, I.P. Batra, J.T. Jacobs, Polarization instability in thin ferroelectric films, *Phys. Rev. Lett.* **1973**, *30*, 1218.

[4]   P. Wurfel, I.P. Batra, Depolarization-field-induced instability in thin ferroelectric films – experiment and theory, *Phys. Rev. B* **1973**, *8*, 5126.

[5]   V. Khikhlovskyi, A.V. Gorbunov, A.J.J.M. van Breemen, R.A.J. Janssen, G.H. Gelinck, M. Kemerink, Multi-bit organic ferroelectric memory, *Org. Electron.* **2013**, *14*, 3399.

[6]   Y. Zhang, P.W.M. Blom, Electron and hole transport in poly(fluorene-benzothiadiazole), *Appl. Phys. Lett.* **2011**, *98*, 143504.

[7]   T. van Woudenbergh, J. Wildeman, P.W.M. Blom, J.J.A.M. Bastiaansen, B.M.W. Langeveld-Voss, Electron-enhanced hole injection in blue polyfluorene-based polymer light-emitting diodes. *Adv. Funct. Mater.* **2004**, *14*, 677.

[8]   N. Miyaura, A. Suzuki, Palladium-catalyzed cross-coupling reactions of organoboron compounds, *Chem. Rev.* **1995**, *95*, 2457.

Chapter 7

Data retention in ferroelectric diodes

Solution-processed ferroelectric diodes could become the long-missing non-volatile memory elements in organic electronic devices. To this end, data retention in these devices should be characterized, understood and controlled. First, we show that the measurement protocol can strongly affect the 'apparent' retention time and we identify a suitable protocol. Second, we show by experimental and theoretical methods that partial depolarization of the ferroelectric is the major mechanism responsible for imperfect data retention. This depolarization occurs in close vicinity to the semiconductor-ferroelectric interface, is driven by energy minimization and is inherently present in this type of phase-separated polymer blends. Third, we experimentally and numerically demonstrate a direct relation between data retention and the charge injection barrier height of the diode. Tuning the injection barrier height allows to improve retention by many orders of magnitude in time, albeit at the cost of a reduced on/off ratio.

7.1 Introduction

There is an evident demand for non-volatile memory elements in organic electronics. Unlike in *e.g.* the silicon industry, in organic electronics there does to date not exist a technology that fulfils all demands for a non-volatile memory.[1,2] Solution-processed ferroelectric diodes have recently been proposed as a very promising practical realization of a non-volatile memory that can be read out non-destructively and is compatible with flexible electronics and large area applications.[3,4] The ferroelectric diode consists of a thin film made of a polymeric semiconductor-ferroelectric blend sandwiched between two electrodes. The phase separation in the blend is driven by a spinodal decomposition process which results in sub-micron sized semiconductor domains embedded in a ferroelectric matrix. Thus, transport of charge carriers, which is needed for the resistive read out, is possible only via the semiconducting phase. The working principle of the ferroelectric diode relies on a modulation of the barrier for charge injection from the metal electrode into the semiconductor by the polarization charges in the ferroelectric.[5,6] This makes it possible to switch the device between high- and low- resistive states. The non-volatility and bistability of the ferroelectric diode stem from the remnant polarization of the ferroelectric part of the blend.

Data retention is a crucial parameter for memory elements. It is known that the depolarization phenomenon that occurs in the ferroelectric is the major factor that harms the device performance.[7] However, the detailed mechanism of information loss, especially at the local scale, is unknown. Moreover, although there are a number of publications in which data retention of ferroelectric diodes is studied,[8-10] the exact measurement scheme was not always specified. This hampers both comparison between reports and the assessment of the actual relevance for applications.

In this chapter, we address the related questions regarding the importance of a well-chosen measurement protocol, the mechanism of the information loss, and ways to mitigate data retention. We show that the data retention is intimately linked to the morphology of the phase-separated polymer blend and is due to polarization loss in a narrow region around the semiconducting domains. From theoretical considerations we show that the polarization in this region is inherently instable. As such, the mechanism governing retention in our devices is fundamentally different from those in ferroelectric-only devices[11,12] and in semiconductor-ferroelectric-metal multilayers.[13,14] Mitigation of this fundamental problem is however possible. We find a direct relation between data retention and the charge injection barrier height of the ferroelectric diode which allows to improve retention by many orders of magnitude in time, albeit at the cost of a reduced on/off ratio.

7.2 Results and discussion

7.2.1 Electrical and memory characteristics of a ferroelectric diode

Figure 7.1a shows the hysteretic current-voltage (*I-V*) curve measured on the device fabricated with a P(VDF-TrFE):F8BT 9:1 blend. A Au/MoO$_x$ bottom electrode was chosen for hole injection. The work-function of Au/MoO$_x$ electrode is estimated to be ≈ 5.0 eV[15] because a very thin layer of MoO$_x$ (~ 1 nm) was deposited. Since the energy level of the highest occupied molecular orbital (HOMO) of F8BT amounts to 5.9 eV *vs.* vacuum, the hole injection barrier from Au/MoO$_x$ to HOMO of F8BT is of the order of 1 eV. The contribution from electron transport to the total current, provided by the top Ba/Al electrode, is thought to be negligible because of the low electron mobility in F8BT.[16] However the top Ba/Al electrode is essential for providing asymmetric *I-V* characteristics of the device. Without ferroelectric polarization the large charge injection barrier limits hole injection and, therefore, the current in the device is low. However, the injection barrier can be tuned with the assistance of the stray field of the ferroelectric polarization charges.[5,6] The ascending curve in Figure 7.1a shows that upon increasing the applied voltage the ferroelectric becomes polarized which consequently lowers the injection barrier, leading to a significant current increase which occurs at around the coercive voltage of + 10 V.[17] As the ferroelectric preserves its polarization state when the applied voltage is turned off, the descending part of the *I-V* curve does not follow the ascending one. Thus the positive part of the *I-V* sweep demonstrates significant hysteresis behavior and the device can be
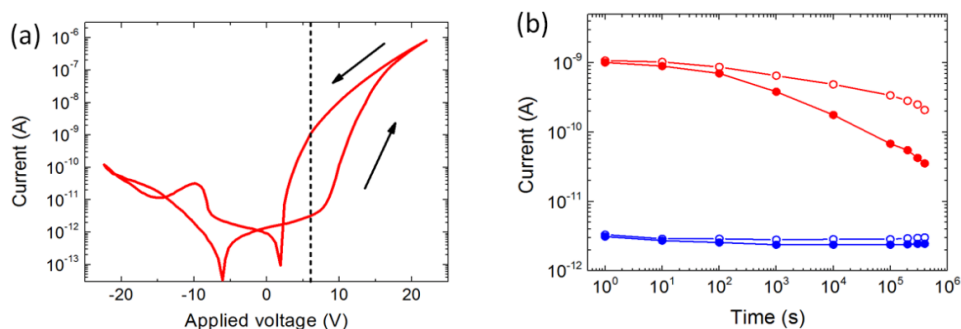
Figure 7.1: Electrical and memory characteristics of a ferroelectric diode fabricated based on a P(VDF-TrFE):F8BT 9:1 blend with Au/MoO$_x$ bottom and Ba/Al top electrodes. (a) Hysteretic current-voltage sweep. Arrows indicate the scan direction, the dashed line at 6 V marks the read-out voltage used in the retention measurements in panel b. (b) Data retention. The device was programmed in the ON- and OFF- states by applying ± 18.5 V respectively. Red and blue circles represent device current in the ON- and the OFF- states respectively. Filled and open circles correspond to short-circuit and constant read voltage protocols, respectively (see text).

programmed to the ON- and OFF- states. The diode is characterized by the I_{ON}/I_{OFF} ratio, the ratio of the ascending and descending curves, measured at a particular read-out voltage (dashed line in Figure 7.1a).

Retention measurements on the same device were done by programming the device to the ON- and OFF- states and subsequently monitoring the corresponding I_{ON} and I_{OFF} currents over time at the read-out voltage shown in Figure 7.1a. It is important to notice that such measurements can be done using at least two different protocols – short-circuit and constant applied voltage respectively. In the former case the read-out voltage is only occasionally applied to the otherwise short circuited device to detect the I_{ON} and I_{OFF} currents. In the latter case the device remains constantly under (read-out) bias. Figure 7.1b shows the data retention of the device in Figure 7.1a. An important finding is that the same device appears to show significantly better memory characteristics when characterized in constant read voltage mode. This is because the polarization state of the ferroelectric is partially prevented from the depolarization by the applied field. In contrast, in the short-circuit mode the device is left undisturbed. This method is representative for actual operational conditions in non-volatile memory devices and should therefore be preferably used. It is used in the rest of Chapter 7.

7.2.2 Underlying mechanism of the information loss

In order to understand the underlying mechanism of the information loss the depolarization in the ferroelectric phase of the device was studied using the double-wave method (DWM). The concept of the DWM is described in detail in Chapter 1. In the DWM a sequence of one 'set' and two (identical) 'probe' pulses is applied and the corresponding switching currents are measured (see Figure 1.7, Chapter 1).[17] The set signal is used to set the desired polarization state of the ferroelectric. The probe pulses are used for studying the prepared ferroelectric polarization. The response to the first probing pulse will contain both the (interesting) switching current and the (undesired) leakage and displacement currents. As the response to the second pulse contains only the latter contributions, these can be subtracted to obtain the switching current. The DWM is more accurate when the switching currents are large compared to the background. This condition is met in reverse bias (see Figure 7.1a) – the device demonstrates a low current at the negative voltage. Thus the DWM is applied by first setting the memory to the ON-state and therefore switches at reverse (negative) bias where the current is low. By knowing the saturated polarization of the ferroelectric the initial polarization state of the device can be retraced. Figure 7.2 shows the ascending part of the ferroelectric polarization hysteresis loop measured right after programming the device and after keeping it for 1 day ($\sim 10^5$ s) at short-circuit conditions. The inset in Figure 7.2 represents the polarization retention of the ferroelectric capacitor of the same thickness and with the same electrodes. The polarization of the ferroelectric hardly changes during the retention measurements, irrespective of the presence of the semiconductor. The measured ferroelectric polarization is similar to that of the ferroelectric

capacitor based on P(VDF-TrFE). In contrast, the I_{ON} current (see Figure 7.1b) decays by at least one order of magnitude during the same time ($\sim 10^5$ s). Taking into account that in the ON-state charge injection occurs in the vicinity of the semiconductor/ferroelectric interface, the most probable explanation is that only a very small fraction of the ferroelectric, around the semiconductor domains, loses polarization during the data retention measurements. An alternative scenario in which *e.g.* the semiconductor degrades can be ruled out by the fact that re-poling will bring back the original high-current ON-state.
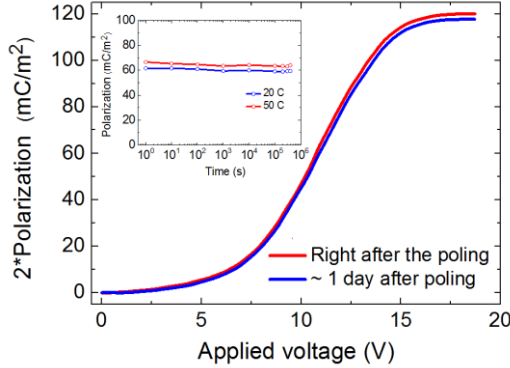

Figure 7.2: Retention of the ferroelectric part of the diode. Red and blue curves correspond respectively to the ascending part of the ferroelectric hysteresis loop of the Au/MoO$_x$/P(VDF-TrFE):F8BT/Ba/Al measured right after programming and after 1 day ($\sim 10^5$ s) of keeping the device at short-circuit conditions. Inset: polarization retention of a ferroelectric capacitor, Au/MoO$_x$/P(VDF-TrFE)/Ba/Al, at two different temperatures.

Figure 7.3 illustrates the proposed depolarization mechanism in the device. We will consider the system's total energy to argue that the polarization of the ferroelectric in close vicinity to the semiconductor is inherently unstable. First, inclusion of a non-ferroelectric (semiconducting) domain in a ferroelectric matrix introduces a domain boundary and a corresponding stray field. The electrostatic energy associated with this stray field increases the total energy of the system, and is inversely proportional to the local dielectric constant. Hence there is a driving force for the polarization edge to move away from the semiconductor ($\varepsilon_r \approx 3$) into the ferroelectric ($\varepsilon_r \approx 10$) (see Figure 7.3) due to the minimum energy principle. The driving force for retracting from the semiconductor domains is counteracted by the energy penalty associated with increasing the perimeter of the depolarized area - the latter mechanism is responsible for the instability of inverted domains below a critical size upon polarization reversal of a ferroelectric.[18-21] Growth of the depolarized area is therefore self-limiting. Once the stray field at its perimeter sits predominantly in the ferroelectric phase, there is no longer a driving force for further depolarization. This rationalizes why the vast majority of polarization charge is time-stable

(see Figure 7.2) whereas the I_{ON} current, that critically relies on the polarization at the semiconductor/ferroelectric interface, decreases by more than an order of magnitude (see Figure 7.1b): recall that the injection current depends critically on the magnitude of the stray field in the semiconductor.[5]
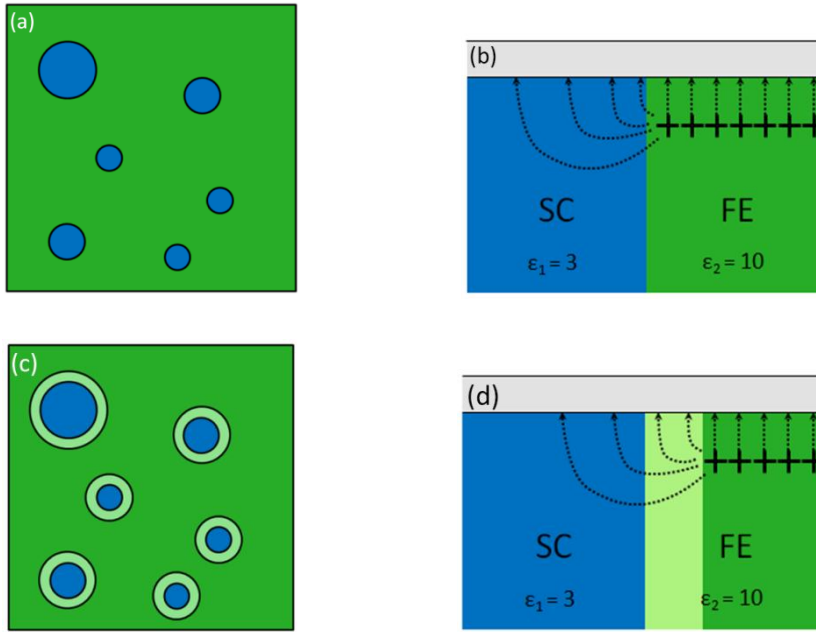
Figure 7.3: Schematic representation of the relation between the morphology and the depolarization phenomenon in the ferroelectric diode. (a) Top view - circular semiconductor domains (blue), are embedded in the ferroelectric matrix (green). (b) Corresponding cross-section, directly after poling. Plus signs indicate polarization charges. Arrows indicate electric fields. (c+d) As (a+b) with partially depolarized ferroelectric phase. Dark (light) green colours corresponds to the polarized (depolarized) ferroelectric regions. The polarization boundary has retracted into the high-dielectric constant region, minimizing total energy. Consequently, current injection, which is driven by the stray field extending into the semiconductor, is reduced.

In order to quantitatively analyze the microscopic depolarization mechanism described above the energy of the ferroelectric diode was calculated. As mentioned above there are two contributions to the total energy of the system: the domain wall (DW) energy and the electrostatic (E) energy. Hence the total energy of the simulated system is calculated as:[18-20]

$$W = W_{dw} + W_e , \tag{7.1}$$

where W_{dw} is the domain wall energy of a domain wall of height h, assumed to be equal to the film thickness, and radius r:

$$W_{dw} \approx (2\pi rh)\,\sigma_{dw} \tag{7.2}$$

which is determined by the domain wall energy $\sigma_{dw} \approx 60$ mJ/m^2 of the ferroelectric.[21]

The electrostatic energy W_e is given by:

$$W_e = \frac{1}{2}\int \varepsilon_0 E(\vec{r})D(\vec{r})d^3r \tag{7.3}$$

where $E(\vec{r})$ is the local electric field and $D(\vec{r})$ is the electric displacement.

Figure 7.4 shows the energy of the system depending on the distance between the polarization domain boundary in the ferroelectric and the semiconductor domain (see Figure 7.3d). It is clear from Figure 7.4 that the total energy of the system crosses a minimum when the width of the depolarized ferroelectric reaches $\approx 20 - 30$ nm, so there is no driving force for further depolarization. The reason that the electrostatic energy term W_e goes down with distance is due to an (im)balance between two components: one related to the field between the polarization charges and their image charges in the metal electrodes, and one component related to the stray field at the polarization edge. The first component gives a positive contribution to the electrostatic energy, so increasing the depolarized area decreases this term. The second component is also a positive term that at larger distances is linear in the perimeter of the depolarized domain, *i.e.* increasing the distance increases this term. Since the first term dominates the electrostatic energy decreases far from the interface. However, the term W_{dw} that is associated with the domain wall energy increases with distance and causes the total energy W to increase once the stray field predominantly sits in the ferroelectric phase. Thus the bulk polarization is time stable – in line with the experimental results above.
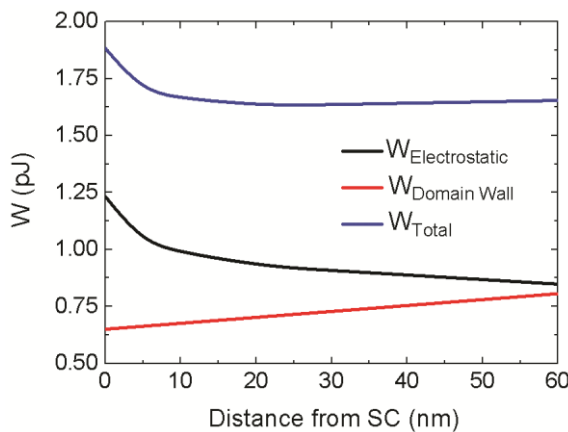

Figure 7.4: Total energy of a system consisting of a cylindrical semiconductor domain of radius 250 nm surrounded by 250 nm of ferroelectric (see Figure 7.3). Electrostatic, domain wall and total energy of the system are shown with black, red and blue curves respectively.

7.2.3 Studying and improving the data retention

Now the mechanism underlying the (partial) depolarization and the associated information loss, as well as its fundamental presence are established, we address the important question on how to mitigate its effects. To this end we compare the measured electrical characteristics of the ferroelectric diodes with large (see Figure 7.4a) and small (see Figure 7.4b) injection barriers. Thus we compare two different polymer semiconductors, F8BT and PTAA, in the same device configuration with Mo/MoO$_x$ and MoO$_x$/Ag serving as bottom and top electrodes respectively. The energies of HOMO and LUMO of F8BT amount to 5.9 and 3.3 eV, respectively,[16] the bottom electrode is most likely to provide hole injection into the F8BT over an injection barrier in the order of 1 eV. At the same time electron transport from the top electrode is suppressed. The I_{ON}/I_{OFF} ratio
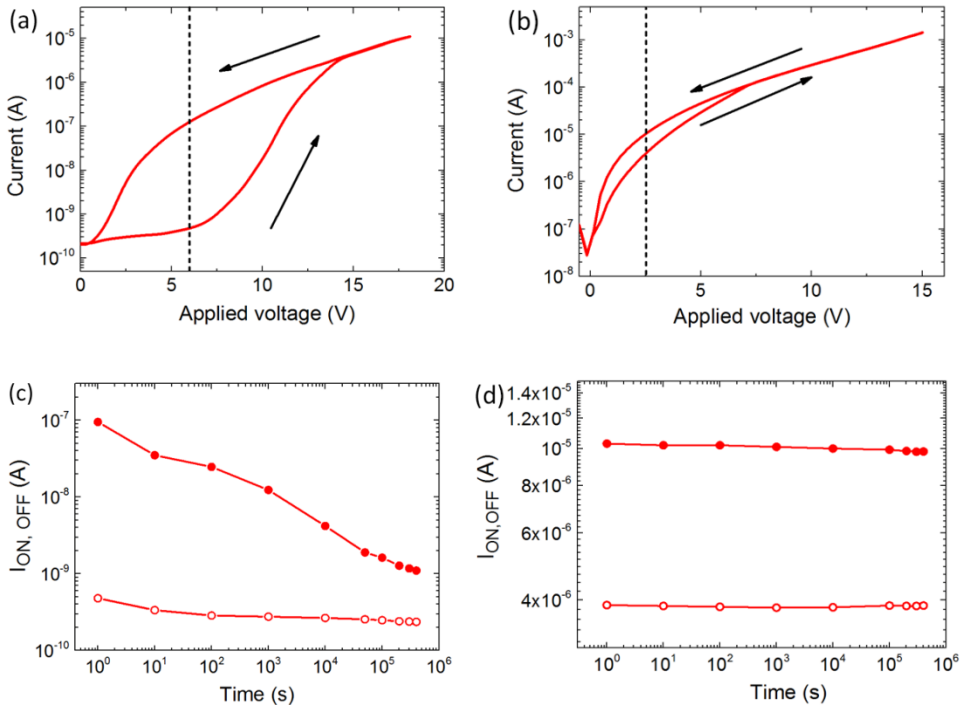
Figure 7.5: Electrical and memory characteristics of ferroelectric diodes. Electrical characteristics of the ferroelectric diode fabricated with: (a) A P(VDF-TrFE):F8BT 9:1 w/w blend with Mo/MoO$_x$ (bottom) and MoO$_x$/Ag (top) electrodes. Arrows indicate the scan direction. (b) As (a) with a P(VDF-TrFE):PTAA 9:1 w/w blend. Arrows indicate the scan direction, dashed lines mark the read-out voltage used in the retention data measurements. (c, d) Data retention of the devices in (a) and (b), respectively after programming at ± 18.5 V (c) and ± 15 V (d). Filled and open circles represent the device current in the ON- and OFF- states respectively.

measured at the read-out voltage yields more than two orders of magnitude. It has to be noted that both I_{ON} and I_{OFF} currents in Figure 7.5a are larger compared to the device in Figure 7.1a. This is most likely related to differences in build-in field due to the different bottom electrodes and to batch-to-batch variations in the semiconductor.

To record the data in Figure 7.5b the same electrodes as in the case of Figure 7.5a were used, but F8BT was replaced with PTAA. Since for PTAA the HOMO and LUMO levels are at 5.25 and 2.3 eV, respectively,[22] the bottom electrode now provides hole injection into the PTAA over a low injection barrier in the order of 0.25 eV. At the same time electron transport from the top electrode remains suppressed. It is not surprising that such a small injection barrier leads to a low I_{ON}/I_{OFF} ratio, in this case of about 2.5. It has to be noted that the difference between I_{ON} and I_{OFF} currents originates truly from the injection barrier modulation and not from spurious effects associated *e.g.* with ionic impurities in the semiconductor. This we ruled out by measuring (hysteresis free) *I-V* characteristics for a bulk PTAA device with the same electrodes and at the same sweep speed (see Figure 7.6).
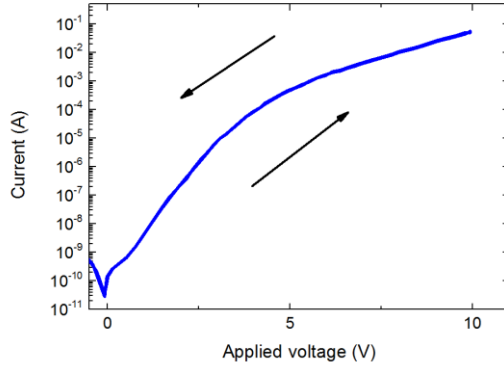
Figure 7.6: Current *vs.* voltage (*I-V*) characteristics of PTAA semiconductor-only diode with Mo/MoO$_x$ (bottom) and MoO$_x$/Ag (top) electrodes. The diode is swept between + 10 and - 10 V. Arrows indicate the scan direction. Sweep speed is comparable to Figure 7.4b.

Figure 7.5c and Figure 7.5d show the data retention of both types of the devices. It is clear that the data retention of diode with large injection barrier, based on the F8BT, shows a similar trend as in Figure 7.1. At the same time the PTAA-based device shows a significant improvement as the ON-state is hardly affected during the course of the measurement. Figure 7.7 shows a joint plot of the normalized I_{ON}/I_{OFF} ratio obtained from Figure 7.5c,d. Intuitively this result can be directly linked to the depolarization phenomenon at the semiconductor/ferroelectric interface as described in Figure 7.3. The diode with low injection barriers relies to a much lesser degree on the ferroelectric polarization charges than the one with large injection barriers. At the same time the absolute I_{ON}/I_{OFF} ratio of the F8BT-based device is always greater than the PTAA-based one.

Figure 7.7: Comparison of the normalized I_{ON}/I_{OFF} ratio as measure for the relative data retention of the ferroelectric diodes in Figure 7.5c,d. Red and blue curves correspond to devices based on the PTAA (low injection barrier) and F8BT (high injection barrier) semiconductors respectively.

In order to substantiate the interpretation of the measurements presented above a 2D model for the charge transport in the ferroelectric diode was e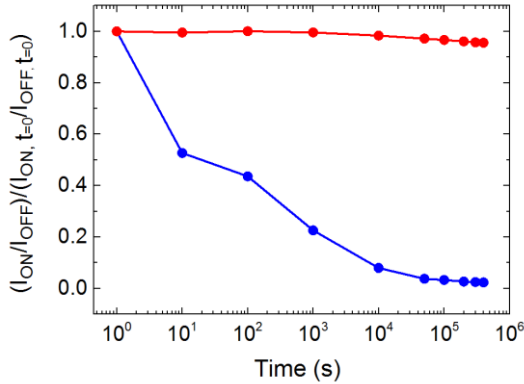mployed.[5] The phase separated morphology is simplified to a 2D structure of alternating ferroelectric and semiconducting slabs. Motion of electrons and holes and the electrostatic potential are described by the transport, continuity, and Poisson equations that are numerically solved on a rectangular grid. The parameters of the blend used in the simulation and the electrical transport model are explained in detail in the Experimental section and Appendix B respectively.

Figure 7.8a shows calculated absolute I_{ON} and I_{OFF} currents versus the ferroelectric polarization of the diodes with injection barriers. As expected the I_{ON}/I_{OFF} ratio of the diode is directly correlated with the injection barrier height. The magnitudes of the ON-currents are in good agreement with the experimentally obtained ones; the OFF-currents are underestimated due to the absence of leakage in the simulations.[5] More importantly, when the polarization charge density is reduced, corresponding to depolarization in the interfacial areas in the actual experiment (see Figure 7.3), the ON-current decreases. This increase is more pronounced and sets in earlier for devices with a high injection barrier, *c.f.* Figure 7.5c,d. Figure 7.8b shows the corresponding normalized I_{ON}/I_{OFF} ratio, its inset shows the absolute I_{ON}/I_{OFF} ratio. Again, reading the polarization charge in the decreasing direction as a measure of time in the experiment, the similarity to Figure 7.6 is striking. Note in particular that due to the self-limiting nature of the depolarization process, see the discussion at Figure 7.3, the polarization charge will not vanish completely for long times. Hence from the numerical model a finite retention at long times is expected. Like in the experiment, the I_{ON} current of the device with largest injection barrier is most sensitive to polarization loss but has the largest I_{ON}/I_{OFF} ratio. This means that the cost of longer

retention time is a lower I_{ON}/I_{OFF} ratio. This result is in a good agreement with Ref. 3 where good data retention was shown at the low read-out voltage *i.e.* low I_{ON}/I_{OFF} ratio. Unfortunately a low I_{ON}/I_{OFF} ratio limits the possibility of large scale integration of the diodes in simple crossbar arrays;[23,24] when combined with more advanced readout electronics the low-injection barrier devices could, however, form the basis for a stable organic memory.
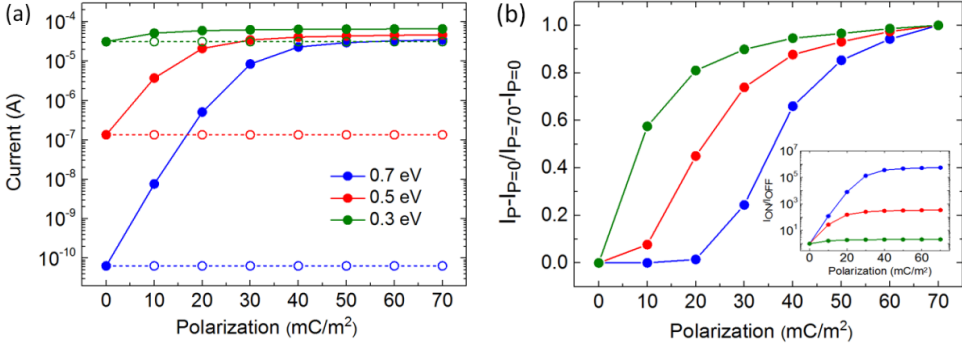
Figure 7.8: (a) Simulated absolute I_{ON} and I_{OFF} – currents *vs.* ferroelectric polarization of the resistive diode with different injection barriers (indicated in the figure) into the semiconductor. Solid and dashed lines represent I_{ON} and I_{OFF} currents respectively. (b) Corresponding normalized I_{ON}/I_{OFF} ratio and absolute I_{ON}/I_{OFF} ratio (see inset).

7.3 Conclusions

In summary, we have studied data retention in ferroelectric diodes based on phase separated blends of ferroelectric and semiconducting polymers. We show that the data retention is highly dependent on the measurement protocol. Devices measured while being continuously biased at the read-out voltage demonstrate misleading, but significantly better retention due to the fact that the polarization state of the ferroelectric is partially stabilized by the applied voltage. Detailed study of the data retention reveals that partial depolarization of the ferroelectric is the major mechanism responsible for poor data retention. This depolarization occurs mostly in the close vicinity of the semiconductor-ferroelectric interface. We argue, based on theoretical considerations, that the depolarization is driven by an energy minimization process and therefore inherently present in this type of phase-separated polymer blends. We also find a direct relation between the data retention and the charge injection barrier height of the diodes. We show by experiments and numerical simulations that the devices with a low injection barrier offer much better data retention than devices with a large injection barrier, albeit at the cost of a reduced on/off ratio.

7.4 Experimental

Poly[(9,9-di-n-octylfluorenyl-2,7-diyl) – alt – (benzo[2,1,3]thiadiazol-4,8-diyl)] F8BT (M_n = 4.9 kDa, D = 1.8) was synthesized according to a modified Suzuki polymerization.[25,26] Poly(bis(4-phenyl)2,3,4-trimethylphenyl)amine PTAA (M_n = 17.5 kDa) was purchased from Flexink and used as received. The ferroelectric polymer, poly(vinylidene fluoride-trifluoroethylene) P(VDF-TrFE) (M_n = 220 kDa, 2.3 < D < 2.8 with a 77/23 VDF/TrFe ratio) was supplied by Solvay Specialty Polymers. Blend solution of P(VDF-TrFE):F8BT was prepared by co-dissolving P(VDF-TrFE) and F8BT (9:1 w/w) in a mixture of cyclohexanone and tetrahydrofuran 75:25 (v/v) at 50 °C overnight (50 mg/mL). P(VDF-TrFE):PTAA solution was prepared with the same ratio according to the same recipe with a single solvent cyclohexanone. Cleaned glass substrates with lithographically patterned Au/MoO$_x$ and Mo/MoO$_x$ contact electrodes of 0.44 mm^2 were used. Blend films were then spin coated in a nitrogen-filled glove box. The average film thickness was measured with a DEKTAK profilometer and found to be ≈ 200 ± 10 nm.

Subsequently, the samples were annealed at 135 °C for 1 hour followed by the deposition of the corresponding Ba/Al or MoO$_x$/Au top electrode. Ferroelectric capacitors with Au/MoO$_x$ and Ba/Al electrodes were made according to the same fabrication recipe mentioned above using the same solvent mixture as for P(VDF-TrFE):F8BT.

The 2D drift-diffusion model used for simulating the ferroelectric diodes takes into account the phase separated morphology, which is approximated by alternating slabs of ferroelectric and semiconductor materials such that both materials are always in contact with both electrodes (see Figure 1.5c, Chapter 1). Zero mobility is assumed for the electrically insulating ferroelectric P(VDF-TrFE). In the ferroelectric slab a surface polarization charge density σ_p ≈ 70 mC/m^2 and a static relative dielectric constant ε_r = 10 were used. The organic semiconducting slabs were characterized by a typical (constant) hole mobility, μ_p = 6.5 × 10^{-11} m^2/(V·s), and ε_r = 3. A field-dependent charge injection into the semiconductor over a barrier of finite height is implemented by using the Emtage/O'Dwyer model.[27,28] Further details on the model can be found in Ref. 5, 6 and Appendix B.

7.5 References

[1]   J.S. Meena, S.M. Sze, U. Chang, T.-Y. Tseng, Overview of emerging nonvolatile memory technologies, *Nanoscale Res. Lett.* **2014**, *9*, 526.

[2]   S.-T. Han, Y. Zhou, V.A.L. Roy, Towards the development of flexible non-volatile memories, *Adv. Mater.* **2013**, *25*, 5425.

[3]   K. Asadi, D. M. de Leeuw, B. de Boer, P.W.M. Blom, Organic non-volatile memories from ferroelectric phase-separated blends, *Nat. Mater.* **2008**, *7*, 547.

[4]   A.J.J.M. van Breemen, J.-L. van der Steen, G. van Heck, R. Wang, V. Khikhlovskyi, M. Kemerink, G.H. Gelinck, Crossbar arrays of nonvolatile, rewritable polymer ferroelectric diode memories on plastic substrates, *Appl. Phys. Express* **2014**, *7*, 031602.

[5]   M. Kemerink, K. Asadi, P.W.M. Blom, D.M. de Leeuw, The operational mechanism of ferroelectric-driven organic resistive switches, *Org. Electron*. **2012**, *13*, 147.

[6]   V. Khikhlovskyi, R. Wang A.J.J.M. van Breemen, G.H. Gelinck, R.A.J. Janssen, and M. Kemerink, Nanoscale organic ferroelectric resistive switches, *J. Phys. Chem. C* **2014**, *118*, 3305.

[7]   K. Asadi, J. Wildeman, P.W.M. Blom, D.M. de Leeuw, Retention time and depolarization in organic nonvolatile memories based on ferroelectric semiconductor phase-separated blends, *IEEE T Electron Devices* **2010**, *57*.

[8]   M.A. Khan, U.S. Bhansali, D. Cha, H.N. Alshareef, All-polymer bistable resistive memory device based on nanoscale phase-separated PCBM-ferroelectric blends, *Adv. Funct. Mater.* **2013**, *23*, 2145.

[9]   J. Hu, J. Zhang, Z. Fu, J. Weng, W. Chen, S. Ding, Y. Jiang, G. Zhu, Fabrication of electrically bistable organic semiconducting/ferroelectric blend films by temperature controlled spin coating, *ACS Appl. Mater. Interfaces* **2015**, *7*, 6325.

[10]   S.H. Sung, B.W. Boudouris, Systematic control of the nanostructure of semiconducting-ferroelectric polymer composites in thin film memory devices, *ACS Macro Lett.* **2015**, *4*, 293.

[11]   X. Zhang, H. Xu, Y. Zhang, Temperature dependence of coercive field and fatigue in poly(vinylidene fluoride-trifluoroethylene) copolymer ultra-thin films, *J. Phys. D: Appl. Phys.* **2011**, *44*, 155501.

[12]   G.D. Zhu, Z.G. Zeng, L. Zhang, X.J. Yan, Temperature dependence of polarization fatigue in ferroelectric vinylidene fluoride and trifluoroethylene copolymer films, *J. Appl. Polym. Sci.* **2008**, *107*, 3945.

[13]   R.C.G. Naber, K. Asadi, P.W.M. Blom, D.M. de Leeuw, B. de Boer, Organic nonvolatile memories based on ferroelectricity, *Adv. Mater.* **2010**, *22*, 9, 933.

[14]   R.C.G. Naber, M. Mulder, B. de Boer, P.W.M. Blom, D.M. de Leeuw, Low-voltage polymer field-effect transistors for nonvolatile memories, *Org. Electron.* **2006**, *7*, 132.

[15]   S. Chen, J.R. Manders, S.-W. Tsang, F. So, Metal oxides for interface engineering in polymer solar cells, *J. Mater. Chem.* **2012**, *22*, 24202.

[16]   Y. Zhang, P.W.M. Blom, Electron and hole transport in poly(fluorene-benzothiadiazole), *Appl. Phys. Lett.* **2011**, *98*, 143504.

[17]   V. Khikhlovskyi, A.V. Gorbunov, A.J.J.M. van Breemen, R.A.J. Janssen, G.H. Gelinck, M. Kemerink, Multi-bit organic ferroelectric memory, *Org. Electron.* **2013**, *14*, 3399.

[18]   I. Lukyanchuk, P. Sharma, T. Nakajima, S. Okamura, J.F. Scott, A. Gruverman, High-symmetry polarization domains in low-symmetry ferroelectrics, *Nano Lett.* **2014**, *14*, 6931.

[19]   A.A. Thiele, The energy and general translation force of cylindrical magnetic domains, *Bell System Techn. J.* **1969**, *48*, 3287.

[20]   A.A. Thiele, The theory of cylindrical magnetic domains, *Bell System Techn. J.* **1971**, *50*, 711.

[21]   W.J. Hu, D.-M. Juo, L. You, J. Wang, Y.-C. Chen, Y.-H. Chu, T. Wu, Universal ferroelectric switching dynamics of vinylidene fluoride-trifluoroethylene copolymer films, *Sci. Rep.* **2014**, *4*, 4772, 1.

[22]   A. Intaniwet, C.A. Mills, P.J. Sellin, M. Shkunov, J.L. Keddie, Achieving a stable time response in polymeric radiation sensors under charge injection by X-rays, *Appl. Mater. Inter.* **2010**, *2*, 6, 1692.

[23]   N. Pimparkar, Q. Cao, J.A. Rogers, M.A. Alam, Theory and practice of 'striping' for improved ON/OFF ratio in carbon nanonet thin film transistors, *Nano Res.* **2009**, *2*, 167 175.

[24]   W.A. Goddard III, D. Brenner, S.E. Lyshevski, G.J. Iafrate, Handbook of nanoscience, engineering, and technology, Third Edition, **2012**, 11-25, CRC Press.

[25]   T. van Woudenbergh, J. Wildeman, P.W.M. Blom, J.J.A.M. Bastiaansen, B.M.W. Langeveld-Voss, Electron-enhanced hole injection in blue polyfluorene-based polymer light-emitting diodes, *Adv. Funct. Mater.* **2004**, *14*, 677.

[26]   N. Miyaura, A. Suzuki, Palladium-catalyzed cross-coupling reactions of organoboron compounds, *Chem. Rev.* **1995**, *96*, 2457.

[27]   P.R. Emtage, J.J. O'Dwyer, Richardson−Schottky effect in insulators, *Phys. Rev. Lett.* **1966**, *16*, 356.

[28]   J.J.M. van der Holst, M.A. Uijttewaal, R. Balasubramanian, R. Coehoorn, P.A. Bobbert, G.A. de Wijs, R.A. de Groot, Modeling and analysis of the three-dimensional current density in sandwich-type single-carrier devices of disordered organic semiconductors, *Phys. Rev. B* **2009**, *79*, 085203.

Appendix A

Confirmation of the working mechanism of the ferroelectric diode at the local scale

In Chapter 3, the operating mechanism of the ferroelectric diode at the nanometer scale was studied. A key part of the work relies on the C-AFM experiment where it was shown that the current injection occurs in the vicinity of the semiconductor/ferroelectric interface. Its complexity leads to concerns related to the tip resolution and tip-sample contact radius. In order to confirm the working mechanism of the device at the nanoscale,
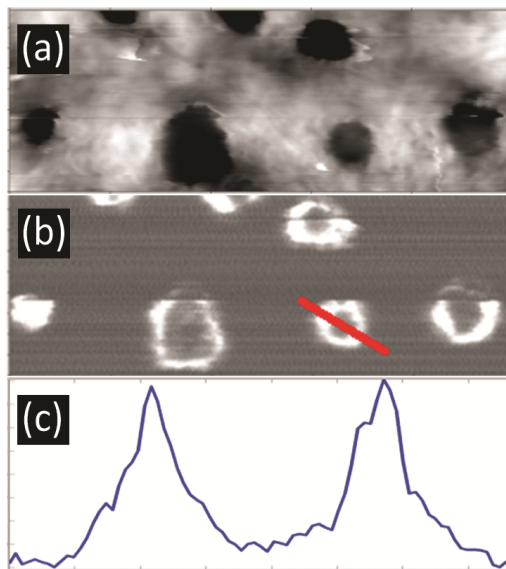
Figure A.1: C-AFM–images (5×2 μm^2) of a P(VDF-TrFE):F8BT (9:1 w/w) blend on Au. (a) Topography (total vertical scale – 70 nm). (b) Corresponding current map. (c) Current cross-section over the conductive domain of diameter 600 nm indicated by the red line in b.

the current from the poled region of the blend was locally recorded by another C-AFM setup at the beam-line end-station NanoXAS at the Swiss synchrotron (SLS), and is shown in Figures A.1. The current distribution image in Figure A.1b shows an unambiguous correlation with the blend topography in Figure A.1a. Another crucial observation in Figure A.1b is the enhancement of the current at the perimeter of the semiconductor domains. This effect can be evaluated quantitatively by considering the cross-section of an arbitrarily selected conducting domain shown by the red line in Figure A.1b. Figure A.1c shows the corresponding current profile. It reveals an approximately fivefold current enhancement at the ferroelectric/semiconductor interface compared to the current measured inside the semiconducting domain. This current profile is an experimental confirmation of the current enhancement in the semiconducting material due to the proximity of the nearby ferroelectric material, as desribed in Chapter 3.

Appendix B

Description of the numerical model

The 2D model for ferroelectric diodes takes into account the phase separated morphology, which is approximated by slabs of ferroelectric and semiconductor material that alternate along the plane of the film in the lateral direction such that both materials are always in contact with the planar bottom electrode. The top electrode is either planar (full device simulation) or pointed (SPM simulation). Motion of electrons and holes is described by the transport, continuity and Poisson equations:

$$j^{n} = qn\,\mu_{n}\nabla\Psi \qquad\qquad\qquad (B1)$$

$$j^{p} = qn\,\mu_{p}\nabla\Psi \qquad\qquad\qquad (B2)$$

$$q\,\frac{\partial n}{\partial t} = \nabla j^{n} + q\,(G - R) \qquad\qquad\qquad (B3)$$

$$q\,\frac{\partial p}{\partial t} = -\nabla j^{p} + q\,(G - R) \qquad\qquad\qquad (B4)$$

$$\nabla\cdot(\varepsilon\,\nabla\phi) = q\,(n - p) \qquad\qquad\qquad (B5)$$

Here ϕ denotes the electrostatic potential, F the electric field, n and p are the free carrier concentrations of electrons and holes, j^{n} and j^{p} are the electron and hole current density, respectively. D_{n}, D_{p}, μ_{n} and μ_{p} are the diffusion coefficients and the mobilities of electrons and holes, respectively. R and G are the recombination and

(photo) generation rate, respectively. The generation rate is set to zero. $\varepsilon = \varepsilon_r \varepsilon_0$ with ε_0 the permittivity of vacuum and ε_r the relative permittivity.

The recombination rate is given by the Langevin expression:

$$R = \gamma np \tag{B6}$$

with

$$\gamma = \frac{\mu_p + \mu_n}{\varepsilon} \tag{B7}$$

Note that the use of the transport equation implies the validity of the Einstein relation:

$$D_{n/p} = \frac{k_B T}{q} \mu_{n/p} \tag{B8}$$

Here, k_B is the Boltzmann constant, T the temperature, and q the elementary charge.

Eqs. B1–B5 are solved on a rectangular 2D grid. Periodic boundary conditions on the left and right hand sides are used, effectively making the simulated device an infinite repetition of alternating slabs of ferroelectric and semiconductor material.

A Boltzmann factor for the hole and electron densities p_0, n_0 at the bottom contact is used as boundary condition for the density in the semiconductor:

$$p_0 = N_0 \exp\left(-\frac{q \varphi_p}{k_B T}\right) \tag{B9}$$

$$n_0 = N_0 \exp\left(-\frac{q \varphi_n}{k_B T}\right) \tag{B10}$$

The $\varphi_{p,n}$ are the effective hole and injection barriers that must add up to the HOMO-LUMO gap, *viz.* $\varphi_p + \varphi_n = E_g$. The boundary condition at the top contact is a similar Boltzmann factor. The injection barriers $\varphi_{p/n}$ may be reduced to an effective injection barrier $\varphi'_{n/p}$ by the image potential, in which case:

$$\varphi'_{n/p} = \varphi_{n/p} - \sqrt{\frac{q|F|}{4\pi\varepsilon_0\varepsilon_r}} \tag{B11}$$

The square root term in Eq. B11 only applies when the electric field *F* is directed to (away from) the contact so electron (hole) injection is facilitated. This model is referred to as the Emtage O'Dwyer model and gives rise to a field dependent charge injection.

In the ferroelectric slab a surface polarization charge density $\pm\sigma_p$ can be fixed on the second and the next to the last grid points, *i.e.* above the bottom electrode and below the top electrode. The first and the last grid points are filled with the spacer material and screening charges respectively. The sign depends on the polarization direction.

A bias *V* may be applied between the contacts by setting the electrostatic potential at the top contact at $-qV$ while keeping the potential of the bottom contact at zero.

Solutions to Eqs. B1–B5 are obtained by setting the appropriate boundary conditions for *n*, *p* and ϕ at the start of the simulation at *t* = 0. For the rest, the device is taken to be depleted of mobile charges at *t* = 0. In subsequent small time steps, currents are calculated from Eqs. B1–B2, which, for each time step, give rise to a change in the carrier density according to Eqs. B3–B4 and to a new electrostatic potential according to Eq. B5. The changed field at the contacts translates into a change in the boundary conditions Eqs. B9,10 via Eq. B11. Steady state is reached when currents and carrier densities no longer change.

Summary

Organic Ferroelectric Diodes

Today's world demands a special type of electronics. Those new devices will look nothing like rigid metal and plastic boxes. Instead, they will be extremely light, soft, flexible, transparent, cheap or a combination thereof, and can be integrated into everyday objects like paper, clothes and packaging material. The ferroelectric diode could be a very attractive information storage element in this type of electronics because it can be processed from solution on rigid and flexible plastic substrates at low temperatures. Other important features of this device are architectural simplicity and the possibility of non-destructive read out, making it an extremely promising candidate for large-area, low-cost, non-volatile reprogrammable memory applications in general.

The aim of the research described in this thesis is the understanding-based development, characterization and optimization of ferroelectric memory devices, *i.e.* capacitors and diodes.

In Chapter 2, a multi-bit organic ferroelectric-based non-volatile memory with binary readout from a simple capacitor structure is introduced. The functioning of the multi-bit concept is quite generally applicable and depends on the following properties for the data storage medium: (a) The data storage medium effectively consists of microscopic switching elements ('hysterons'). (b) The positive and negative coercive fields of each hysteron are equal in magnitude. (c) The distribution of hysteron coercive fields has substantial width. It is shown that the organic ferroelectric copolymer P(VDF-TrFE) meets these requirements. All basic properties of our device are measured and modeled in the framework of the dipole switching theory. As a first example the possibility to independently program and subsequently read out the lower, middle and upper parts of the hysteron distribution function, yielding a 3-bit memory in a single capacitor structure, is shown. All measured devices show good state reproducibility, high endurance and potentially great scalability.

In Chapter 3, various scanning probe techniques are combined with numerical modeling to unravel the operational mechanism of ferroelectric diodes. It is shown that the resistive switching results from modulation of the charge injection barrier at the semiconductor-electrode interfaces. The modulation is driven by the stray field of the

polarization charges in the ferroelectric phase, and consequently is restricted to regions where semiconductor and ferroelectric phases exist in close vicinity. Since each semiconductor domain can individually be switched and read out, a novel, nanoscale memory element is demonstrated. An ultimate information density of $\approx$ 30 Mb/cm^2 is estimated for this bottom-up defined memory device.

In Chapter 4, a simple approach to study the full 3D morphology of phase-separated blends, taking advantage of the possibility to selectively dissolve the different components is introduced. This method is applied in combination with AFM to investigate a blend of a semiconducting and ferroelectric polymer that is typically used as active layer in ferroelectric diodes. It is found that the blend consists of a ferroelectric matrix with three types of embedded semiconductor domains and a thin wetting layer at the bottom electrode. Statistical analysis of the obtained images excludes the presence of a fourth type of domains. Criteria for the applicability of the presented technique are discussed as well.

In Chapter 5, the possibility to direct the semiconducting domains of a phase-separating mixture of P(VDF-TrFE) and F8BT in a thin film into a highly ordered 2D lattice by means of surface directed phase separation is demonstrated. Numerical simulation of the surface-controlled de-mixing process provides insight in the ability of the substrate pattern to direct the phase separation, and hence the regularity of the domain pattern in the final dry blend layer. By optimizing the ratio of the blend components, the number of electrically active semiconductor domains is maximized. Pattern replication on a cm-scale was achieved, and improved functional device performance is demonstrated in the form of a tenfold increase of the ON-current and a sixfold increase in current modulation. This approach therefore provides a simple and scalable means to higher density integration, the ultimate target being a single semiconducting domain per memory cell.

In Chapter 6, the device structure and its impact on the device performance are studied by advanced scanning probe techniques. It is found that a thin wetting layer drastically influences the device performance by hindering the ferroelectric polarization in one of the bias directions. An optimal and simple fabrication recipe to avoid the formation of this wetting layer is found. The new fabrication provides an improved blend structure that offers better device performance.

In Chapter 7, the data retention of the devices is characterized, understood and controlled. First, it is shown that the measurement protocol can strongly affect the 'apparent' retention time and a suitable protocol is identified. Second, it is shown by experimental and theoretical methods that partial depolarization of the ferroelectric is the major mechanism responsible for imperfect data retention. This depolarization occurs in close vicinity to the semiconductor-ferroelectric interface, is driven by energy minimization and is inherently present in this type of phase-separated polymer blends. Third, a direct relation between data retention and the charge injection barrier height of the diode is demonstrated experimentally and numerically. Tuning the injection barrier height allows to improve retention by many orders of magnitude in time, albeit at the cost of a reduced

on/off ratio.

To summarize, this thesis describes the local working mechanism, structure and data retention of ferroelectric memory diodes based on phase separated blends of ferroelectric and semiconductor polymers. The operational mechanism of the device is studied at the device level and at the nanoscale by various scanning probe techniques, leading to a fully quantitative device model. In addition a simple approach to study the full 3D morphology of the blend, taking advantage of the possibility to selectively dissolve the different components, is introduced. In combination with the developed methods to control the phase separated morphology, this allows to improve the device performance in a rational manner. The most important result obtained in this work is that the data retention is intimately linked to the morphology of the phase-separated polymer blend and is due to polarization loss in a narrow region around the semiconducting domains. Mitigation of this fundamental problem is possible by tuning the injection barrier height of the device, albeit at the cost of a reduced on/off ratio. An alternative strategy could be to use a semiconductor with a high dielectric constant, which reduces the driving force for depolarization. This might improve the data retention of the devices since it should slow down the depolarization process in the ferroelectric matrix.

Samenvatting

De wereld van vandaag vraagt om een special type elektronica. Deze nieuwe elektronica zal niet bestaan uit hard metaal en plastic behuizingen. Integendeel, het zal extreem licht, zacht, flexibel, transparant, goedkoop of een combinatie van dit alles zijn en zal geïntegreerd kunnen worden in dingen als papier, kleding en verpakkingsmateriaal. De ferroelektrische diode zou een zeer aantrekkelijke informatieopslagelement kunnen zijn in dit type elektronica, omdat het vanuit oplossing geproduceerd kan worden op zowel stugge als flexibele substraten bij lage temperatuur. Andere belangrijke kenmerken van deze component zijn de eenvoudige architectuur en de mogelijkheid om niet-destructief uit te lezen. Dit maakt het een zeer beloftevolle kandidaat voor groot-oppervlakte, goedkope, herprogrammeerbaar permanent geheugentoepassing en in het algemeen.

Het doel van het onderzoek zoals beschreven in dit proefschrift is de op begrip gebaseerde ontwikkeling, karakterisatie en optimalisatie van ferroelektrisch geheugen, zoals condensatoren en diodes.

In Hoofdstuk 2, wordt een multibit organisch permanent geheugen geïntroduceerd gebaseerd op ferroelektriciteit met een binaire uitleesmogelijkheid via een simpele condensatorstructuur. Het functioneren van dit multibitconcept is vrij algemeen toepasbaar en hangt af van de volgende eigenschappen van het opslagmedium: (a) Het opslagmedium bestaat effectief uit microscopische schakelaarelementen ('hysteronen'). (b) De positieve en negatieve coërcieve velden van elk hysteron zijn gelijk in grootte. (c) De verdeling van coërcieve velden van de hysteronen heeft een behoorlijke breedte. Er wordt aangetoond dat het organische ferroelektrische copolymeer P(VDF-TrFE) voldoet aan deze voorwaarden. Alle basiseigenschappen van onze component zijn gemeten en gemodelleerd binnen het raamwerk van de dipoolschakeltheorie. Als een eerste voorbeeld, wordt de mogelijkheid om het lage, midden en hoge gedeelte van de hysteronverdelingsfunctie onafhankelijk te programmeren en daaropvolgend uit te lezen getoond, wat een 3-bits geheugen in een enkele condensatorstructuur oplevert. Alle gemeten componenten laten een goede reproduceerbaarheid van de toestand, een hoog uithoudingsvermogen en een potentieel grote schaalbaarheid zien.

In Hoofdstuk 3, worden verschillende *scanning probe* technieken gecombineerd met numeriek modelleren om het operationele mechanisme van organische ferroelektrische weerstandsschakelaars te ontrafelen. Er wordt getoond dat het weerstandsschakelen het resultaat is van het moduleren van de ladingsinjectiebarrière aan de halfgeleider-elektrodegrensvlakken. De modulatie wordt gedreven door de strooivelden van de polarisatielading in de ferroelektrische fase, en beperkt zich dus tot de regio's waar de halfgeleider en ferroelektrische fasen naast elkaar bestaan. Aangezien elk halfgeleiderdomein individueel geschakeld en uitgelezen kan worden, is dit een demonstratie van een nieuw geheugenelement op de nanoschaal. Er wordt een ultieme informatiedichtheid van $\approx$ 30 Mb/cm^2 geschat voor deze *bottom-up* gedefinieerde geheugencomponent.

In Hoofdstuk 4, wordt een eenvoudige aanpak geïntroduceerd om de volledige 3D morfologie van de fasegescheiden mengsels te bestuderen, gebruik makend van de mogelijkheid om selectief de verschillende componenten op te lossen. Deze methode wordt toegepast in combinatie met AFM om een mengsel van een halfgeleidend en ferroelektrisch polymeer te onderzoeken dat typisch gebruikt wordt als actieve laag in ferroelektrische diodes. Het blijkt dat het mengsel bestaat uit een ferroelektrische matrix met drie types van ingesloten halfgeleidende domeinen en een dunne bevochtigende laag op de bodemelektrode. Statistische analyse van de verkregen beelden sluit de aanwezigheid van een vierde type domein uit. Ook worden criteria voor de toepasbaarheid van de gepresenteerde techniek besproken.

In Hoofdstuk 5, wordt de mogelijkheid om de halfgeleidende domeinen van een fasescheidende mix van P(VDF-TrFE) en F8BT in een dunne film te sturen naar een sterk geordend 2D rooster door middel van oppervlakgerichte fasescheiding gedemonstreerd. Numerieke simulaties van het door het oppervlak gecontroleerde ontmengingsproces geven inzicht in hoeverre het substraatpatroon de fasescheiding en daarmee de regulariteit van het domeinpatroon in uiteindelijke droge laag kan sturen. Door de ratio van de componenten van het mengsel te optimaliseren kan het aantal elektrisch actieve halfgeleiderdomeinen worden gemaximaliseerd. Patroonreplicatie op een centimeterschaal is bereikt, alsmede een verbeterde prestatie van de functionele component in de vorm van een tienvoudige toename van de aan-stroom en een zesvoudige toename in de stroommodulatie. Deze aanpak biedt derhalve een simpele en schaalbare methode om hogere integratiedichtheden te realiseren, met als uiteindelijk doel een enkel halfgeleiderdomein per geheugencel.

In Hoofdstuk 6, wordt de componentstructuur en de invloeden op de prestaties daarvan bestudeerd met geavanceerde *scanning probe* technieken. Het blijkt dat de bevochtigingslaag de prestaties drastisch beïnvloed door het hinderen van de ferroelektrische polarisatie in een van de spanningsrichtingen. Er is een optimaal en eenvoudig fabricagerecept gevonden om de formatie van deze bevochtigingslaag te voorkomen. De nieuwe fabricage biedt een verbeterde structuur van het mengsel wat een betere prestatie oplevert.

In Hoofdstuk 7, wordt de dataretentie van de componenten gekarakteriseerd, verklaard en beheerst. Eerst wordt er getoond dat het meetprotocol een sterk effect kan hebben op de 'schijnbare' retentietijd en wordt er een passend protocol geïdentificeerd. Ten tweede wordt er door middel van experimentele en theoretische methoden aangetoond dat gedeeltelijke depolarisatie van het ferroelektricum het hoofdmechanisme is dat verantwoordelijk is voor de imperfecte dataretentie. Deze depolarisatie treedt op in de buurt van het halfgeleider-ferroelektricum interface, wordt gedreven door minimalisatie van de energie en is intrinsiek aanwezig in dit soort fasegescheiden polymere mengsels. Ten derde wordt een direct verband tussen de dataretentie en de hoogte van de ladingsinjectiebarrière van de diode experimenteel en numeriek aangetoond. Het afstemmen van de injectiebarrièrehoogte kan de retentietijd met ordes van grootte verbeteren, al zij het tegen de prijs van een verminderde aan/uitratio.

Samenvattend, dit proefschrift beschrijft de lokale werking, structuur en dataretentie van ferroelektrische geheugendiodes gebaseerd op fasegescheiden mengsels van ferroelektrische en halfgeleidende polymeren. De werking van de component is bestudeerd op componentniveau en op de nanoschaal door middel van verschillende *scanning probe* technieken, leidend tot een volledig kwantitatief componentmodel. Daarbovenop is er een eenvoudige aanpak om de volledige 3D morfologie van het mengsel te bestuderen geïntroduceerd. In combinatie met de ontwikkelde methodes om de fasegescheiden morfologie te sturen, biedt dit de mogelijkheid om de prestaties op een rationele manier te verbeteren. Het belangrijkste resultaat verkregen uit dit werk is dat de dataretentie sterk verbonden is met de morfologie van het fasegescheiden polymeermengsel omdat polarisatieverlies optreedt in een smalle regio rondom het halfgeleidende domein. Dit fundamentele probleem is te vermijden door de hoogte van de injectiebarrière af te stemmen, zij het tegen de prijs van een verminderde aan/uitratio. Een alternatieve strategie zou het gebruik van een halfgeleider met een hoge diëlektrische constante zijn, hetgeen de drijvende kracht voor depolarisatie vermindert. Dit zou de dataretentie van de componenten kunnen verbeteren, aangezien dit het depolarisatieproces in de ferroelektrische matrix zou moeten vertragen.

Curriculum Vitae

Vsevolod Khikhlovskyi was born on the 1st of December 1985 in Zhovti Vody, Ukraine. After finishing high school in 2003 at the Lyceum in Zhovty Vody, he studied Applied Physics and Electronics at Kyiv National Taras Shevchenko University in Kyiv, Ukraine. In 2009 he was awarded a scholarship for the Top Master Program in Nanoscience at the University of Groningen, The Netherlands. His master graduation project was focused on the nanoscale electronic transport in metal and oxide based devices. After his graduation in 2011 he continued as a PhD student in the group Molecular Materials and Nanosystems at the Eindhoven University of Technology and in the group Organic and Oxide Transistor/Flexible OLED Displays at the Open Innovation Research and Development Center Holst Center. His research was done in the field of ferroelectric diodes. The main results of his PhD research are described in this thesis.

List of publications

1. V. Khikhlovskyi, A.V. Gorbunov, A.J.J.M. van Breemen, R.A.J. Janssen, G.H. Gelinck, and M. Kemerink, Multi-bit organic ferroelectric memory, *Org. Electron.* **2013**, *14*(12), 3399-3405.

2. V. Khikhlovskyi, R. Wang A.J.J.M. van Breemen, G.H. Gelinck, R.A.J. Janssen, and M. Kemerink, Nanoscale Organic Ferroelectric Resistive Switches, *J. Phys. Chem. C* **2014**, *118*, 3305-3312.

3. A. van Breemen, T. Zaba, V. Khikhlovskyi, J. Michels, R.A.J. Janssen, M. Kemerink, and G.H. Gelinck, Surface Directed Phase Separation of Semiconductor Ferroelectric Polymer Blends and their Use in Non-Volatile Memories, *Adv. Funct. Mater.* **2015**, *25*, 278-286.

4. V. Khikhlovskyi, A.J.J.M. van Breemen, J.J. Michels, R.A.J. Janssen, G.H. Gelinck and M. Kemerink, 3D-morphology reconstruction of nanoscale phase-separation in polymer memory blends, *accepted to J. Polym. Sci. Pol. Phys.*

5. V. Khikhlovskyi, A.J.J.M. van Breemen, R.A.J. Janssen, G.H. Gelinck and M. Kemerink, Data retention in organic ferroelectric resistive switches, *in preparation*.

6. X. Li, A.J.J.M. van Breemen, V. Khikhlovskyi, E.C.P. Smits, M. Kemerink, D.J. Broer, G.H. Gelinck, Programmable polymer light emitting transistors with ferroelectric polarization-enhanced channel current and light emission, *Org. Electron.* **2012**, *13*, 9, 1742-1749.

7. A.J.J.M. van Breemen, J.-L. van der Steen, G. van Heck, R. Wang, V. Khikhlovskyi, M. Kemerink, and G.H. Gelinck, Crossbar arrays of nonvolatile, rewritable polymer ferroelectric diode memories on plastic substrates. *Appl. Phys. Express* **2014**, *7*, 031602.

8. J. Lee, A.J.J.M. van Breemen, V. Khikhlovskyi, M. Kemerink, R.A.J. Janssen, G.H. Gelinck, Pulse-modulated multilevel data storage in an organic ferroelectric resistive memory diode, *submitted to Adv. Electron. Mater.*

Acknowledgements

This thesis would not have been possible without the help and support of many people.

First of all, I would like to express my deepest gratitude to my supervisors at the Eindhoven University of Technology and the Holst Centre Prof. Dr. Martijn Kemerink, Prof. Dr. Gerwin Gelinck and Prof. Dr. René Janssen.

Martijn, you have been my supervisor at the TU/e for four years. I would like to thank you for giving me the opportunity to work on this challenging, but very interesting project. Your style of supervision was a key part of my project. I had freedom to do science and at the same time I was gently guided by you to the right direction! You have built a significant part of my personality. Your love and fantastic dedication to science combined with a positive attitude towards life energize people around you. I am thankful for all the conferences, workshops, scientific discussions and other activities I was involved in during my project. What I would like to mention is that you have been supervising me remotely for about one and half years. It worked out pretty well – you were always there to help me whenever needed! And of course my congratulations on your promotion to a full professor position at Linköping University! I wish you good luck in your scientific career and many exciting publications from your growing group!

Gerwin, you have been supervising me at Holst Centre for four years. I would like to thank you for allowing me to work on my PhD project at Holst Centre. I enjoyed my time at Holst Centre – a place where academia and industry meet each other. I learned a lot from you in terms of science, writing manuscripts, presenting results and time/project management. You always brought new ideas and excellent suggestions. You are a very productive and active person; you manage to be everywhere – in science, R&D and industry. My congratulations on your promotion to a professor position at Eindhoven University of Technology! I wish you all the best in your future career!

René, my first impression of you and the M2N group was formed when I received your kind reply on my PhD application – *"Dear Seva, Thank you for your e-mail and application for a PhD position. In our group we have vacancies for PhD students on topics*

related to organic ferroelectrics… Best regards, René Janssen". My four-year PhD journey started from that email. The support (in all aspects) and openness from you, René, was crucial for my PhD project. Your scientific input, especially at the very last stage, was extremely important for completion of my dissertation. You bring up a relaxing, positive and at the same time very productive atmosphere to the M2N group. My congratulations on your SPINOZA Award! "*The Award is the ultimate recognition of the great science and technology of all (former) members of René Janssen's Group*".

I sincerely acknowledge Dr. Albert van Breemen – my daily supervisor at Holst Centre. Albert, I learned a lot from you. I was always fascinated with your enthusiasm, patience, energy and kindness. I am very thankful for your help with my experiments, manuscripts and for all fruitful discussions we had. Because I called you so many times, I still remember your phone number by heart ☺. Your contribution was absolutely essential for the completion of this dissertation.

I am grateful to Dr. Jasper Michels for modeling phase separation in polymer blends that contributed to the work described in thesis.

I would like to thank Nicolas Pilet, Laetitia Bernard and Peter Warnincke for organizing research activities in Switzerland. I stayed there for a few days however we managed to produce data which was important in confirming and strengthening hypothesis.

I would like to thank all the members of my PhD committee: Prof. Dr. Beatriz Noheda, Prof. Dr. Paul Koenraad, Prof. Dr. Dago de Leeuw, Dr. Stefan Meskers for their time and efforts that make my defense possible.

I also appreciate Dr. Kees Flipse, Dr. Peter Bobbert and Prof. Dr. Reinder Coehoorn for their constructive questions and remarks during our weekly group meetings.

I would like to acknowledge Jolanda Kooijmans and Martina Jiricka for their administrative support during my four years of stay at the TU/e.

Next, I would like to thank our technicians Wijnand Dijkstra and Marco van der Sluis for their continuous technical support and help. Wijnand, your assistance in the SPM-related measurements was crucial for my PhD project. Marco, you were always around to fix/improve our setups. I really appreciate Ton van den Biggelaar, engineer from Philips, for his eager help with the fabrication whenever required.

I would like to thank several master students at the TU/e and Holst Centre: Rui, Mina, Tomasz and Jun. All of you helped me a lot during my PhD project and lots of your results ended up in this thesis.

I would like to acknowledge people from the M2N group at the TU/e: Dr. Martijn Wienk, Dr. Stefan Meskers, Stephan, Cristian, Kevin, Mohamed, Wijnand, Igor, Ameneh, Robin, Mike, Andrey, Alice, Hans, Serkan, Harm (thanks for helping me with my Samenvatting ☺), Koen, Le, Vikas and Andrea.

Finally, I would like to thank members of the TP5 group and other people from Holst Centre: Abhishek, Brian, Jan-Laurens, Joris, Karin, Charlotte, Francisco, Juliane, Santhosh, Ashutosh, Hangxing, Aashini, Madelon and Bas.